Karlsruhe Institute of Technology

Understanding the Selective Oxidation of Propane to Acrylic Acid on M1 Phase Mixed Metal Oxide Catalysts using Computational Modelling

Zur Erlangung des akademischen Grades eines
Doktors der Naturwissenschaften
(Dr. rer. nat.)

von der KIT-Fakultät für Chemie und Biowissenschaften
des Karlsruher Instituts für Technologie (KIT)

genehmigte
Dissertation

von

M.Sc. Karnajit Sen

1. Referent: Prof. Dr. Felix Studt
2. Referent: PD Dr. Philipp N. Plessow

Tag der mündlichen Prüfung: 29 October, 2025

Abstract

In this dissertation, the selective oxidation of propane to acrylic acid on the M1 phase of the mixed metal oxide Mo-V-Te-Nb-O catalyst is investigated computationally employing ab initio quantum chemistry methods. Due to the electronic complexity introduced by multiple transition metals and their variable oxidation states, a multilayer cluster model of the Mo-only M1 catalyst, excluding vanadium, to simplify the system is constructed as a ground truth. The study inherently explored various surface dynamics, such as surface oxidation by oxygen, migration of oxygen and hydrogen atoms between metal-oxo sites and water desorption for thermodynamic stabilization.

To accelerate the estimation of C-H activation barriers on all surface configurations, the universal Linear Scaling Relationship (LSR) has been established. Theoretical analysis revealed that fast hydrogen migration between metal-OH and metal-oxo sites, with a low barrier of 20 kJ/mol, facilitates alcohol group insertion, being crucial for oxygenated compounds formation. Using this insight, the minimum energy pathways and the full catalytic cycle for propane oxidation to propylene have been proposed. Afterwards, the successive oxidation of propylene to acrylic acid via allyl alcohol and acrolein as the intermediates have been established. The minimum energy pathways for the unselective path towards isopropanol formation from propane has also been shown. The density functional theory (DFT) calculation shows that the insertion of an -OH group into the adsorbed propyl radical leads to isopropanol formation, which limits selectivity toward acrylic acid. Conversely, –OH insertion into activated propylene or acrolein is essential for acrylic acid production. This dual role of -OH insertion presents a selectivity trade-off in the direct one-step conversion of propane to acrylic acid on the M1 catalyst.

Finally, systematic substitution of Mo by V in two layers of the active site cluster model are performed and several energetically stable V-containing configurations are further investigated for propane oxidation reaction. The results show that increasing vanadium content lowers the C–H activation barriers, with the most active configuration featuring three diagonally positioned vanadium atoms per layer. Structural and electronic analysis indicates that vanadium enhances reactivity of molybdenum by oxidizing it. While tellurium removal from the top layer (due to hydrolysis) has minimal impact on activity, it inhibits hydrogen migration, thereby increasing selectivity toward propylene.

Zusammenfasung

In dieser Dissertation wird die selektive Oxidation von Propan zu Acrylsäure auf der M1-Phase des Mischmetalloxid-Katalysators Mo-V-Te-Nb-O rechnerisch mithilfe ab initio-Quantenchemie-Methoden untersucht. Aufgrund der elektronischen Komplexität, die durch mehrere Übergangsmetalle und deren variable Oxidationszustände entsteht, wird ein mehrschichtiges Cluster-Modell des ausschließlich Molybdän-haltigen M1-Katalysators (ohne Vanadium) als vereinfachtes Referenzsystem konstruiert. Die Studie untersucht verschiedene Oberflächendynamiken, wie die Oxidation der Oberfläche durch Sauerstoff, die Migration von Sauerstoff- und Wasserstoffatomen zwischen Metall-Oxo-Zentren sowie die Wasserdesorption zur thermodynamischen Stabilisierung.

Zur Beschleunigung der Abschätzung der C–H-Aktivierungsbarrieren auf allen Oberflächenkonfigurationen wurde die universelle Lineare Skalierungsbeziehung (LSR) etabliert. Die theoretische Analyse zeigt, dass eine schnelle Wasserstoffmigration zwischen Metall-OH- und Metall-Oxo-Zentren mit einer niedrigen Barriere von 20 kJ/mol die Einfügung von Alkoholgruppen erleichtert, was entscheidend für die Bildung von oxygenierten Verbindungen ist. Basierend auf diesen Erkenntnissen wurden die minimalen Energiepfade und der vollständige katalytische Zyklus für die Oxidation von Propan zu Propylen vorgeschlagen. Anschließend wurde die sukzessive Oxidation von Propylen zu Acrylsäure über Allylalkohol und Acrolein als Zwischenprodukte etabliert. Auch die minimalen Energiepfade für den unselektiven Weg zur Bildung von Isopropanol aus Propan wurden dargestellt. Die Dichtefunktionaltheorie (DFT) zeigt, dass die Einfügung einer –OH-Gruppe in das adsorbierte Propylradikal zur Bildung von Isopropanol führt, was die Selektivität gegenüber Acrylsäure einschränkt. Im Gegensatz dazu ist die –OH-Einfügung in aktiviertes Propylen oder Acrolein entscheidend für die Produktion von Acrylsäure. Diese doppelte Rolle der –OH-Einfügung stellt einen Selektivitätskonflikt bei der direkten einstufigen Umwandlung von Propan zu Acrylsäure auf dem M1-Katalysator dar.

Abschließend wird eine systematische Substitution von Mo durch V in zwei Schichten des aktiven Cluster-Modells durchgeführt, und mehrere energetisch stabile V-haltige Konfigurationen werden weiter hinsichtlich der Propanoxidationsreaktion untersucht.

Die Ergebnisse zeigen, dass ein erhöhter Vanadiumgehalt die C–H Aktivierungsbarrieren senkt, wobei die aktivste Konfiguration drei diagonal angeordnete Vanadiumatome pro Schicht aufweist. Strukturelle und elektronische Analysen zeigen, dass Vanadium die Reaktivität von Molybdän durch dessen Oxidation erhöht. Während die Entfernung von Tellur aus der obersten Schicht (durch Hydrolyse) nur geringe Auswirkungen auf die Aktivität hat, hemmt sie die Wasserstoffmigration und erhöht somit die Selektivität gegenüber Propylen.

Contents

1. Introduction

1.1 Acrylic acid and its economy

Acrylic acid or Propanoic acid is an organic compound with the formula CH2=CHCOOH. It is an organic molecule and the simplest of unsaturated acids. At room temperature, acrylic acid is a liquid and has a characteristic acid and tart aroma. It is corrosive in liquid and vapor forms. The boiling point and melting point of it are 141.0 °C 13.5 °C, respectively.

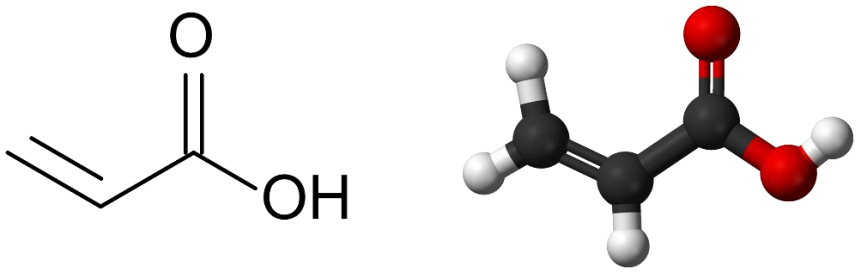

(a) (b)

Figure 1.1 (a) 2D and (b) 3D molecular structure of acrylic acid

Acrylic acid and its esters have long been valued for the formation of economic products for several industries. Its uses include superabsorbent, plastics, coatings, adhesives, elastomers, detergents, water treatment, paints, polishes, paper, leather and textiles (Table 1.1). Additionally, acrylic acid is used in the production of hygienic medical products, detergents, and wastewater treatment chemicals[1]. The major players in the global market are BASF SE, Arkema SA, Nippon Shokubi Co. Ltd. And LG Chem Limited. However, BASF SE held globally the largest capacity of acrylic acid. In March 2023, BASF made an announcement of a new acrylic acid complex in Zhanjiang Verbund site in China. {https://www.chemanalyst.com/industry-report/acrylic-acid-market-287}.

In 2022, the market volume of acrylic acid worldwide amounted to nearly 8.12 million metric tons. It is forecasted that the market volume of this organic compound will grow to around 11.9 million metric tons worldwide in the year 2030 (Figure 1.2).

Industry	Application
Hygiene & Health	Superabsorbents
Housing & Construction	Coatings
Packaging	Adhesives
Mobility & Communication	Detergents
Energy & Resources	Water Treatment
Personale Care	Paper
	Leather & Textile

Table 1.1 Different applications of acrylic acid-based products in several industries

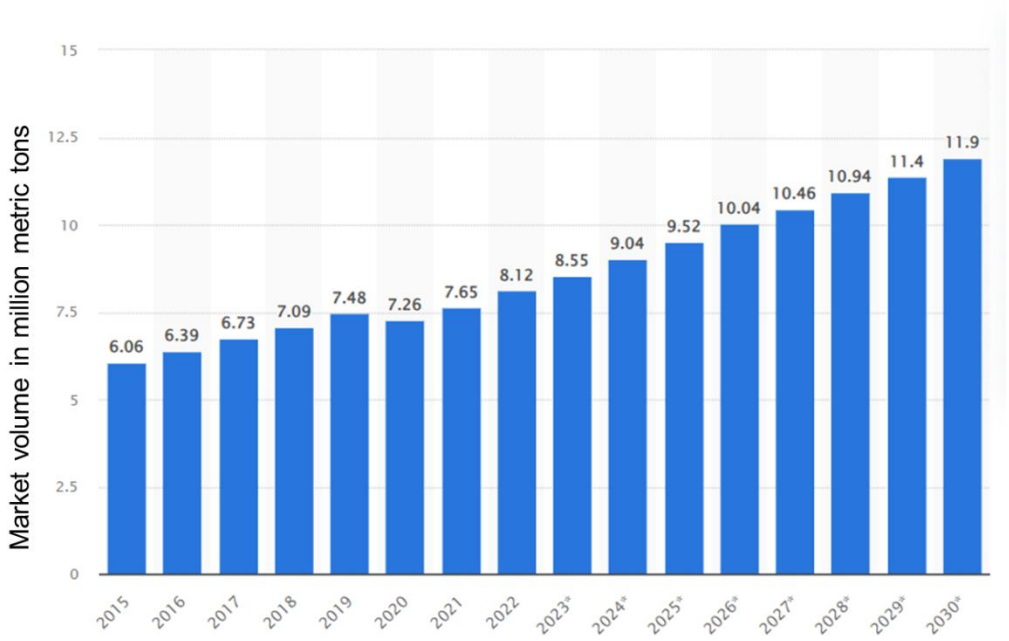

Figure 1.2 Market volume of acrylic acid worldwide from 2015 to 2022, with a forecast for 2023 to 2030. Source ©Statista 2023

1.2 Production Process

Historically acrylic acid has been produced via different routes, among which many have been abandoned for economic and environmental reasons. One of them was the Reppe Chemistry, the hydro carboxylation of acetylene. This method requires nickel carbonyl, high pressures of carbon monoxide, and acetylene, which is relatively expensive compared to propylene. Acrylic acid was also produced from acrylonitrile

which was formed oxidation of propylene via the SOHIO process in 1950's. At present, globally most acclaimed production of acrylic acid is a 2 step process in the gas phase where propylene is first oxidized to acrolein as intermediate, which is further oxidized to acrylic acid via molecular oxygen[1,2]

Step 1: $H_2C{=}CH{-}CH_3 + O_2 \rightarrow H_2C{=}CH{-}CHO + H_2O$, $\Delta H = -340.8$ kJ/mol

Step 2: $H_2C{=}CH{-}CHO + \frac{1}{2}\, O_2 \rightarrow H_2C{=}CH{-}COOH$, $\Delta H = -254.1$ kJ/mol

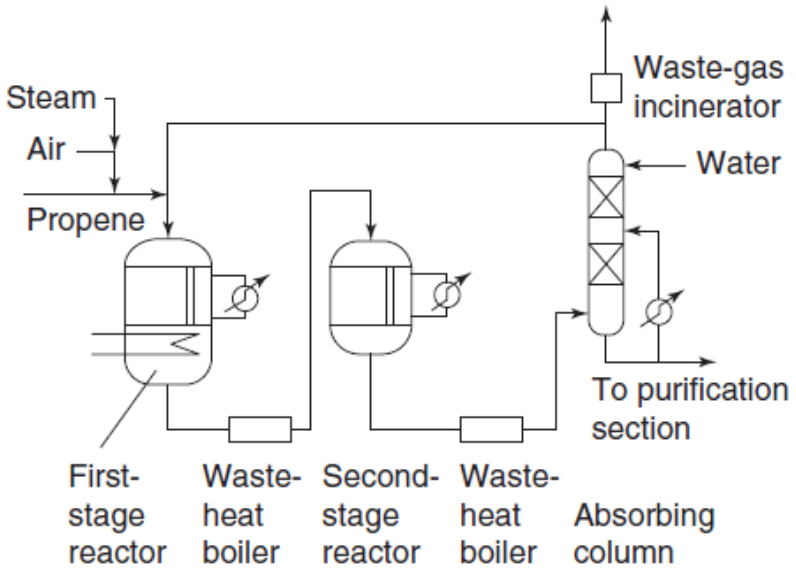

Figure 1.3. Schematic diagram of two stage acrylic acid production. Reproduced from Ref.[3]

The 2-stage process is carried out separately in 2 successive reactors (Figure 1.3) in the presence of different heterogeneous catalysts. First-stage catalysts are acrolein-selective propylene-oxidation catalysts. One of the state of the art industrial catalyst used for this is multicomponent mixed metal oxide Bi-Mo-Co-Fe-K-O based catalysts[4]. The early second stage catalysts for acrolein oxidation were based on another multicomponent mixed metal oxide catalysts Mo-V-W-Cu-O which shows excellent product selectivity with high conversion of propylene[5]. As an alternative, acrylic acid can also be produced from a one-step direct oxidation of propylene as in Equation 1.1.

$$H_2C{=}CH{-}CH_3 + 1\tfrac{1}{2}\, O_2 \rightarrow H_2C{=}CH{-}COOH + H_2O \quad \Delta H = -594.9 \text{ kJ/mol} \qquad (1.1)$$

However, this 1 step process gives a lower yield of acrylic acid than the former two stage process. Optimal reaction temperature for stage 1 of 2 stage process is around

320-330 ºC and for stage 2 it is around 210-255 ºC. Because activation of allyl CH bond of propylene needs more energy than acrolein, the operating temperature of one stage process must be around 325-350ºC to achieve higher conversion. But at this elevated temperature deep oxidation of acrolein and acrylic acid occurs, which leads to unwanted side products and excessive CO/CO_2 production. And this limits desired yield of acrylic acid which make them commercially challenging[2].

1.3 Selective Oxidation of Propane

Partial oxidation of Propane by molecular oxygen can generate different pathways toward several products. All the pathways are highly exothermic processes, producing excessive amounts of heat energy. First CH activation of propane at middle carbon or at the terminal carbon requires higher reaction conditions compared to CH activation energy of the generated products. So, when left uncontrolled, different C3 products can be further oxidized to CO or CO_2 generating more heat. On the other hand, high operating conditions and excessive heat generated can also break the C-C bond producing unwanted C1 or C2 products. Hence, use of efficient catalysis is mandatory to achieve controlled combustion of propane and higher selectivity towards desired product.

Propylene can be formed from propane via two different routes (Figure 1.4). Reaction enthalpy of three different routes in Figure 1.4 is shown in Figure 1.5. Route 1 (blue path in Figure 1.5) is direct two consecutive CH bond cleavages to form propylene intermediate (ΔH= -117 kJ/mol). Route 2 (red path in Figure 1.5) is the formation of isopropanol as an intermediate (ΔH= -174 kJ/mol) and then dehydration of isopropanol to propylene. The first step of route 2 is thermodynamically more favorable than route 1. The mechanism of acrolein production from propylene (ΔH= -300 kJ/mol) can be postulated in 3 steps as follows,

1) abstraction of allylic CH bond of propylene,
2) insertion of oxygen atom in the activated carbon to form allyl alcohol,
3) final dehydrogenation of the same terminal carbon atom to form C=O of acrolein.

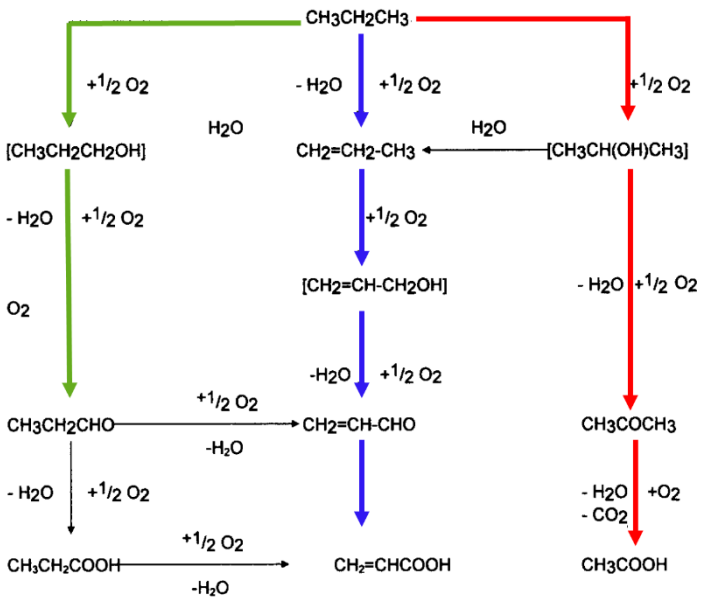

Figure 1.4. Different possible pathways those form olefins, oxygenated molecules, water and CO_2 from the partial oxidation of propane and propylene are shown. Reproduced from ref [6] with permission. The colors of the arrows are partly in corresponds with the color of the thermodynamic paths shown in Figure 1.5. The thermodynamics of the reactions with arrows in black are not shown in Figure 1.5.

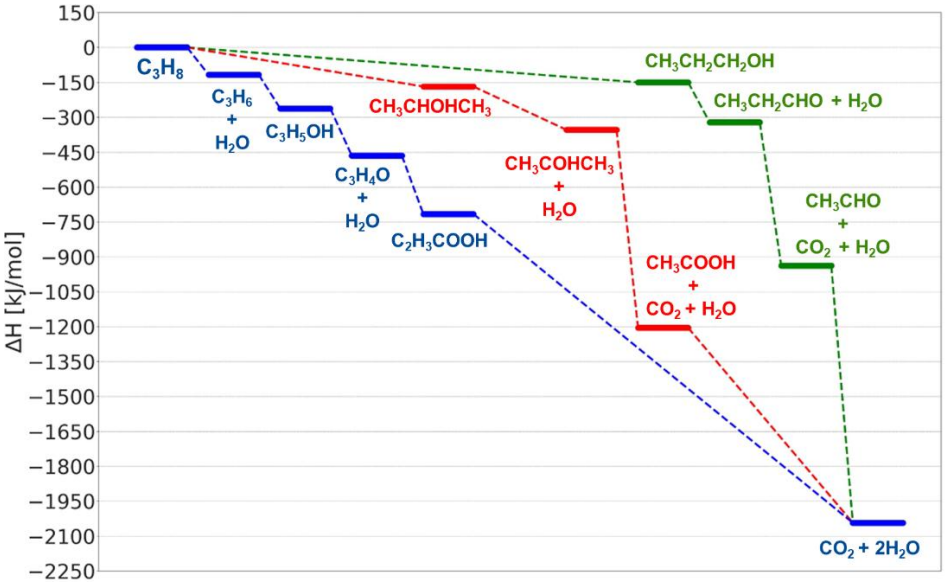

Figure 1.5. Three different thermodynamic pathways for the deep partial oxidation of propane to the valuable products and successive CO_x formation, calculated standard reaction enthalpies[2] are shown in y-axis. The Blue path is for propane oxidation to propylene and the acrylic acid via allyl alcohol and acrolein as the intermediates. The red path shows the formation of iso propanol from propane. Isopropanol further oxidizes to acetone and C-C cleavage of it forms acetic acid and CO/CO_2 in consequence. The green path shows the first formation of propanol from propane. Propanol further oxidizes to propionaldehyde, and C-C cleavage of it forms formaldehyde and CO/CO_2 in consequence.

However, another possibility is also shown via propanol as an intermediate starting from propane (green path in Figure 1.5). Even though this route is thermodynamically more favorable than the former (∆H= -150 kJ/mol compared to -117.1 kJ/mol for the former one), kinetically it needs abstraction of terminal CH bond of propane which is energetically more difficult than CH abstraction from middle carbon of propane.

Propylene is oxidized to allyl alcohol with ∆H= -145 kJ/mol and then to acrolein with ∆H= -203 kJ/mol. Acrolein can be partially oxidized to acrylic acid having ∆H= -251 kJ/mol. Partial oxidation of propane or propylene can lead to unselective pathway towards acetone and acetic acid. Partial oxidation of propane or hydration of propylene can produce iso-propanol which can be further oxidized to acetone. Acetone is further oxidized to acetic acid with high exothermic reaction enthalpy ∆H= -851 kJ/mol and then to CO/CO_2. Once the reaction proceeds towards acetone and acetic acid, it is difficult to bring them back towards selective path of propylene or acrolein towards acrylic acid. Other unwanted side products like formaldehyde, methanol, acetaldehyde are also experimentally observed to be formed in this process. Hence it is especially important to have a controlled selective oxidation of propane using an efficient catalytic system to achieve economically viable selectivity towards acrylic acid.

1.4 Crystal Structure of M1

Bulk mixed metal based oxide material Mo-V-Te/Sb-Nb-O has shown to be one of the most promising catalyst for the conversion of light hydrocarbons to high value products by catalytic selective oxidation reaction in presence of molecular oxygen under favorable reaction conditions[7,8]. In early 1990s, scientist at Mitsubishi Chemicals reported[9] the Mo-V-Te/Sb-Nb-O catalyst for propane ammoxidation to acrylonitrile and acrylic acid. It majorly consists of 2 mixed-metal oxide phases, 1. M1 phases - ($Mo_{7.8}V_{1.2}NbTe_{0.94}O_{28.9,}$ Pba2: a=21.1337Å; b=26.6440Å; c=4.01415Å; z=4,ICSD-55097) and M2 phases ($Mo_{4.67}V_{1.33}Te_{1.82}O_{19.82}$, *Pmm*2: *a*=12.6294 Å; *b*=7.29156 Å; *c*=4.02010 Å; *z*=4, ICSD-55098)[10], but also in minority of other phases such as MoV, MoTe, Mo_5O_{14} etc[11–14]. The M2 phase contains no Nb site, or a few compared to M1 and V^{4+} compared to presence of V^{5+} in M1. These are the key differences between the two phases which also impact their catalytic behavior significantly.

It is believed that the (001) facet of bulk M1 is responsible for the observed catalytic activity[12,15,16]. The 001 plane of Orthorhombic unit cell of M1 phase is composed of hexagonal or heptagonal ring surrounded by MO_6 or MO_7 (M = Mo or V) respectively with Te=O at the center and a pentagonal ring of MO_5 having NbO at the center[17,18]. Figure 1.6 presents a schematic diagram of M1 catalyst. It shows the presence of several different oxidation states of $Mo^{5+/6+}$, $V^{4+/5+}$, $Te^{2+/4+}$ at different sites. The Te at the hexagonal ring has proximity towards the Mo/V which makes it Te^{4+}. Te inside the heptagonal ring resides at the center with oxidation state Te^{2+}. High-resolution TEM studies indicated that the M1 phase domain decreases in the order: Mo-V-Te-Nb-O > Mo-V-Te-O > Mo-V-O[19]. Therefore, Nb and Te are claimed to play a stabilizing role of the crystal structure. The presence of such complex mixed oxidation states of metal and transition metals makes this catalyst inherently interesting and complex by nature.

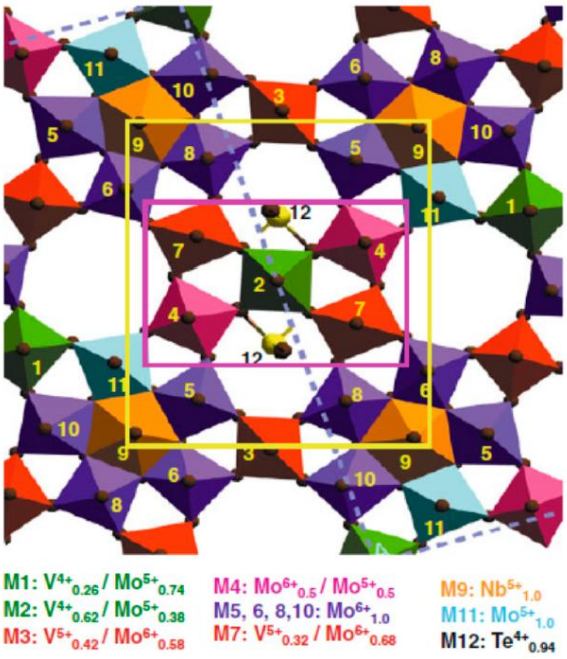

Figure 1.6. Schematic representation of the structure of M1 along the (001) direction. Green represents NbO_7, blue MoO_6 and yellow MO_6; M = Mo or V. Figure reproduced with permission from reference[18]

1.5 Propane ammoxidation to acrylonitrile

Acrylonitrile, C_3H_3N is currently produced by ammoxidation of propylene in presence of ammonia and air using bismuth phosphomolybdate catalysts known as SOHIO

process.[20] More than 10 billion pounds of Acrylonitrile is currently produced and used in the production of acrylic fibers, resins, rubbers etc.

$$CH_2{=}CHCH_3 + NH_3 + 3/2O_2(air) \xrightarrow{catalyst} CH_2{=}CHCN + 3H_2O$$

Direct oxidative dehydrogenation of propane to propylene as an intermediate, followed by ammoxidation of propylene to acrylonitrile is an improved efficient path as one step process. Both M1 phases Mo-V-Nb-Te-O and Mo-V-Nb-Sb-O has shown 62% and 55% acrylonitrile yield at moderate reaction conditions (<450°C, 1-15 atm)[9,10,14,21]. M2 is unable to convert propane due to lack of V^{5+} in M2, whereas Grasseli et al.[21] reported increase of acrylonitrile selectivity in presence of M2 with M1. Woo et al.[22] performed synergetic study between these two phases and suggested M1 is the only phase that is required for the reaction. Shiju et al.[23] reported increasing selectivity of acrylonitrile with presence of Nb and Te in the order Mo-V-Te-Nb-O > Mo-V-Te-O > Mo-V-O, which indicates the better performance of M1 than M2. Yu et al.[24,25] found low activation barrier of 27 kJ/mol for H abstraction of NH_3 by first stabilizing NH_3 at Mo site and then abstraction of H takes place at a neighboring Te-oxo site, using Generalized Gradient Approximation (GGA) level of DFT model. They also found Te-oxo site to be more active than V-oxo site for C-H activation of propane. DeSanto Jr et al.[26] compared 2 different composition Mo-V-Te-Nb-O and Mo-V-Te-Ta-O, replacing Nb by Ta. They showed Ta^{5+} replaces the exact site of Nb^{5+} in the crystal structure and probable to increase the propane conversion rate by increasing number of active sites. Whereas Nb^{5+} increases the presence of acidic Mo^{6+}, which increases the selectivity of acrylonitrile. Aluminum decomposition using atomic layer decomposition (ALD) technique on the surface of M1 has attempted to increase catalytic performance by Shiju et al.[27]. But this shows >95% selectivity to CO_2 with very low conversion of propane compared to exposed M1 surface.

1.6 Oxidative dehydrogenation (ODH) of alkanes

1.6.1 ODH of Ethane

Oxidative dehydrogenation (ODH) of small alkanes to olefins and further oxygenated products is a cyclic redox mechanism, which takes place on catalytic surface via Mars van Krevelen (MvK). First C-H activation is the rate determining step of this mechanism[28]. Hydrogen activation at moderately strong nucleophilic metal-oxo site is responsible for olefin generation, which is followed by oxygen insertion from weak

electrophilic metal-oxo to the olefins creates oxygenated products.[29–31] The basal ab plane (001) have the most surface energy and mainly responsible for highest catalytic performance[27]. The Mo^{6+}/V^{5+} is next to the Te^{4+} inside magenta box of Figure 1.6. acts as the main active site for alkane activation. Nevertheless, several publications show the selectivity largely depends on different synthesis methods of M1. Kolen'ko et al.[32] prepared series of M1 powder by using a hydrothermal-based route, purification of biphasic M1-M2 oxide systems, and an innovative approach utilizing a superheated water vapor treatment of calcined precursors. They studied morphologically different catalysts for the selective oxidation of propane to acrylic acid, revealing that active sites appear on the entire M1 surface and illustrating the high sensitivity of catalyst performance on the catalyst synthesis method. Chu et al.[33] used oxalic acid treatment to modulate the morphology of M1 catalysts and investigated its structure sensitivity during the Oxidative Dehydrogenation of Ethane (ODHE) process. They suggested that the use of a phase pure M1 catalyst with a lower aspect ratio in the ODHE process would be more favorable for ethylene selectivity. Melzer et al.[34] demonstrated differences in catalytic activity among M1 samples of equal chemical composition depend primarily on the morphology of the particles, which determines the predominant terminating facets. Ueda's group[35–37] experimentally and Deshlara's group[38–40] theoretically investigated effect of micropores on catalysis for a deeper understanding of nature of the active site. They suggest that heptagonal channels are responsible for catalyzing ethane, propane and acrolein. However, activity depends on the size of the molecule so it can enter and disperse through the pore dimension. Ethane, being a small molecule, can easily be converted to ethylene inside porous structures. Annamalai et al.[39] studied heptagonal pore of M1 compared to surface V=O sites by using reactant size-dependent kinetic probes and density functional theory (DFT). Their study shows that while ethylene fits to the core, big molecules like benzene cannot access intrapore sites. On the other hand, the tight confinement in micropores hinders the C-O contact necessary for O-insertion, thus intrinsically ensuring high selectivity of ethylene.

1.6.2. ODH of Propane

Several studies were published for ODH of propane on M1. Haevecker et al.[41] studied M1 for propane to acrylic acid by infrared spectroscopy, microcalorimetry, and in situ photoelectron spectroscopy. Their experiments showed that in the presence of steam

as a feed, acrylic acid formation correlates with surface depletion Mo^{6+} and enrichment of V^{5+} sites in close vicinity of Te^{4+}. Raoul Naumann d'Alnoncourt et al.[42] found partial pressure of oxygen as important descriptor for activity of propane, as high oxygen feed keeps the catalyst in high oxidation state and active. They observed that the surface of M1 changes dynamically and reversibly with the change of feed composition. The presence of steam in the feed changes the oxidation states of surface metals and it also correlates with the selectivity towards acrylic acid. Steam caused enrichment of V and Te on the surface at the expense of Mo. They also observed that high O_2 concentration in the feed keeps the catalyst in a high oxidation state. They measured the activation energy of propane in dry feed to be 80-95 kJ/mol, which is reduced to 55-75 kJ/mol in wet feed.

Pierre Kube et al.[43] performed extensive reaction network study for M1 and mesoporous silica supported (6V/SBA-15) catalysts for selective oxidation of propane by temperature-programmed reaction and steady-state using isotope label reactants. The distribution of products observed is similar in both catalysts, only propionic acid is observed for 6V/SBA but not for M1. Other products ensemble contains ethylene, propylene, acetaldehyde, acetic acid, acrylic acid, acrolein, propionaldehyde, acetone, allyl alcohol, CO, and CO_2. Their concentration increases steadily with increasing reaction temperature in range of 100–450 °C. Their Arrhenius plot measures average rate of propane consumption calculated based on sum of reaction products E_a=80 kJ/mol for M1 and 100 kJ/mol for 6V/SBA catalyst. A schematic diagram of complete reaction network was proposed shown in Figure 1.7. Kinetic isotope effects (KIE) study showed that abstracting C-H from methyl group is the rate limiting process on M1. Wernbacher et al.[44] investigated electronic properties of M1 to its catalytic performance for ethane, propane and n-butane oxidation. They saw no change in conductivity for different alkane oxidation in a dry feed, whereas the addition of steam led to decrease of its surface conductivity and work function. Steam significantly influenced surface layer by enriching V^{5+} or Mo^{6+} components and surface hydroxylation. Induced changes in the surface potential barrier by wet propane oxidation feed contributed to a modification of the bulk−surface charge transfer and improved selectivity to acrylic acid.

1.6.3. Role of Te for ODH of Propane

Few studies[14,45,46] presented Te as an indispensable constituent of the active ensemble of M1 catalyst. Whereas Trunschke et al.[47] studied MoV M1 oxide in oxidation of propane in a temperature range where the crystal structure is stable (250−300 °C). Acrylic acid is also formed over the Te-free M1 structure in significant amounts, implying that Te is not necessarily required as a component of the active ensemble responsible for selective oxygen insertion. Compositional complexity of many transitions metal complex and presence of their mixed oxidation state of M1 also makes it inherently very difficult to study computationally. Fjermestad et al.[48] used embedded cluster modelling for $MoVO_x$ system to understand acrolein oxidation to acrylic acid with and without presence of water. Without the presence of water, the energy span of the acrolein conversion to acrylic acid reported as ~170 kJ/mol whereas on a hydrolyzed surface, the energy span reduced to ~145 kJ/mol. O-H assisted C-H bond cleavage is more facile than other mechanisms.

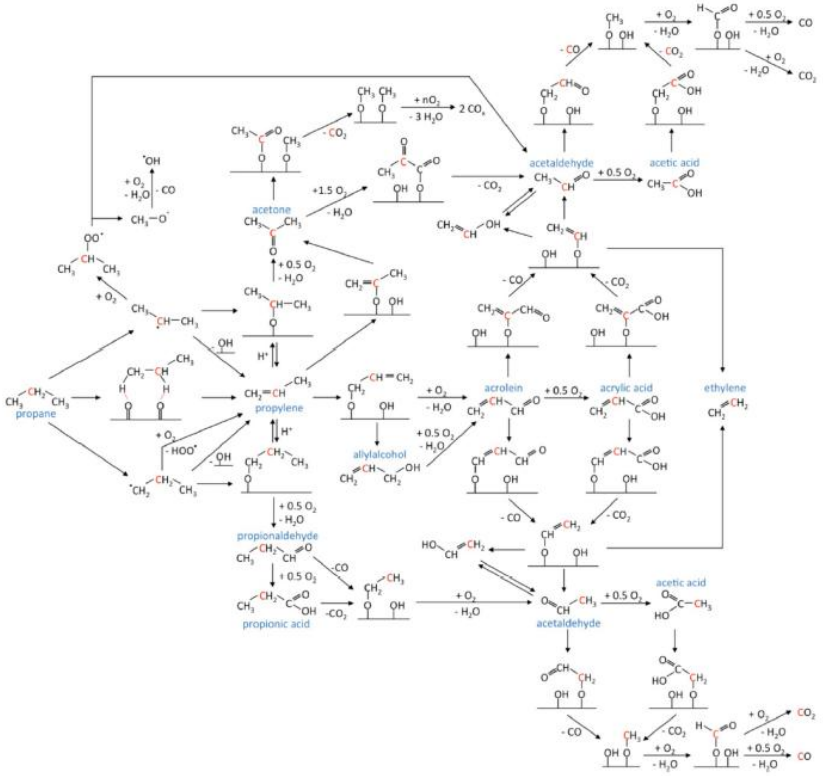

Figure 1.7: Reaction network in propane oxidation outlined based on intermediate products detected in the gas phase (blue) over M1 and 6V/SBA-15 in dry feed ($C_3H_8/O_2/He$=10/5/85) in the temperature range 100-450°C during temperature-programmed propane oxidation; Furthermore, the results of the experiments with d- and ^{13}C-labeled propane (the red color indicates the ^{13}C-labeled carbon atom) have been integrated into the Scheme. This Figure reproduced with permission from reference[43]

1.6.4. Theoretical Studies of ODH of Propane

Nevertheless, the reaction mechanism from propane to acrylic acid is quite complex and thus still not entirely understood[30]. Owing to the importance of the process, the selective propane oxidation over M1/M2 has also been subject to several theoretical studies. It was proposed that C-H abstraction and successive C-O bond formation at allylic positions of different gas phase intermediates as the key steps in the above-mentioned pathways which determined not only activity but also selectivity[49]. Liu et. al used the concept of H-atom addition energy (HAE), steric effects, and the effects of spin multiplicity to understand different active sites on the surface of M1[49,50]. They performed a comparative study for the activation of propane mainly at the porous site of M1 and on the (001) surface of a V_2O_5 catalyst. Due to the large unit cell and the complexity in terms of Mo/V substitution and related oxidation states, simple models of M1 have been invoked. Studies of ODH on M1 by Li et. al.[51] showed correlations between adsorption energies of hydrogen atoms on the surface to the reaction energy and also to the activation barrier of the C-H activation of the alkanes. Based on their findings, they proposed a vertical migration of electrons from the top to the middle layer during the reaction. Cheng et al.[45] studied reduction-coupled oxo activation (ROA) mechanism on single layer cluster of the active site. According to them, first C-H activation of propane occurs by a proton transfer to the Te=O site of 1 (Figure 1.8) and the electron goes to the neighboring V=O site. Then the second proton is transferred from adsorbed propyl radical to another Te=O site to form a propylene molecule. Based on a linear model of activation barrier E_a (Equation 1.2), they proposed that Te should be the most active element having the lowest $D_{O\text{-}H}$ amongst other metal sites. The pathway shown in Figure 1.8 with 5V in surroundings to Te=O sites, potential energy diagram is first uphill by 22.7 kcal/mol to break the secondary C−H bond of propane at Te=O site, while forming intermediate 2 plus isopropyl. Next, the isopropyl radical is trapped by V=O, leading to intermediate 3, which is 16.6 kcal/mol more stable than the reactant. Finally, the second Te=O cleaves the terminal C−H bond of the isopropyl to form species 4 plus propylene. Although the overall reaction is downhill by 10.6 kcal/mol, the reaction energy for the final step is uphill by 6.0 kcal/mol.

$$E_a = D_{C-H} - D_{O-H} \qquad (1.2)$$

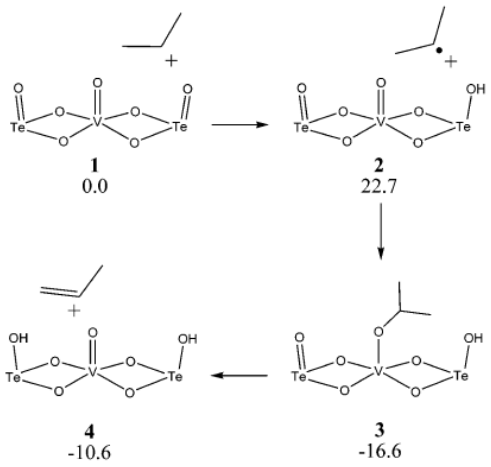

Figure 1.8. Potential energy surface for oxidative dehydrogenation of propane to propene using the 5V configuration 3k (electronic energy only, in kcal/mol). Figure reproduced with permission from reference[45]

1.7 Computational Aspects of CH Activation Chemistry

In the early 1920s, the Sabatier principle emerged[52,53], which mentioned that an optimum catalyst should possess a suitable binding strength towards the reaction intermediate, which indicated that a strong binding would lead to catalysts poisoning, and a too weak binding would fail to activate the reactants. With the development of computational chemistry and, more recently, DFT, the study of heterogeneous catalytic processes and their elementary steps and mechanisms at the atomic scale allowed the discovery of new catalytic materials throughout the use of activity descriptors[54]. Furthermore, as the reaction rates are essentially governed by only a few descriptors, a large number of potential catalysts can be screened rapidly utilizing computational chemistry[55,56]. Nevertheless, the fundamental understanding offered by DFT calculations still serves as a cornerstone in the complete process of computer-aided catalytic design[57].

The alkane C–H bond activation is one of the most active research topics for the industry and the scientific community. It comprises several crucial catalyzed industrial reactions such as dry reforming, steam reforming, selective oxidation, partial oxidation, dehydrogenation, oxidative dehydrogenation. Industrial research is progressed over many years to find and tune for optimum catalyst for CH activation chemistry, because there exist many different paths to improve activity as well as selectivity. For example,

oxidative dehydrogenation of propane, where first CH activation is the rate determining step to produce propylene. Further in the pathway consecutive CH bond activation and selective oxidation of further C3 molecules are crucial chemical steps to generate valuable chemical such as acrylic acid.

CH activation of small alkanes on metal-oxide surface occurs either via radical-like transition state (TS) or the surface stabilized TS structure[58,59]. Figure 1.9 shows the significance difference between these two types which is the carbon (C) to surface metal site distance, indicating different surface interaction influencing the TS barrier. However, in both cases electrophilic H-atom of the methane is transferred to nucleophilic surface oxygen atom (M-O) producing surface M-OH species and either an adsorbed methyl species on a neighboring metal site free or a free methyl radical in the gas phase.

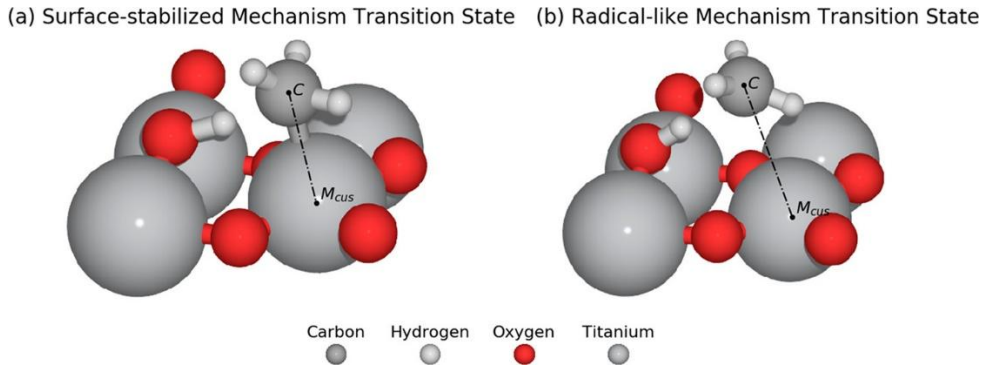

Figure 1.9. Two activation mechanisms on rutile-type metal oxide (110) surfaces are exhibited, (a) the surface-stabilized mechanism TS and (b) the radical-like mechanism TS. Reproduced from Ref.[60] with permission from American Chemical Society, copyright 2019.

1.8 Linear Scaling Relation for Metal Catalyst

Computational screening for vast catalytic materials using large-scale DFT calculations is computationally expensive, making the catalyst discovery solely based on DFT a very challenging task. For each elementary reaction step of complex reaction network, a DFT calculation typically involves optimizing reactants and products on several configurational state-space of the dynamic catalyst surface, location of transition states, and verification of these states as energy minima/maxima along the reaction coordinate of interest. To achieve higher accuracy of such energetics considering

several open shell spin state calculations required higher level of computationally expensive DFT method. As all these calculations are highly computationally demanding, faster approaches to accelerate catalyst screening have always been of the highest necessity.

BrØnsted-Evans-Polanyi (BEP) formalism[61,62] relates activation energies for elementary steps to their reaction energy, causing faster rates for the reactions most favored by thermodynamics. The effective medium theory and d-band center analysis originally proposed by Abild-Pedersen et al.[63] provides a compact explanation for the existence of scaling relationships on transition metal surfaces. In addition a few distinguished studies has proposed Structure-to-Activity Relationship (SAR) for estimation of transition state energies and adsorption energies of different intermediates from simple relevant descriptors such as binding energy of hydrogen (E_H), nitrogen (E_N), oxygen (E_O), carbon (E_C) on metal surfaces[64,65]. Using such descriptors typically results in a description of catalytic performance that follows a volcano-shaped activity behavior facilitating the identification of superior catalytic materials (Figure 1.10b). In particular, candidates near the volcano maximum exhibit high catalytic activity and moderate adsorption strength of reaction intermediates, in line with the Sabatier principle.

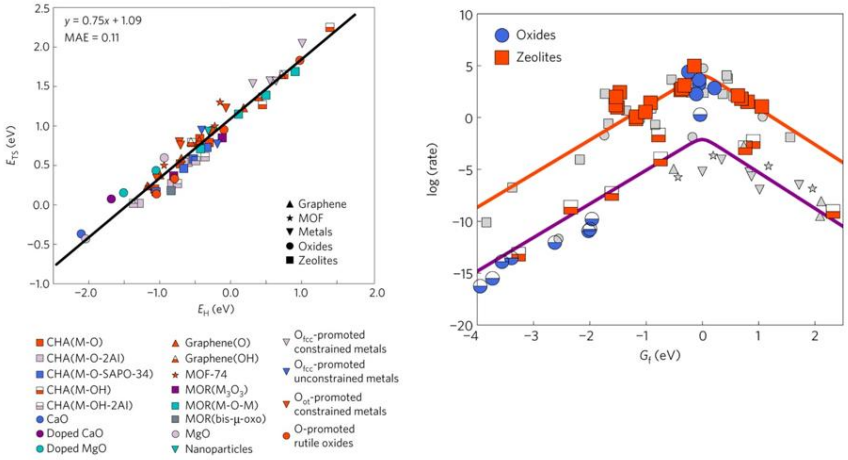

(a) (b)

Figure 1.10. (a) Universal scaling relationship for methane C–H bond activation that proceeds via a radical-like TS. Filled symbols correspond to M_mO_x active sites, while half-filled symbols correspond to M–OH active sites. (b) Identifying promising catalysts for methane activation using scaling relations. Rate volcano for different zeolite topologies for M_mO_x active site motifs (red squares), 4d and 5d transition metal cations for M–O/CHA (half-filled red squares) and oxides (perovskites and strained IrO_2, blue circles). The filled symbols correspond to systems for which a transition state was explicitly calculated using DFT and half-filled symbols

represent the rates predicted by the universal scaling relationship. Adapted from Ref.[59] with permission from Springer Nature, copyright 2017.

Among all these descriptors, E_H (calculated using Equation 1.3) stated to be the most significant descriptor to describe C-H bond activation.

$$E_H = E(M_mO_xH_{y+1}) - E(M_mO_xH_y) - 0.5*E(H_2) \quad (1.3)$$

Where the first term on right is the energy of the surface with adsorbed hydrogen atom, the second term is that without the hydrogen atom and third term is half of the energy of hydrogen molecule.

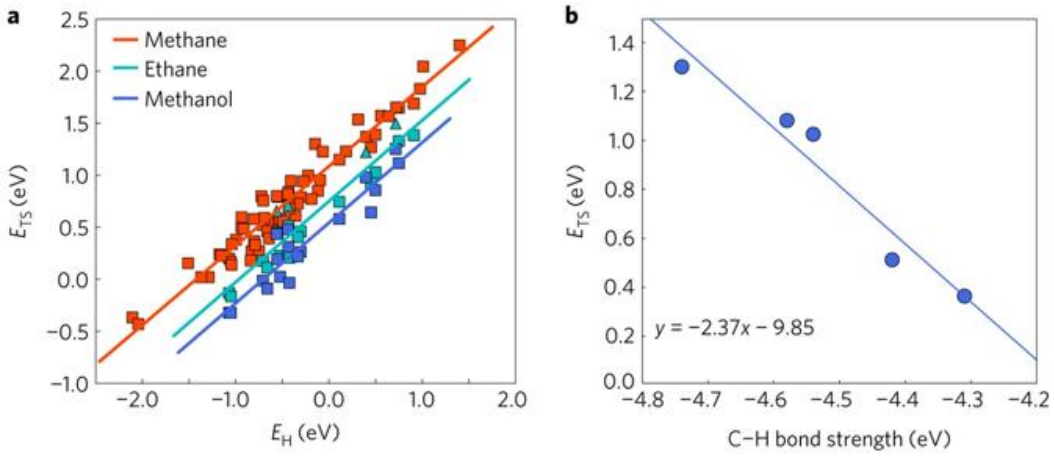

*Figure 1.11. (C–H bond activation for different reactants. a) Universal scaling for C–H activation of methane (E_{TS}=0.75*E_H+1.09, MAE=0.11), ethane (E_{TS}=0.75*E_H+0.7, MAE=0.13) and methanol (E_{TS}=0.75*E_H+0.54, MAE=0.12). b) The activation energies of C1–C3 alkanes and methanol on Fe(Mg)/MOF-74 plotted as a function of C–H bond energies. Adapted from Ref.[59] with permission from Springer Nature, copyright 2017.*

Equation 1.4 presents a more generic scaling relationship for C–H bond activation across reactants and catalysts that depends only on the E_H of the catalyst and the C–H bond energy of the reactant ($E_{C–H}$). This model shows excellent prediction for DFT calculated activation barrier for wide variety of reactants and catalysts (Figure 1.11 a, b)

$$E_{TS} = 0.75E_H - 1.26E_{C–H} - 4.93 \quad (1.4)$$

1.9 Scope of the thesis

In this dissertation, the aim of the thesis is to theoretically understand the activity and selectivity of Mo-V-Te-Nb-O M1 catalyst for acrylic acid formation via selective

oxidation of propane. The complete work is described in the successive chapters as below,

- In Chapter 3, the establishment of the computational models is presented in detail, including rationale of the choice of the DFT methods and Mo-only cluster model creation of M1 catalytic active site.

- The scope of chapter 4 is to establish the full catalytic cycle for propane oxidation to propylene on M1 active site. The chapter focuses on establishing universal linear scaling relationship (LSR) for the M1 cluster model for propane and propyl gas molecule. Different surface phenomena, such as how surface oxidation via gas phase oxygen and surface dynamics to create different surface configurations is discussed. These all together facilitates establishing the full catalytic cycle and minimum energy pathway for propane to propylene formation exploring all possible surface configurations and reaction pathways of the active site.

- In chapter 5, The minimum energy pathways for four selective reactions such as propane to propylene, propylene to allyl alcohol, allyl alcohol to acrolein and acrolein to acrylic acid and one unselective reaction that is propane to isopropanol is presented for all possible surface sites of the Mo-Only M1 active site. The LSR is extended to be more robust for M1 type catalyst for this purpose. The minimum energy pathways is established using two different reaction schemes, one for alkene formation and one for oxygenated product formation.

- Finally in chapter 6, the effect of vanadium content on the active site for the oxidation of propane to propylene is discussed. In addition, the activity of Te-Free M1 active site with and without vanadium is also shown at the end of the chapter.

2. Computational Methods

2.1 ab-initio Quantum Chemistry

Quantum Mechanics is the fundamental theory in Physics that describes nature at microscopic scale where pre-existing Classical Theory of Physics has failed to provide an accurate description of matters and molecules. Electronic structure calculations derived from Quantum Mechanics serve as an important role to define chemical structures, reactivity and laying out a fundamental basis to study physio chemical properties of all organic and inorganic molecules and materials. In this chapter, conventional DFT as the ab-initio Quantum Chemistry method is described briefly. In addition, some relevant theories related to the thesis is discussed.

Catalytic systems can be theoretically described mainly by the motion of nuclei and electrons as well as their interaction in ground states. This system can be described by finding an approximate solution of the non-relativistic time-independent Schrödinger Equation 2.1

$$\mathbf{H}\Psi_{tot}(\mathbf{r}, \mathbf{R}) = E_{tot}\,\Psi_{tot}(\mathbf{r}, \mathbf{R}) \tag{2.1}$$

Where **H** is the multi-electron-non-relativistic Hamiltonian operator. The solution to the equation is $\Psi_i(\mathbf{r}, \mathbf{R})$ which depends on the system of nuclei and electrons described by the position vectors **R** and **r** respectively and the total energy of the system (E_{tot}). In atomic units, the Hamiltonian for N electrons and M nuclei are given by Equation 2.2.

$$\mathbf{H} = -\sum_{i=1}^{N_{elec}} \frac{1}{2}\nabla_i^2 - \frac{1}{2M_A}\sum_{A=1}^{N_{nuc}} \frac{1}{2}\nabla_A^2 - \sum_{A=1}^{N_{nuc}}\sum_{i=1}^{N_{elec}} \frac{Z_A}{r_{iA}} + \sum_{i=1}^{N_{elec}}\sum_{j>i}^{N_{elec}} \frac{1}{r_{ij}} + \sum_{A=1}^{N_{nuc}}\sum_{B>A}^{N_{nuc}} \frac{Z_A Z_B}{R_{AB}} \tag{2.2}$$

In the above equation, M_A is the ratio of the mass of nucleus A to the mass of an electron, and Z_A is the atomic number of nucleus A. The Laplacian operators ∇_i^2 and ∇_A^2 are the differentiation w.r.t the coordinates of the ith electron and the Ath nucleus. The first term is the operator for kinetic energy of the electrons (T_e); the second term represents operator for the kinetic energy of nuclei (T_N); the third term represents the coulomb attraction between electrons and nuclei (V_{Ne}); the fourth and the fifth terms are the repulsion between electrons (V_{ee}) and between nuclei (V_{NN}), respectively. Thus Equation 2.2 can be summarized as below,

$$\mathbf{H} = T_e + T_N + V_{Ne} + V_{ee} + V_{NN} \tag{2.3}$$

The Born-Oppenheimer approximation is central to quantum chemistry[66]. Since nuclei are much heavier than the electrons, they move more slowly. Hence, the changes in the wavefunction are influenced more due to rapid change in the position of electrons in the field than that due to the nuclei. So, the wave function at a given state can be written as a function of nuclear coordinates and electronic wave function as in Equation 2.4.

$$\Psi_{tot}\,\mathbf{(r,\ R)} = \sum_i \chi_{n_i}(R)\ \Psi_i(r, \{R\}) \tag{2.4}$$

Where the curly bracket indicates that Ψ_{elec} parametrically depends on the position of nuclei R. Hence Equation 2.1 can be approximated as Equation 2.5 and 2.6 below,

$$(T_e + V_{Ne} + V_{ee})\Psi_i(r, \{R\}) = E_i\Psi_i(r, \{R\}) \tag{2.5}$$

$$(V_{NN} + E_i(R))\chi_{n_i}(R) = E_{tot}\chi_{n_i}(R) \tag{2.6}$$

So, the total energy of the system E_{tot} can be described by the sum of electronic energy E_{elec} and the constant nuclear repulsion coulomb energy term V_{NN}. The term $V_{Ne}$for coulombic interaction between nuclei and electrons can also be generalized to as an external potential term as V_{ext} (Equation 2.7)

$$\mathbf{H_{elec}} = T_e + V_{ee} + V_{ext} \tag{2.7}$$

There are two main approaches to the solution of the equation. In ***ab initio calculations,*** a model is chosen for the electronic wavefunction and is solved using as input only the values of the fundamental constants and the atomic numbers of the nuclei. The accuracy of this principally depends on the model chosen for the approximation of wavefunctions. Because ***ab initio calculations*** are computational expensive to obtain accurate wave functions in case of large molecules, a second approach can be chosen, so called ***semiempirical methods.*** It simplifies the form Hamiltonian as well as uses the adjustable parameter with values obtained from experimental observations. In both cases, it is a challenging task to compute ***"chemically accurate"*** energies, which is within an error bar of 1 kcal/mol.

2.2 The Hartree-Fock approach

In the Hartree-Fock formulation electron-electron interaction of Equation 2.7 has been treated in an average way. This means, instead of calculating the repulsion for all electron pairs, one can calculate the repulsion between each electron and an average field of all other electrons. This converts the term V_{ee} only as a set of one-electron terms and writes the Hamiltonian as follows,

$$\mathbf{H_{elec}} = \sum_{i=1}^{N_{elec}} f(x_i) \qquad (2.8)$$

Where $f(x_i) = -\frac{1}{2}\nabla_i^2 - \sum_{A=1}^{N_{nuc}} \frac{Z_A}{r_{iA}} + v^{HF}(x_i)$

At this stage one must also introduce the concept of ***spin orbital,*** $\Phi_a(x_i; \mathbf{R})$, by considering spin of the electron. It is a product of an orbital wavefunction and a spin function and write the one electron Hartree-Fock Equation as,

$$f(x_i)\Phi a(x_i; \mathbf{R}) = \varepsilon_a \Phi a(x_i; \mathbf{R}) \qquad (2.9)$$

ε_a is the orbital energy of the spin-orbital and $f(x_i)$ is called the Fock operator,

$$f(x_i) = h(x_i) + \sum_u \{J_u(x_i) - K_u(x_i)\} \qquad (2.10)$$

In this expression, $h(x_i)$ is the core Hamiltonian for ith electron, the sum is over all spin orbitals u = a, b,.., z, and J_u is the **Coulomb operator** and K_u is the **Exchange operator.**

In restricted closed-shell Hartree-Fock formalism, individual spatial wavefunction Ψ_i is approximated by a linear combination of linearly independent basis functions which leads to ***Roothaan Equation*** **(2.11)** for the complete system. And this is solved in a *self-consistent* iterative approach to calculate the converged wave function and energies.

$$\boldsymbol{Fc} = \boldsymbol{Sc\varepsilon} \tag{2.11}$$

Where $\boldsymbol{F}$ is the **Fock matrix**, $\boldsymbol{S}$ is called **overlap matrix** of the basis functions, $\boldsymbol{c}$ is the coefficients for the linear combinations and $\boldsymbol{\varepsilon}$ is energies.

2.3 Density Functional Theory

About 40 years after L.H. Thomas[67] and E. Fermi[68] first used the density as a basic variable in the late 1920s, The Density Functional Theory (DFT) as it is known today, was born in 1964 when a landmark paper by Hohenberg and Kohn appeared in the Physical Review[69] as an alternative to HF method. The basic idea behind DFT is that the energy of an electronic system can be written in terms of the electron probability density *ρ*. For a system of n electrons, *ρ*(**r**) denotes the total electron density at a particular point in space **r.** According to the first ***Hohenberg-Kohn theorem*** the external potential V_{ext} of Equation 2.7 is said to be a functional of the electron density, denoted by E[ρ] (Equation 2.12). Integration over ρ(r) gives number of electrons n and determines other terms of Equation 2.7 T_e and V_{ee}.

$$E[\rho] = F[\rho] + \int v(\boldsymbol{r})\rho(\mathbf{r})d^3r \tag{2.12}$$

Where $F[\rho] = T_e[\rho] + V_{ee}[\rho]$. Second Hohenberg-Kohn theorem mentions that the functional that delivers the ground state energy of the system gives the lowest energy if and only if the input density is the true ground state density. However, the theorems do not tell us the form of the functional dependence of energy on the density. A year next in 1965, Kohn and Sham[70] proposed how to practically realize the DFT theory by introducing a computational framework to the most important part of kinetic energy

computation of the system. They showed that exact ground state electronic energy E of an n-electron system can be written as,

$$E[\rho] = -\frac{\hbar^2}{2m_e}\sum_{i=1}^{n}\Psi_i^*(\boldsymbol{r}_1)\nabla_1^2\Psi_i(\boldsymbol{r}_1)d\boldsymbol{r}_1 - \sum_{I=1}^{N}\frac{Z_I e^2}{4\pi\varepsilon_0 r_{I1}}\rho(\boldsymbol{r}_1)\,d\boldsymbol{r}_1 + \frac{1}{2}\int\frac{\rho(\boldsymbol{r}_1)\rho(\boldsymbol{r}_2)e^2}{4\pi\varepsilon_0 r_{12}}d\boldsymbol{r}_1 d\boldsymbol{r}_2 + E_{xc}[\rho] \qquad (2.13)$$

Where the one-electron spatial orbitals $\Psi_i(i = 1,2,\dots n)$ are the **Kohn-Sham** orbitals. The exact ground-state charge density ρ at $\boldsymbol{r}$ is given by,

$$\rho(\boldsymbol{r}) = \sum_{i=1}^{n}|\Psi_i(\boldsymbol{r})|^2 \qquad (2.14)$$

Where the sum is over all the occupied Kohn-Sham orbitals and is known once these orbitals have been computed. The first term of Equation 2.13 represents the kinetic energy of the electrons; the second term represents the electron-nucleus attraction with the sum over all N nuclei with index I and atomic number Z_I; the third term represents the Coulomb interaction between the total charge distribution (summed over all orbitals) at $\boldsymbol{r}_1$ and $\boldsymbol{r}_2$; the last term is the **exchange-correlation energy** of the system which is also a functional of the density and takes into account all nonclassical electron-electron interactions. The Kohn-Sham (KS) orbitals are found by solving the **Kohn-Sham Equations**. The KS Equations for the one-electron orbitals $\Psi_i(\boldsymbol{r_1})$ have the form of Equation 2.15 as below,

$$\left\{-\frac{\hbar^2}{2m_e}\nabla_1^2 - \sum_{I=1}^{N}\frac{Z_I e^2}{4\pi\varepsilon_0 r_{I1}} + \int\frac{\rho(\boldsymbol{r}_2)e^2}{4\pi\varepsilon_0 r_{12}}d\boldsymbol{r}_2 + V_{xc}(\boldsymbol{r}_1)\right\}\Psi_i(\boldsymbol{r_1}) = \varepsilon_i\Psi_i(\boldsymbol{r_1}) \qquad (2.15)$$

Where ε_i are the KS orbital energies and the exchange-correlation potential V_{xc}, is the functional derivative of the exchange-correlation energy:

$$V_{xc}[\rho] = \frac{\delta E_{xc}[\rho]}{\delta\rho} \qquad (2.16)$$

If E_{xc} is known, then V_{xc} is readily obtained.

The KS equations are solved self-consistently. The KS orbitals on each SCF iterations can be computed numerically or they can be expressed in terms of a set of basis functions. From the experience of HF methods, a variety of basis set functions can be useful to the choice of DFT basis sets. The computation time for a DFT calculation formally scales as the 3rd power of the number of basis functions.

The main challenge to predict chemically accurate energy of a chemical structure via DFT arises on the accurate approximation of E_{xc} . Several different schemes have been developed to increase the accuracy of it. The oldest and the simplest model is ***Local (Spin) Density Approximation*** (L(S)DA)[71], in which E_{xc} is an integral overall space with the exchange-correlation energy density at each point assumed to be the same as in a homogeneous electron gas density, this energy can be written as the sum of the exchange and correlation energies, Equation 2.17

$$E_{XC}^{LSDA}[\rho^{\uparrow},\rho^{\downarrow}] = \int d\boldsymbol{r}\rho(\mathbf{r})\left[\varepsilon_x^{hom}\left(\rho^{\uparrow}(\boldsymbol{r}),\rho^{\downarrow}(\boldsymbol{r})\right) + \varepsilon_c^{hom}\left(\rho^{\uparrow}(\boldsymbol{r}),\rho^{\downarrow}(\boldsymbol{r})\right)\right] \qquad (2.17)$$

The exchange part of the above Equation has been solved analytically, whereas the correlation part in the second term is obtained by Quantum Monte Carlo calculations[72,73].

To get more accurate definition of E_{xc}, local value of the gradient of the local density is added to the local values of it. These classes of comparatively complex DFT methods are known as ***generalized gradient approximations*** (GGA) and generally represented as in Equation 2.18.

$$E_{XC}^{GGA}[\rho] = \int \rho(r)\varepsilon_{XC}(\rho,\nabla\rho)dr \qquad (2.18)$$

where $\nabla\rho(r)$ is the gradient of electron density. Several GGA functionals have been developed till date to investigate different systems of interest. Among them, Perdew and Wang (PW91)[74], Perdew-Burke-Enzerhof (PBE)[75], BLYP[76,77] are the most common functionals. Different meta-GGA functionals (e.g., TPSS[78]) were developed considering the second derivative of the density and kinetic energy densities with

respect to space. They have shown better performance than LDA and GGA functionals in studies of molecular properties in the gas phase.

By adding the “exact exchange” contribution, obtained from the calculations using Hartree-Fock (HF), to the DFT exchange and correlation to reduce the self-interaction (interaction of an electron with itself) error, the hybrid functionals were developed. They constitute the fourth generation of the XC functionals, and B3LYP (with 20% HF exchange), PBE0 (with 25% HF exchange), M06 are examples of such functionals [79–83]. This work has been extensively used M06 as the hybrid-DFT functional to calculate all the energies in our work, hence the theory of it is only introduced briefly in this context in the next section.

2.4 Introduction to M06 – Minnesota Hybrid Functional

Over the years, a series of functionals, called the Minnesota group of functionals, have been developed by the Scientist involved in the group of Dr. Donald G. Truhlar from the University of Minnesota. Their main goal is to emphasize 5 different crucial areas such as main group thermochemistry (TC), barrier heights (BH), noncovalent interactions (NC), electron spectroscopy (ES), and transition metal bonding (TM) for developing the methods. The first functional, called M05[84], is designed to be as accurate as possible for the TM, MG, BH, and NC areas. The second one, called M05-2X[85], is designed only for main-group chemistry, to be good for the MG, BH, and NC areas. These two functionals are further optimized to develop M06 and M06-2X. The M06 functional is parametrized including both transition metals and nonmetals, whereas the M06-2X functional is a high nonlocal functional with double the amount of nonlocal exchange (2X), and it is parametrized only for nonmetals. The local parts of these 2 depend on three variables: spin density (ρ_σ), reduced spin density (x_σ) and spin kinetic energy density (τ_σ), where σ denotes the component along an arbitrary space fixed axis of electron spin angular momentum. The functional with high HF exchange are not able to describe transition metal-metal and metal-ligand bonding very well due to the presence of their multireference character in open shell configuration. Benchmarking on TMAE9, MLBE21 and 3dTMRE18 databases show the smallest minimum unsigned error (MUE) for the functionals M06, M06-L and M05 in the given order. Thus they are the three strongly recommended methods for transition metal chemistry.[83] Zhao and Truhlar[86] tested the binding energies of the four complexes of

the adsorption of isobutene on a large 16T zeolite cluster model and showed that M06-L, M06, M05-2X, and M06-2X are promising QM methods for the QM/MM simulation of zeolite catalysis. Paranthaman et al.[87] studied bond distance, vibrational frequency and atomization energy (AE) on a broad set of 3*d*-Transition metals mono nitrides (3*d*-TMNs) with several level of functionals. They also found some of the Minnesota functionals give good performance in this case. For example, M06-L, M06 and M05 generates bond distances within a mean deviation between 0.06 Å – 0.21 Å, whereas M06-L performs the best for structural and energetic properties. Among hybrid functionals, MPW91, B3LYP, M06 and PBE0 performed better to describe both bond distance and AE of 3*d*-TMNs. Extensive benchmark has been performed on Mo-Te-Nb-O M1 cluster model to understand which method can best describe our catalyst system and found that M06 is the method describing M1 catalyst suitable well. The details of this benchmark is described in chapter 3.

2.5 Van der Waals interaction

The van der Waals interactions E_{vdw} is the type of attraction or repulsion interaction between atoms when they are close to each other but not directly or weakly bonded. The van der Waals interaction includes the dipole-dipole (electrostatic interaction in a polar system), dipole-induced dipole (interaction between nonpolar and polar systems), and dispersion interactions. The general equation of the van der Waals interactions between two atoms (A and B) is,

$$E_{vdw}(R^{AB}) = E_{repulsive}(R^{AB}) - \frac{C^{AB}}{(R^{AB})^6} \qquad (2.28)$$

Where, R^{AB} is the distance between atom A and B, C^{AB} is a constant, $E_{repulsive}$ is the repulsive energy.[88] Dispersion interactions can be empirically defined as the attractive part of the van der Waals (vdW)-type interaction potential between atoms and molecules arises from the induced dipoles in atoms and molecules due to the fluctuations in the electron density. These fluctuations lead to interactions between the atoms or molecules that decay slowly with distance. For more than a decade, it is known that commonly used DFTs do not describe the long-range dispersion interactions correctly, especially for GGA and also some hybrid functionals.[89]

The method to treat dispersion interactions semi-classically and combine the resulting potential with a quantum chemical approach is known as DFT-D (DFT + dispersion) approach. The general form of dispersion energy which is simply added to the Kohn-Sham DFT energy is,

$$E_{disp}^{DFT-D} = -\sum_{AB}\sum_{n=6,8,10,\ldots}\frac{s_n C_n^{AB}}{R_{AB}^n} f_{damp}(R_{AB}) \qquad (2.28)$$

Where, sum is over all atom-pairs in the system, C_n^{AB} denotes the averaged (isotropic) nth-order dispersion coefficient (orders n = 6, 8, 10, …) for atom pair AB, R_{AB} is their internuclear distance, s_n is a DF dependent scaling factor. Both DFT-D and DFT-D2 are simple forms, including only n=6 in a 2-body term, whereas DFT-D3 includes n=6 and 8 in the 2-body term and a 3-body term called the Axelrod-Teller-Muto (ATM) triple-dipole variety.

2.6 Thermochemistry in Catalysis

DFT generates atomic scale electronic energy at low temperature of 0K. The connection between this microscopic measurement to the real-life macroscopic measurement of chemical reactions at high temperatures and pressure must be necessarily established. The theory of statistical mechanics especially plays the major role in this area by computing different thermodynamic quantity using the partition function, such as entropy (S), and Gibbs free energy (G). Within canonical ensemble and using established thermodynamics definitions, the Gibbs free energy at temperature T and pressure P is calculated from the combination of enthalpy (H) and entropy (S) using following Equation 2.27.

$$G(T,P) = H(T) - TS(T,P) \qquad (2.27)$$

2.8.1 Ideal Gas Assumption

The total partition function q_{total} can be represented as a contribution of translation, rotation and variational modes related to thermal motion of a chemical structure.

$$q_{total} = q_{translation} \times q_{rotation} \times q_{vibration} \qquad (2.29)$$

Ideal gas approximation for gas phase molecules and harmonic approximation for adsorbates on the surface has been applied in this work to calculate the different partition function in the scope of this work.

In ideal gas assumption, as the ensemble is non interacting with ideal gas, one can calculate three different energy components separately as follows,

$$q_{translation} = \left(\frac{2\pi m k_B T}{h^2}\right)^{\frac{3}{2}} V \tag{2.28}$$

where m being the mass, k_B the Boltzmann constant, h is the Planck's constant and V is the volume. Translation entropy S_{trans} can be obtained from Equation 2.28 as,

$$S^o_{trans} = R\left\{\ln\left[\left(\frac{2\pi m k_B T}{h^2}\right)^{\frac{3}{2}} \frac{V^o}{N_A}\right] + \frac{5}{2}\right\} \tag{2.29}$$

Where, superscript 'o' indicates that a 'standard state', meaning the volume occupied by one mole of ideal gas at 298 K and 1 atm pressure, namely $V^o = 24.5\ L$.

All diatomic or polyatomic gas molecules can have linear or non-linear mode of rotational partition functions. The rotational partition function for a linear molecule can be written as,

$$q_{rotation}(T) = \frac{8\pi^2 I k_B T}{\sigma h^2} \tag{2.30}$$

Where σ is 1 for asymmetric linear molecules and 2 for asymmetric linear molecules and I being the moment of inertia. Evaluation of entropy for this part can be written as,

$$S^{linear}_{rot} = R\left\{\ln\left(\frac{8\pi^2 I k_B T}{h^2}\right)^{\frac{3}{2}} + 1\right\} \tag{2.31}$$

The rotational partition function for nonlinear polyatomic gas species can be written as,

$$q_{rotation}(T) = \left(\frac{1}{\sigma}\right)\left(\frac{8\pi^2 k_B T}{\sigma h^2}\right)^{\frac{3}{2}} \pi^{\frac{1}{2}} I_x^{\frac{1}{2}} I_y^{\frac{1}{2}} I_z^{\frac{1}{2}} \tag{2.32}$$

The vibration mode of partition function consists of 3N-6 components for non-linear and 3N-5 components for linear molecules, where N is the number of atoms. Evaluation of the rotational components of the internal entropy using the partition function of Equation (2.32) for more typically encountered non-linear molecules gives,

$$S_{rot} = R\left\{\ln\left[\frac{\pi^{\frac{1}{2}} I_A^{\frac{1}{2}} I_B^{\frac{1}{2}} I_C^{\frac{1}{2}}}{\sigma}\left(\frac{8\pi^2 k_B T}{h^2}\right)^{\frac{3}{2}}\right] + \frac{3}{2}\right\} \tag{2.33}$$

And the remain partition function for molecular vibrations and corresponding entropy term can be expressed as,

$$q_{vib}(T) = \prod_{i=1}^{3N-6}\left(\frac{1}{1 - e^{-\frac{h\omega_i}{k_B T}}}\right) \tag{2.34}$$

$$S_{vib} = R\prod_{i=1}^{3N-6}\left(\frac{h\omega_i}{k_B T(e^{\frac{h\omega_i}{k_B T}} - 1)} - \ln\left(1 - e^{-\frac{h\omega_i}{k_B T}}\right)\right) \tag{2.35}$$

The upper limit changes to 3N-5 for linear molecule, ω_i is the i-th vibrational mode.

Within harmonic oscillator approximation, the energy of the lowest vibrational level can be determined as $\frac{h\omega}{2}$ where h is Planck's constant (6.6261 × 10^{-34} J s) and ω is the vibrational frequency. The sum of all these energies over all molecular vibrations defines the zero-point energy (ZPE). One may then define the ideal gas enthalpy at 0 K for a chemical structure to the relevant temperature as,

$$\mathrm{H(T)} = E_{elec} + E_{ZPE} + \int_0^T C_p\, dT = E_{elec} + \sum_i^{modes}\frac{1}{2}h\omega_i + \int_0^T C_p\, dT \tag{2.36}$$

where E_{elec} is the energy for the stationary point on the Born–Oppenheimer PES and C_p is the heat capacity and can be separated into translational, rotational, vibrational and electronic parts.

2.8.2 Harmonic Approximation

The translational and rotational modes for the strongly bounded adsorbates (e.g., propane, etc.) on catalytic surfaces can be neglected. Hence, the vibrational modes are the only possible degrees of freedom and are approximated as quantum harmonic oscillations. This allows calculation of internal energy U and entropy S as a certain

temperature T with the Helmholtz energy $F = U - TS$. If we can neglect the PV term in $H = U + PV$, then $F = G$. This means the Helmholtz free energy becomes the Gibbs Free energy. And within the harmonic limit one can use the following equations to calculate internal energy and the entropy of an adsorbate on the surface.

$$\mathrm{H(T)} = E_{elec} + E_{ZPE} + \sum_{i}^{harm\ DOF} \frac{h\omega_i}{(\mathrm{e}^{\frac{\mathrm{h\omega_i}}{k_B T}} - 1)} \tag{2.34}$$

$$\mathrm{S} = \mathrm{k_B} \sum_{i}^{harm\ DOF} \left(\frac{h\omega_i}{k_B T(e^{\frac{h\omega_i}{k_B T}} - 1)} - \ln\left(1 - e^{-\frac{h\omega_i}{k_B T}}\right) \right) \tag{2.35}$$

3. Computational Details

3.1 Benchmarking of DFT methods

Understanding which quantum chemical method works the best for a complex system like M1 turns out not to be a quite simple task. Several attempts to benchmark different GGA, meta-GGA, hybrid-DFT methods referenced with highly accurate coupled cluster (CCSD) have failed to give a proper definition of a simple benchmark oxidation reaction like Figure 3.1.

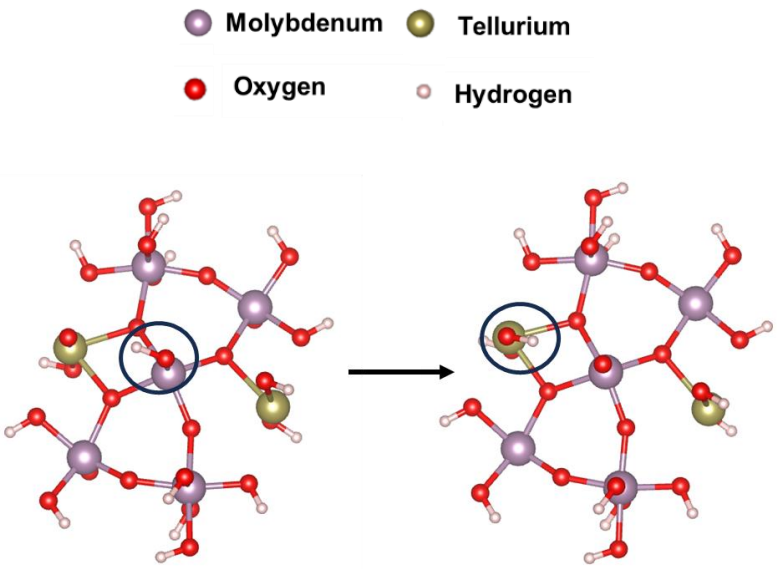

Figure 3.1. Benchmark reaction for H-migration (inside black circle) from central Mo-Oxo site to neighboring Te-oxo site on a 1-layer cluster model of the active site from Figure 4.6.

Stefan Grimme and coworkers[90] introduced the diagnostic tool based on fractional occupation DFT or finite temperature DFT and is called fractional occupation number weighted electron density (FOD). The diagnostic of five different surface configurations (Shown in Figure 3.2) shows significant delocalization of FOD for all of them. This indicates multi-reference characteristics of the cluster, hence it explains that single reference CCSD method cannot be used as reference for benchmarking.

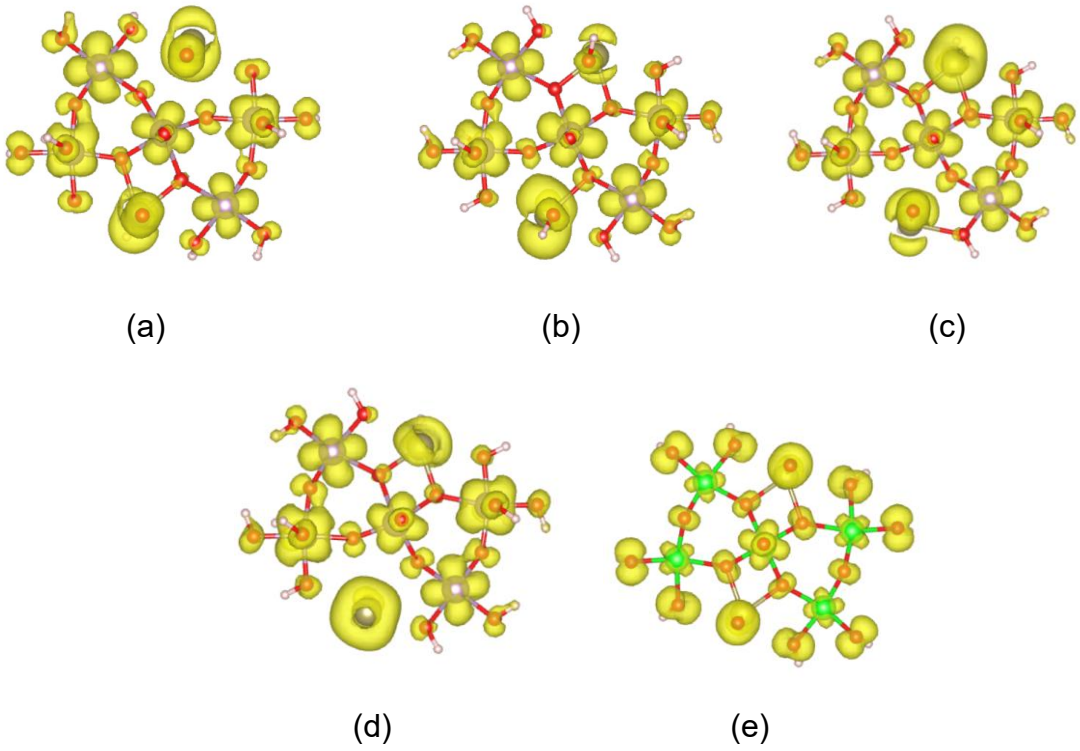

Figure 3.2. FODs of few different surfaces of the 1-layer active site for (a, b, c, d) Mo-only cluster model and (e) V-cluster (five V are in green) are shown here. They demonstrate that multireference nature is similar for all these surface configurations of the M1 active site.

Method	ΔE [kJ/mol]
CAS(4x4)SCF/def2-TZVP	-400
[DLPNO-] **NEVPT2(4x4)/def2-TZVP**	-388

Table 3.1. Reaction energies for the H-migration on the 1L active site cluster model shown in Figure 3.4 calculated with multireference methods using ORCA software package[91].

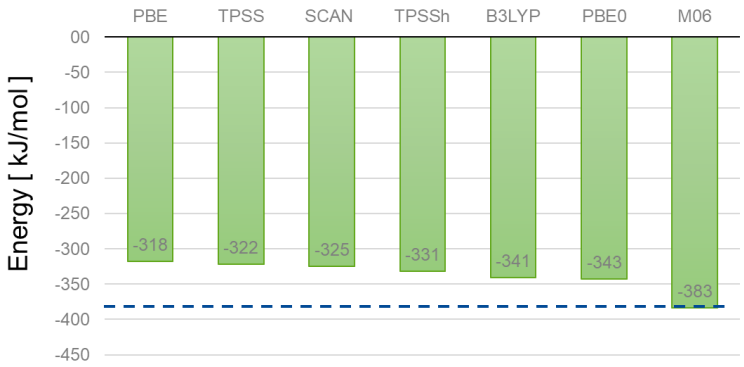

Figure 3.3. Comparison of different DFT functionals with the energy calculated with multi reference method presented in table 3.1. Blue Horizontal dashed line corresponds to NEVPT2-energy.

The reaction energy using multireference method [DLPNO-]NEVPT2(4x4)/def2-TZVP method is calculated as -388 kJ/mol, which has been used as reference (Table 3.1). Figure 3.3 shows the benchmark for different other functionals with same basis set def2-TZVP, compared to this where the dotted line represents the energy from NEVPT2. M06 turns out to be the best functional having lowest error of 5 kJ/mol, whereas other functionals have an error >10 kJ/mol. This confirms that M06 to be our choice of functional to calculate the final energies for this study.

3.2 Computational Detail

All DFT calculations for cluster models were performed using the quantum chemistry molecular code TURBOMOLE[92]. All geometry optimizations have been performed within the generalized gradient approximation (GGA) using the PBE functional[75,79], with split valence basis sets (def2-SVP)[93]. Single point energy calculations have been performed using the meta hybrid-DFT functional M06[83,94,95] (see SI for detailed analysis and benchmarking), triple-zeta valence basis sets with two sets of polarization functions (def2-TZVPP)[93] and higher convergence criteria of 10^{-7} with the optimized geometry. The Grimme D3 dispersion correction[96] was applied for all our calculations. Open shell calculations have been performed within the unrestricted Kohn-Sham framework[97]. Initial analysis of bulk model has been performed using Vienna ab initio Simulation Package software package (VASP)[98–100]

In order to investigate the thermodynamics of reactions in the gas phase, the structures of all conformers of the molecular reaction intermediates have been optimized within the framework of Density Functional Theory (DFT) using the hybrid meta-GGA functional TPSSh[101] and basis sets of valence triple-zeta quality (TZVPP[102]). For the optimized structures, single-point energies have been calculated using the hybrid meta-GGA functional M06[83,94,95], TZVPP basis sets and Grimme's D3 dispersion correction. Zero-point vibrational energies, thermal corrections for enthalpies, and molecular entropies have been determined for standard conditions (25 °C, 1 bar) in the rigid rotor / harmonic oscillator approximation using analytical second derivatives of the TPSSh energy with TURBOMOLE.

3.3 Active Site modelling of M1

The orthorhombic unit cell of M1 Mo-V-Te-Nb-O (ICSD-55097) contains 168 atoms with lattice parameters a = 20.385Å, b = 25.935Å and c =4.800Å after bulk optimization. Figure 1a shows the different surface motifs of 7-membered rings of Mo/V surrounding Te=O (F site), 5-membered rings of Mo surrounding Nb=O (E site), and a 4-membered motif surrounding a 2TeO (G site) and 1 Mo/V=O (B site) structure. 2 Nb ring site are connected via a Mo/V bridge (C, D sites) (Shown in Figure 3.4).

To establish the reference system of the study for propane activation, a Mo-only model containing Mo, Te, Nb and O, without any V is considered. There are three types of oxygen atoms in the bulk model, such as, 1. lattice oxygens connecting the metal sites to each other in plane, 2. oxygen atoms those are shared between two similar metals in between the layers and 3. oxygen atom residing in between the two layers but not shared, rather fully bound to one metal site from one of other layers. The number of these three types of oxygen that are bound to one metal, determines the oxidation states of the corresponding metal atom. In Figure 3.4a, all the unique metal sites on the unit cell of M1 are identified.

Site	Atom	Count	Ox. State	Charge
A1	Mo	16	+6	96
A2	Mo	4	+5	20
B	Mo	2	+5	10
C1	Mo	4	+5	20
C2	Mo	4	+5	20
D1	Mo	2	+5	10
D2	Mo	4	+5	20
E	Nb	4	+5	20
F	Te	4	+2	8
G	Te	4	+4	16
			Σ	240
	O	120	-2	-240

Table 3.2 Distribution of oxidation states for different transition metal sites on the unit cell of M1. The site on the left column is shown as in Figure 3.4a

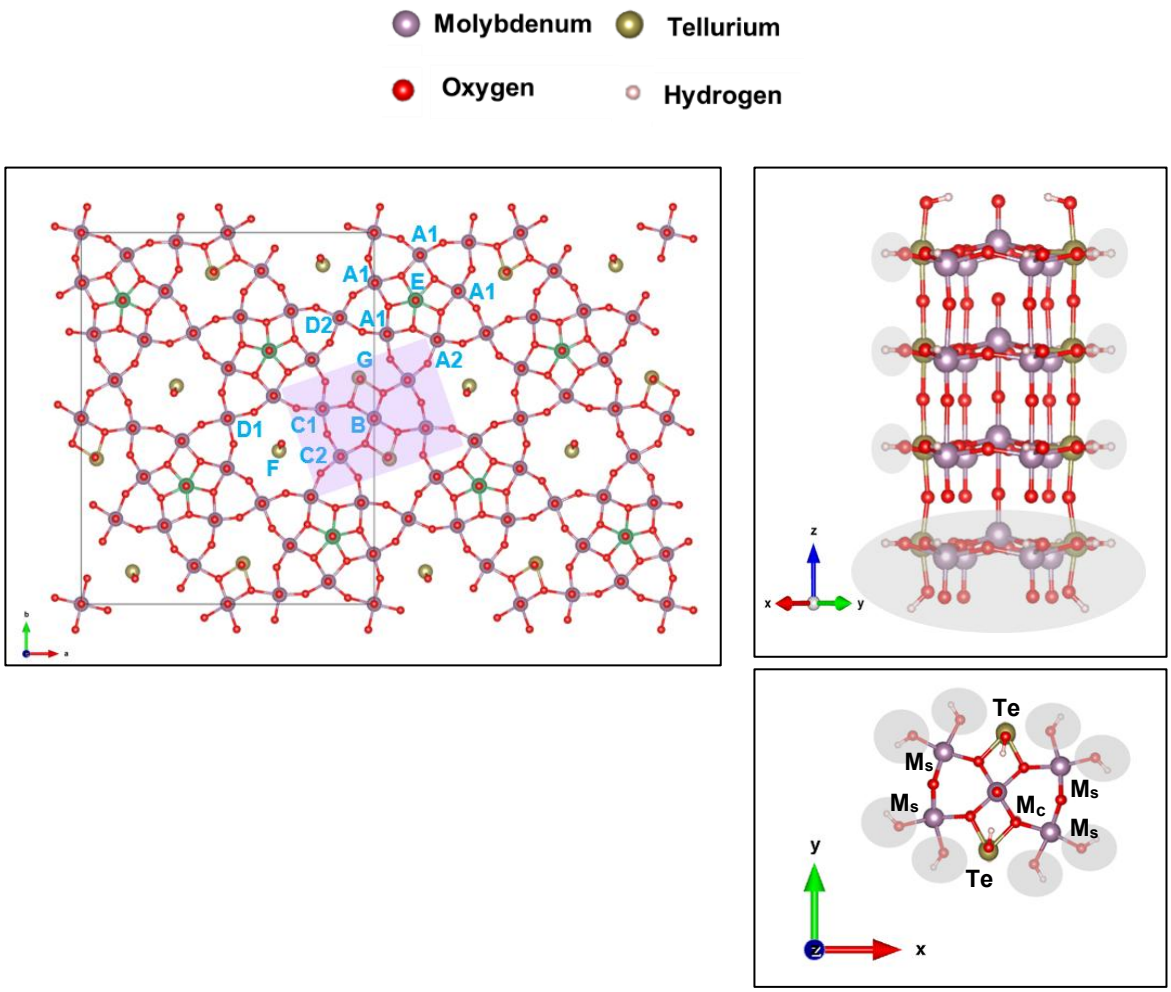

(a) (b)

Figure 3.4. (a) Top view of the (001) facet of the unit cell of MMO-M1 (Mo-V-Te-Nb-O) (ICSD-55097). Mo/V atoms are shown in violet, Nb in green, Te in yellow and oxygen are in red. A1, A2, B, C1, C2, D1, D2 are different unique Mo/V sites, E is for Nb and F, G are two different Te sites present. (b) side and top view of a 4-layer cluster model of the catalytically most active site consisting of C1, C2, B and G sites (highlighted by light lavender rectangle in a) with broken bond termination by OH groups (frozen atoms in the calculations are marked by greyed circles)

To understand the oxidation states of different metal sites, metal-oxygen bond distances are analyzed, which resulted in a distribution of oxidation states according to Table 3.2. According to these findings, Mo at A1 and A2 sites surrounding Nb have the oxidation states 6+ and 5+, respectively. Every other Mo atom (at B, C and D sites) is in the 5+ oxidation state. Te at sites F and G are 2+ and 4+, respectively. This is also consistent with the Bader charge distribution and unpaired spin analysis from periodically optimized bulk structure data, shown in Figure. 3.5. Significant unpaired

electron density at all 2+, 4+ and 5+ sites and almost no spin at Mo^{6+} sites confirms the assigned oxidation states shown in Table 3.2.

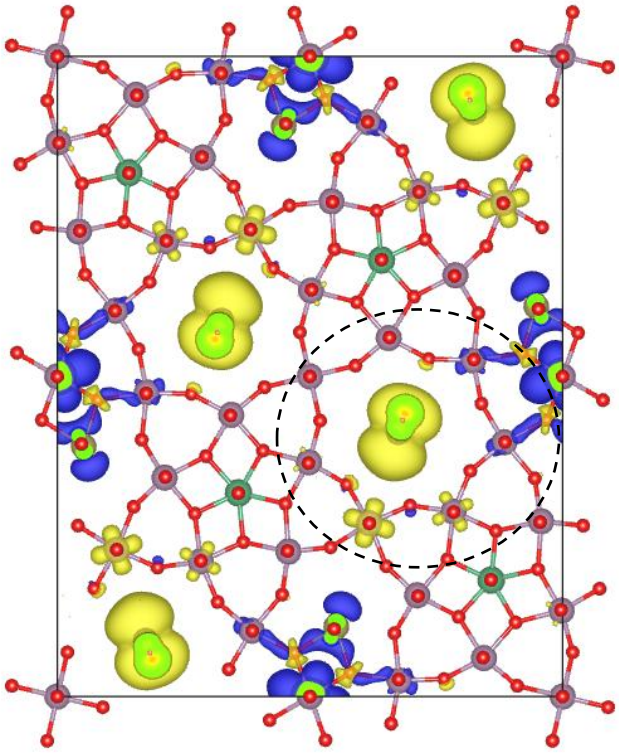

Figure 3.5. Spin density (UP Spin – DOWN Spin) from VASP on bulk model of M1 unit cell. iso-surface = 0.001, Spin density on Te inside 7-membered ring (inside the black dotted circle) in yellow indicates as Te^{2+} (site F). Similarly prominent spin density in blue/yellow in Mo/V (A1, A2, B1, B2, C, D1 and D2) and Te (site G) sites indicate the existence of Mo^{5+}/V^{4+} and Te^{4+} respectively. No spin at Nb site also confirms that it is Nb^{5+}.

According to Govindasamy et. al.[103], the function of the pentagonal Nb site is to stabilize the structure and provide active site isolation for catalytic reactions. The active site[17,18,24] is chosen such that it consists of C1, C2, B and G metal sites (rectangular light magenta zone of Figure 3.4). All broken metal-oxygen bonds at the edge of the cluster have been terminated by hydrogen atoms with the common OH distances of 0.97 Å[104] and with an orientation in the direction of the replaced metal centers. The in-plane terminating OH groups have been kept fixed during all structure optimizations (circular greyed part of Figure 3.4b).

Four different oxidation energies shown in Table 3.3 are calculated for the cluster with 2, 3, 4 and 5 layers (Figure 3.6). Bader charge analysis and spin density on central Mo atoms of the multilayer clusters (Figure 3.7, 3.8) are also performed. All of these properties converge well with a 4-layer model, which is then chosen as a working

model of the active site of the M1 catalyst. All atoms in the lowest layer were kept frozen during optimization (greyed parts in Figure 3.4a). The one layer of active site is

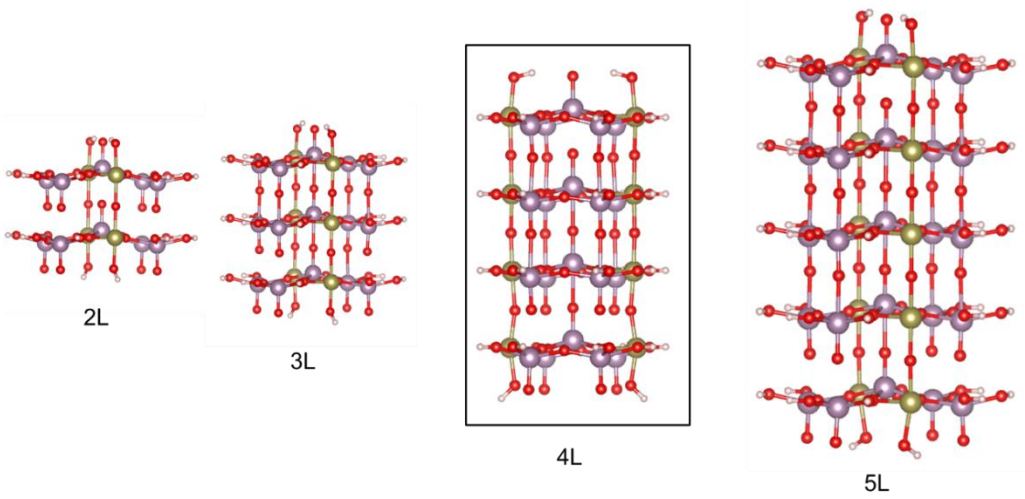

Figure 3.6. Here systematic addition of layers of the active site cluster model is shown. Various oxidation reaction reactions are performed as shown in Table3.3 on these models to understand how many layers are required for accurate modelling to capture all electronic phenomena.

Oxidation reactions	2 Layers (kJ/mol)	3 Layers (kJ/mol)	4 Layers (kJ/mol)	5 Layers (kJ/mol)
* + OH* + OH* + 0.5O_2 → OH* + OH* + O*	-121	-127	-121	-129
* + OH* + OH* + O_2 → OH* + OH* + O* + O*	-193	-198	-223	-219
* + OH* + OH* + 0.5O_2 → * + O* + O* + H_2O	44	14	-27	-23
* + OH* + OH* + 2O_2 → * + OH* + OH* + (O-O)* + (O-O)*		-33	-32	

Table 3.3 Oxidation Energies when O-atom, 1 and 2 O_2 molecules adsorbs on the surface metal sites of the cluster model with 2, 3, 4 and 5 layers (shown in Figure 3.8) of M1 active sites are presented here. All the energies converge at 4th layer configuration indicating the necessity of minimum 4-layer model of the active site.

Mo_5Te_2 cluster. It has one central Mo (denoted M_c) and four symmetry equivalent side-Mo (denoted M_s, see Figure 3.4b). Two Te are attached to the oxygen atoms bridging M_c. and M_s. It is generally found that oxygen (and hydroxyl) binds on these in energetic order M_c, Te, M_s, with M_c having the strongest Mo-O bond.

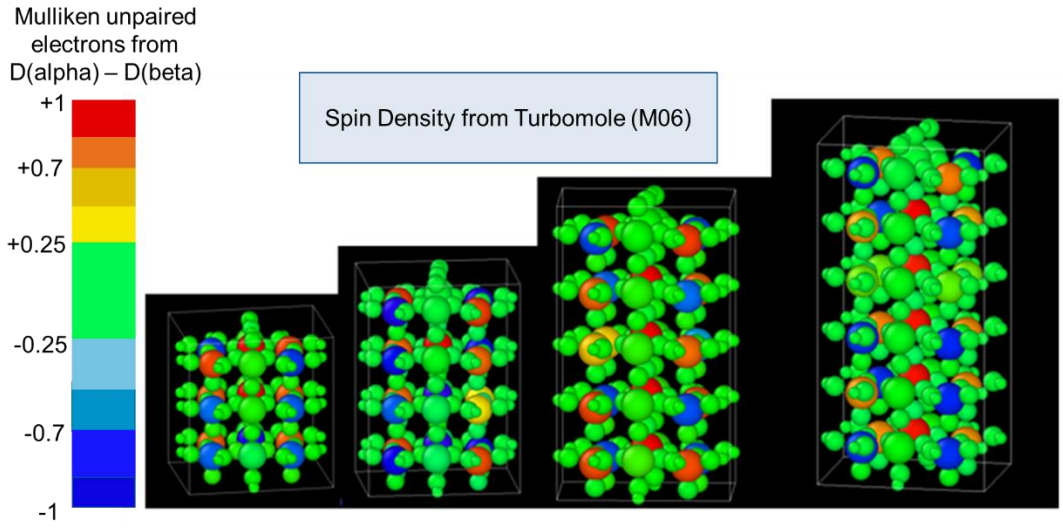

Figure 3.7 Mulliken spin density on metal sites at active sites with 2, 3, 4 and 5 layers of cluster model. The location of unpaired spin (UP or DOWN) remains the same from 4-layer model and onwards. But they can have opposite signs indicating a spin flip.

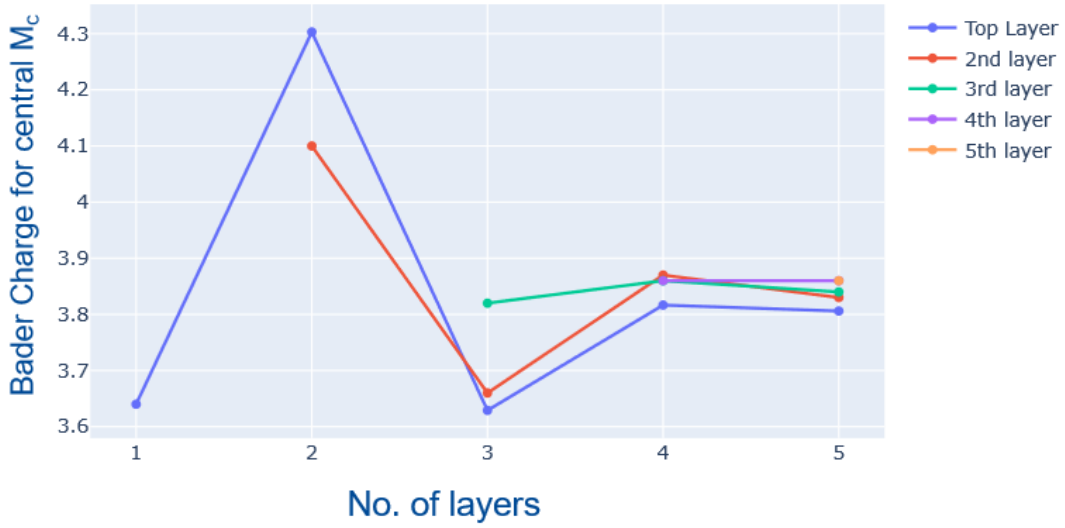

Figure 3.8 Bader charge plot on central Mo sites at each layer of 1-, 2-, 3-, 4- and 5-layers cluster model respectively. It shows that all the charges at M_c as one of the electronic properties, converges at 4^{th} layer model and stays constant to 5^{th} layer.

4. The full catalytic cycle for the selective oxidation of propane to propylene on the M1 phase of Mo-Te-Nb-O catalysts

4.1 Introduction

The activation of C-H bonds constitutes the first step for the functionalization of hydrocarbons towards higher value chemicals. Usually, this activation is achieved through co-feeding of oxygen which often also leads to oxygenated products, that play an important role as a feedstock for many chemicals. However, these oxidation processes need to be highly selective, as one would otherwise obtain undesired side-products and here in particular CO_2. Devising heterogeneous catalysts that are highly selective is thus a crucial prerequisite for implementation in the chemical industry[105,106]. One example is given by the industrial conversion of propane to acrylic acid over the M1/M2 phase of a Mo-V-Te-Nb-O mixed metal oxide catalyst.[8,27,30,41,44,107–116] This catalyst has shown 61% selectivity for the conversion of propane to acrylic acid[42,47,117,118] at 380 ºC. Selective oxidative dehydrogenation of both ethane and propane can also be achieved with this catalyst.[43,39,119]

An extensive study invoking a full catalytic cycle employing the entire active site is missing to date. This being the aim of the current study, our focus is on the Mo-only model as a starting point such that a simple reaction scheme covering the entire catalytic cycle can be established. More realistic catalysts typically incorporate one or more V atoms[18] the location and influence on the catalytic activity are not being fully understood to date. As this adds much more complexity, depending on the location of the V atoms, a Mo-only model here as a starting point is used, future work explores the influence of V substitution.

This chapter is based on the following publication:

K. Sen, A. Schäfer, F. Rosowski, D.I. Sharapa and F. Studt, J. Phys. Chem. C 2024, 128, 34, 14273–14281

This **Mo-only** model is used to investigate the oxygen activation, surface dynamics and oxidation of propane to propene as the first important reaction step of propane functionalization. Based on extensive density functional theory (DFT) calculations, this work suggests for the first time the reaction energetics of a full catalytic cycle that also includes the activation of O_2 and the production of water.

4.2 Surface oxidation and dynamics

Investigation of the surface composition under reaction conditions of the cluster active site model is shown in Figure 3.4b. All possible surface coverages with O and OH are calculated and the phase diagram as a function of the oxygen chemical potential is shown in Figure 4.1a. The surface oxidation state (SOX) for a certain surface configuration is calculated using the following formula,

$$SOX = 2*\eta_O + \eta_{OH}$$

Where η_O = No. of Oxygen on M_s or Te and η_{OH} = No. of OH on the surface.

In the following, the surface configuration is labelled with the SOX as the first digit followed by a letter denoting its energetic ranking in alphabetical order (Figure 4.1b). For example, surface **4b** has a SOX of 4 and is the second most stable surface in that SOX category. The investigation is extended to which the hydrogen atoms at the hydroxyl groups are mobile and that diffusion barriers (hydrogen migration from one O to the nearest neighbor O) are relatively small, typically being less than 20 kJ/mol. Importantly, hydrogen diffusion to a hydroxyl group (OH*) producing a water molecule is similarly fast. Two transition state structures for such investigation have been shown in Figure 4.2. Hence the conclusion is that the catalyst surface is always in its thermodynamic equilibrium with respect to the O-bound H atom distribution under reaction conditions, as well as with the dissociation of water to OH and H (on a second O atom). All structures and their energies are shown in tables AT1 and AT3 in the appendix, here the focus is on the most relevant one from the energetic point of view. The blue dotted line in Figure 4.1a shows the most favorable surface oxidation/reduction path connecting the **2a, 4a** and **6a** configurations, whereas other configurations such as **6e, 6b, 6c, 4b** and **2b** either isomerizes via H-migration or desorb and reabsorb water to achieve the most stable surface states on the blue line.

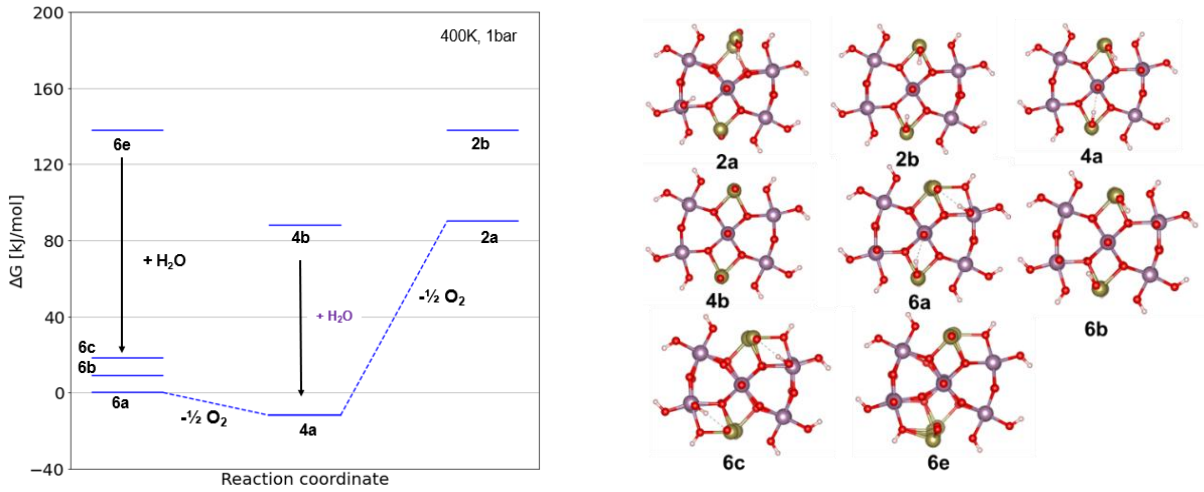

(a) (b)

Figure 4.1 (a). ΔG profile of consecutive reduction of the cluster surface at 400K, and 1 bar pressure of oxygen and water. For each SOX category, the Gibbs free energy levels of different OH distributions and different amount of chemisorbed H_2O (4b and 6e) are shown (b) Top view of the active site structures

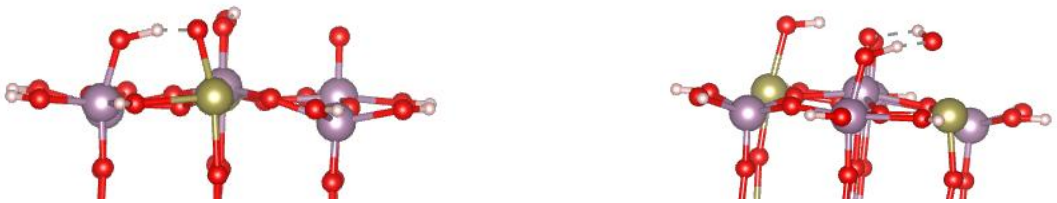

(a) (b)

Figure 4.2. (a) TS structure for hydrogen migration from Mo-O to Te-O site with enthalpic activation barrier of 15 kJ/mol, (b) TS structure for hydrogen migration from Mo-O to Te-OH site and desorbs water molecule with enthalpic activation barrier of 13 kJ/mol

4.3 Mechanistic Routes to Propylene from Propane

The reaction to study for full catalytic cycle is the selective oxidation of two propane molecules with molecular oxygen to generate two propene and two water molecules (Eqn. 4.1)

$$2C_3H_8 + O_2 = 2C_3H_6 + 2H_2O,\ \Delta G_r = -303\text{kJ/mol (M06-D3/def2-TZVPP)} \quad (4.1)$$

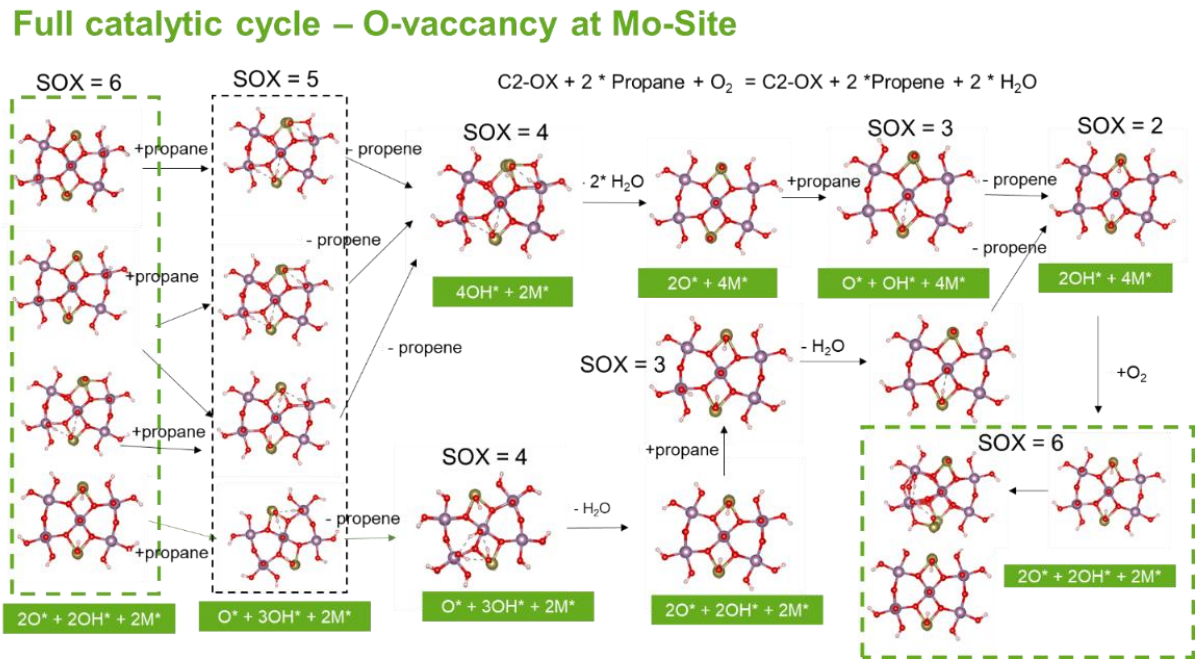

Figure 4.3 All possible pathways for full catalytic cycle consisting of consecutive oxidation of two propane molecule to form two propylene and two water molecules where O-vacancy due to water desorption takes place only at Mo site are shown here. The first propane activation occurs at surface with SOX=6 and the consecutively reduced to ensemble of surfaces with SOX=2, where they are re-oxidized by O_2 to complete the catalytic cycle.

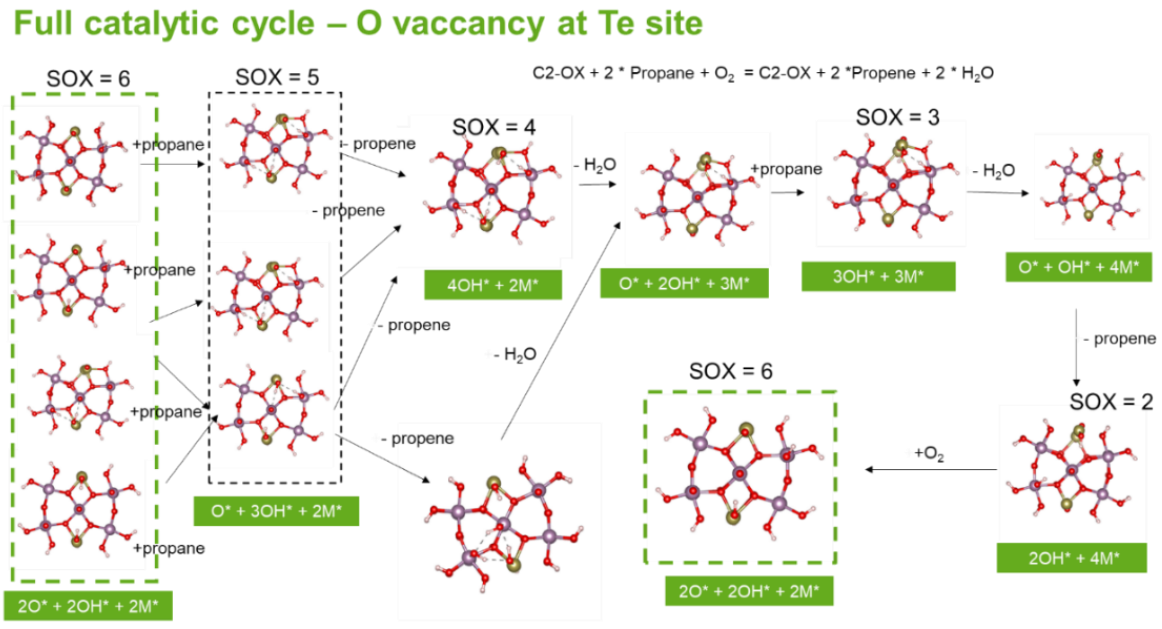

Figure 4.4 All possible pathways for full catalytic cycle consisting of consecutive oxidation of two propane molecule to form two propylene and two water molecules where O-vacancy due to water desorption takes place only at Te site are shown here. The first propane activation occurs at surface with SOX=6 and the consecutively reduced to ensemble of surfaces with SOX=2, where they are re-oxidized by O_2 to complete the catalytic cycle.

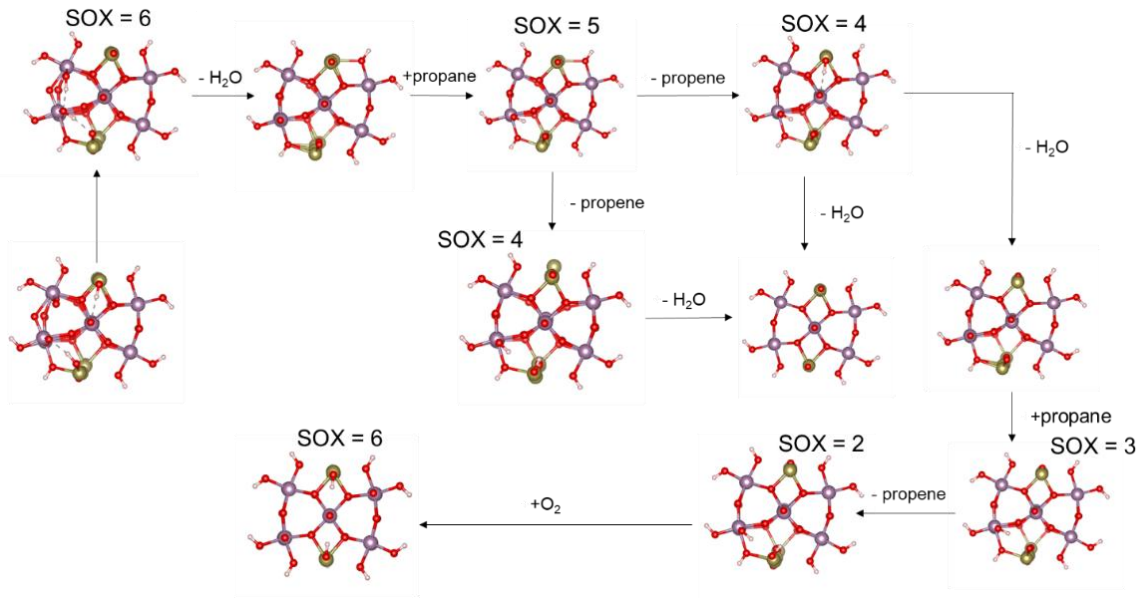

*Figure 4.5 All possible pathways for full catalytic cycle consisting of consecutive oxidation of two propane molecules to form two propylene and two water molecules starting from surface **6f** where the oxygen molecule has been activated at two neighboring Mo sites at same bridge side of the active site.*

Given the thermodynamics of surface oxidation, the successive catalytic oxidation of two propane molecules with molecular O_2 cycles between a SOX of 2 and 6, is a 4-electron process. SOX 6 is chosen to be the starting point for the activation of propane, with structure **6a** being the most stable thermodynamic configuration.

However, as the configurations with higher free energy could also be considerably populated under reaction conditions, the activation of propane on all possible structural models as well are considered. Three different cases of how the reaction can occur on the cluster surface in this full catalytic cycle are investigated. Figure 4.3 shows first possibility, where water desorption from the surface creates O-vacancy at the Mo sites. Figure 4.4 represents the possible pathways where the water desorption creates O-vacancy at Te-site. Starting structures for both possibilities are **6a**, **6b**, **6c**, and **6d**.

Another possibility is to start from the surface **6f** where oxygen molecule has been activated and adsorbed on two neighboring Mo sites on the same side of the cluster. This leads to another pathway which is shown in Figure 4.5.

4.3 Linear Scaling for M1

Earlier theoretical studies established that the transition state energy of C-H bond activation scales linearly with the binding energies of a hydrogen atom on the respective surface oxygen, denoted E_H, with a slope of 0.75.[59] This observation has been made for radical-like transition states of hydrocarbon activation over a range of materials including oxides, and been investigated mostly for the case of methane, but ethane activation has been found to obey a similar universal scaling relation. Busch et al.[120] has benchmarked the linear free energy scaling relationships (LFESR) among binding energies of *-OH, *=O, *-OOH (intermediate species for oxygen evolution reaction (OER)) on different solid and molecular catalysts with several DFT functionals against GMC-QDPT2, a multiconfigurational method based on relativistic quasi-degenerate perturbation theory[121,122]. According to them, hybrid functional with less amount of exact exchange have minimum error and typically under bind the intermediates. Among them, M06 and PBE0 are the best performing hybrid functionals besides less expensive M06-L, to describe linear scaling for OER. Numerous transition states are calculated, dealing with the activation of propane (primary and secondary carbon atom) and the H-abstraction from propyl. Optimized transition state geometries and related reaction barriers for the activation of the secondary carbon are shown in Figure 4.6.

As can be seen barrier heights are on the order of 60 – 100 kJ/mol for the structures investigated. Note that the activation of the primary carbon has always a somewhat higher activation barrier, as one would expect (data given in the appendix in table AT4). Recent work from Yu et al.[24] also established a linear relationship between the C-H activation energy and the hydrogen binding energy (ΔE_H). They, however, observed a much wider range of activation energies (from 80 to 200 kJ/mol) and a scaling with a slope of 1 at the GGA level of theory (Figure 4.7a). Contrary, other work calculated a slope of 0.6 for the same reaction albeit on V_2O_5 and V_2O_5/TiO_2 (Figure 4.7b) for the Catalyst.[51,123]

An analogous scaling relation has been found here, but having a slope of 0.75 along the lines of what has been reported for methane, ethane and methanol activation over a wide range of catalysts.[59] Therefore the scaling with a slope of 0.75 identified herein to estimate reaction barriers for all reaction steps is employed. The difference in

intercepts is the difference in molecular C-H bond energies of 18.6 kJ/mol (Figure 4.8) and the line fits the calculated data points very well (data points in magenta in Figure 4.8).

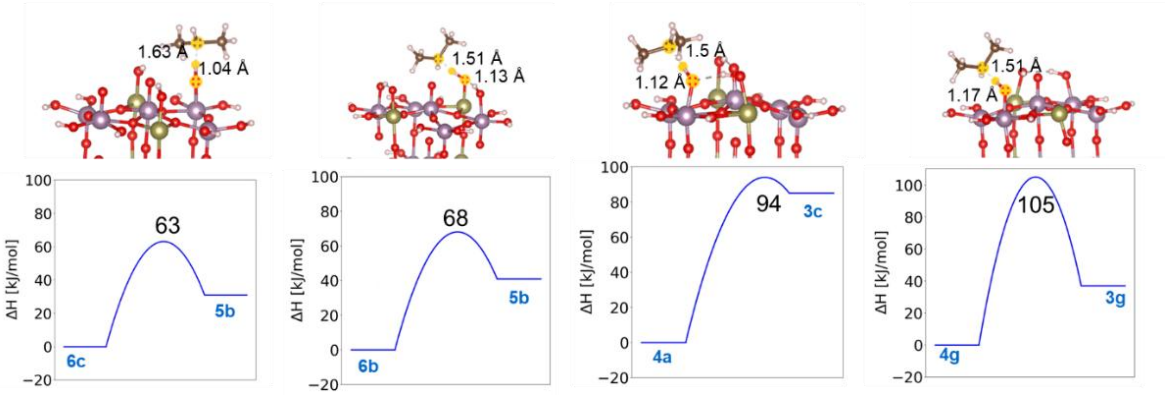

Figure 4.6. Activation barrier for propane (M06-D3/def2-TZVPP) at the central carbon atom on four different surface configurations ***6c->5b*** *(63 kJ/mol),* ***6b->5b*** *(68 kJ/mol),* ***4a->3c*** *(94 kJ/mol),* ***4g->3g*** *(105 kJ/mol) from left to right. TS structures with C—H—O bond distances are shown on top.*

All the four transition states for propane activation are shown in Figure 4.6. The first C-H bond activation produces a propyl radical. The second C-H activation of the propyl radical generally, find much lower barriers, again in line with the much lower C-H bond strength of the propyl radical (being 180 kJ/mol). The difference in C-H bond strength between activating terminal C-H bond in gas phase propane and propyl is 270 kJ/mol (see table AT5 in appendix). The yellow line which is 144 kJ/mol lower than the magenta line, fits the propyl data points well. This smaller activation barrier can be explained by the stabilization of propyl radical on the surface M=O site and activating the C-H bond at terminal site, which makes the activation barrier higher compared to the gas phase C-H bond strength difference. Thus, the hydrogen binding energy (ΔE_H) can be used as a descriptor for C-H activation over the investigated catalyst models. Calculations of entropy contributions at the transition states reveal that these are roughly similar among the structures investigated here (see table AT1 in appendix for details) and hence they are kept constant for the same C-H activation processes.

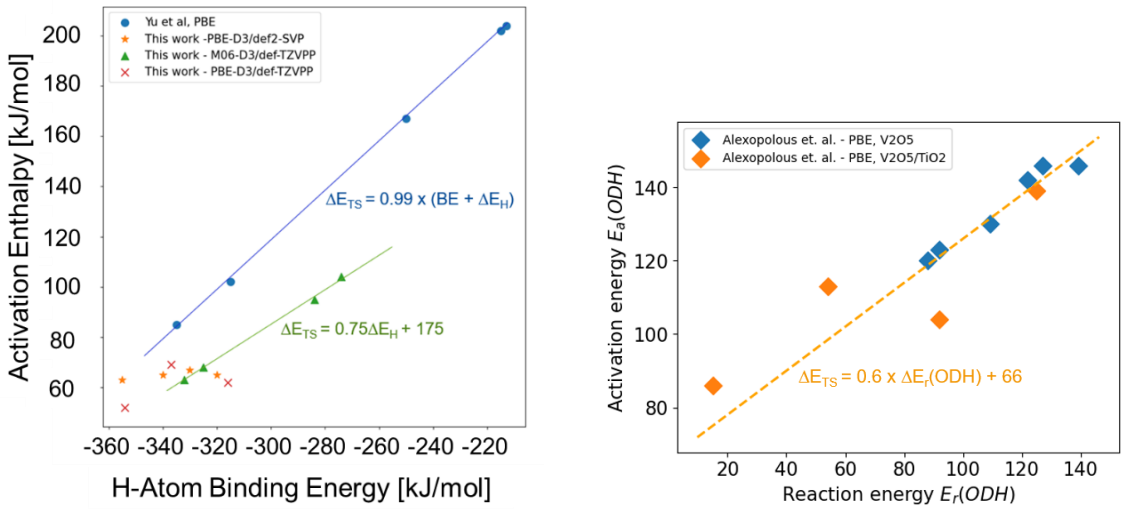

(a) *(b)*

Figure 4.7 (a) Data for propane activation barrier (E_{TS}) and hydrogen atom binding energy (E_H) from Yu et. al.[24](Green points) and from this work utilizing 3 different level of theories (PBE-D3/def2-SVP, PBE-D3/def2-TZVPP, M06-D3/def2-TZVPP). (b) BEP relation using the reaction energy, activation energy data published by Alexopoulus et. al.[51,123]

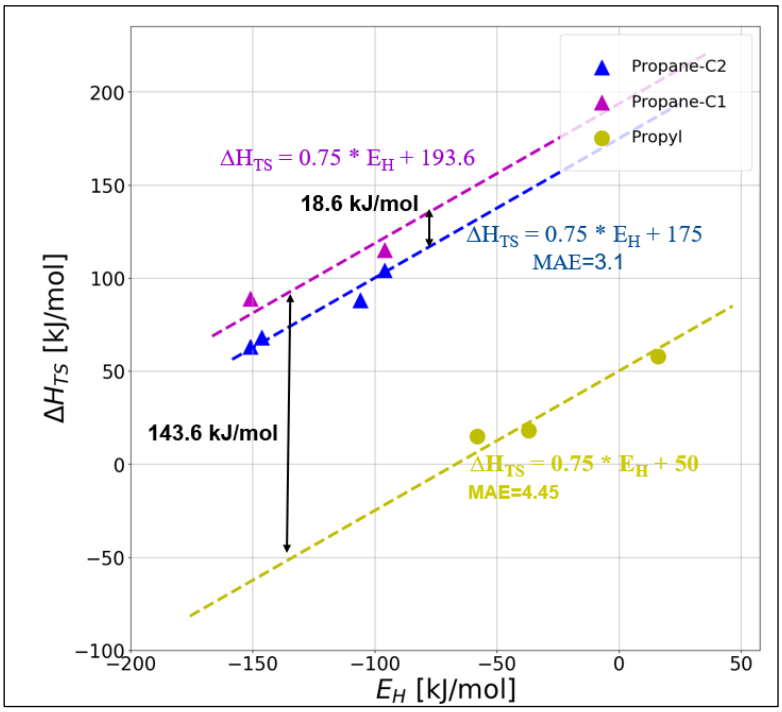

Figure 4.8 Linear scaling lines for H abstraction at C1 of propane (purple line), for H abstraction at C2 (blue line) and for H abstraction at C1 of propyl (yellow line) on the M1 catalyst between E_H and H_{TS} for 5 Mo on the surface. The enthalpy differences between different lines are shown with black arrows.

4.4 The Full Catalytic Cycle

Using the scaling relations shown in Figure 4.8, the full catalytic cycle of the conversion of two propane molecules and molecular oxygen is presented. Figure 4.9 shows the resulting free energy diagram at a temperature of 400 K and a pressure of 1 bar. The starting point is the fully oxidized surface (SOX=6), which reacts with one propane to create propene and a surface with SOX=4. After conversion of another propane to propene, the resulting surface (SOX=2) is re-oxidized using molecular oxygen, thus establishing a full catalytic cycle (Figure 4.10). As discussed above, the assumption is here that, due to low barriers of hydrogen diffusion, all surfaces are in thermodynamic equilibrium, including the adsorption and desorption of water. The obtained final minimum free energy pathway with activation barriers is shown in Figure 4.10.

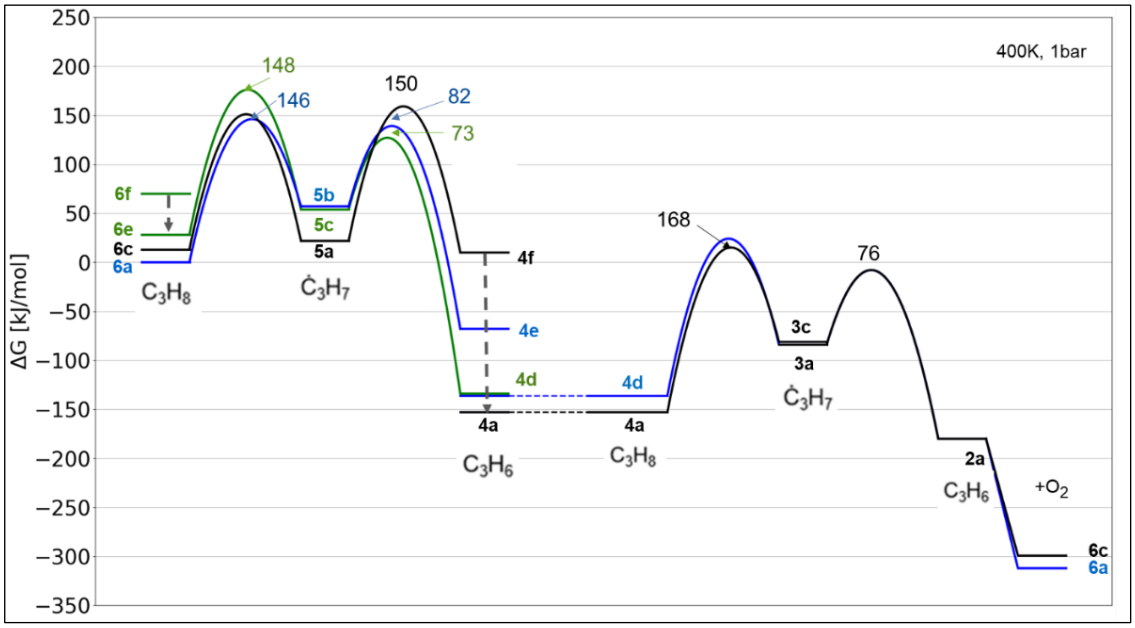

Figure 4.9. Free energy diagram for the full catalytic cycle of oxidation of 2 propane molecules to 2 propylene and 2 water molecules at 400K and 1 bar. All energies are given relative to ideal gas phase propane, propyl or propene molecules and catalyst. ***6a*** *is the initial structure and has the lowest propane activation barrier of 146 kJ/mol (blue) to* ***5b****.* ***5b*** *desorbs water to* ***5d*** *which has the lowest activation barrier of 73 kJ/mol for propyl to propene (green line) to* ***4d****.* ***4d*** *is stabilize to* ***4a*** *via H-migration. A high second propane activation barrier of 168 kJ/mol is observed at* ***4a*** *to* ***3c****, followed by water desorption to* ***3a*** *and propyl activation to form the second propene molecule on* ***2a****.* ***2a*** *is oxidized by* O_2 *to form* ***6a*** *to complete the catalytic cycle. Activation barriers are estimated from the linear scaling relations in figure 4. The black dotted arrows correspond to water desorption.*

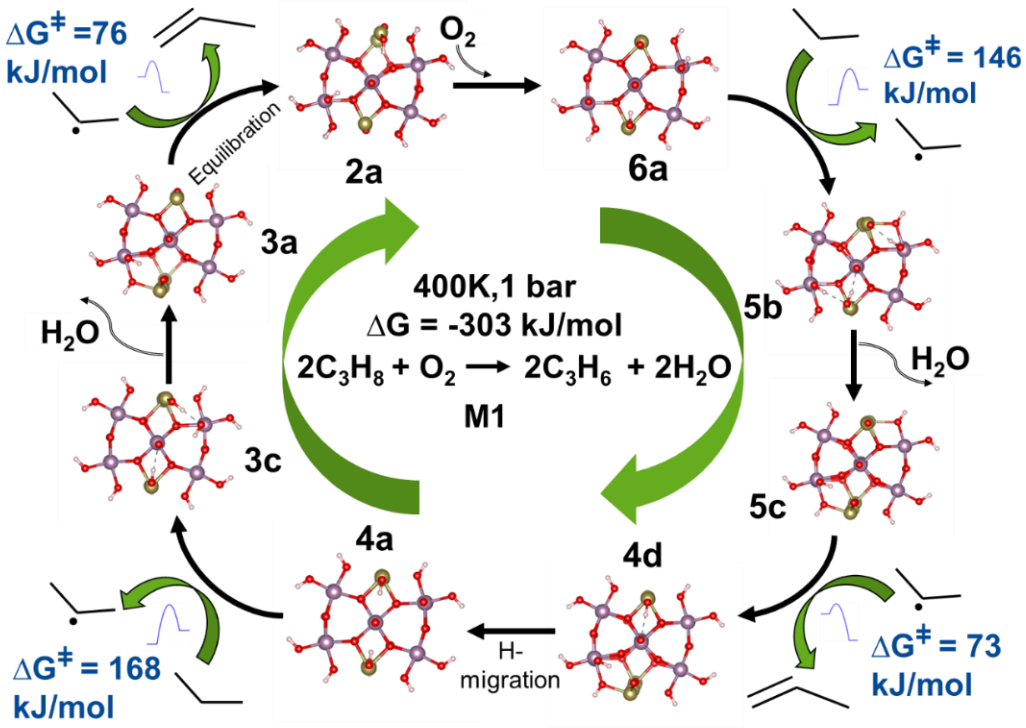

Figure 4.10. The final minimum energy pathway is summarized from figure 4.9 of the full catalytic cycle of oxidation of 2 propane molecules to form 2 propylene and 2 water molecules. The top view of the surface states, their id and 4 activation barriers are shown here.

Figure 4.9 shows the minimum energy pathways for C-H activation of the central carbon of propane, as this is always lower in energy than for the terminal carbon. The black and blue lines are the pathways where water desorption from **4f/4e** to **4a** create an O-vacancy at a Mo-site, whereas the green line starts from dissociative adsorption of an O_2 molecule in neighboring M_c sites (**6f**) followed by a water desorption to **6e**. The first reaction free energy barrier is 123 kJ/mol (TS1, blue line). After that, the propyl radical reacts further with a barrier of about 100 kJ/mol (TS2, green line), when referenced to the preceding propyl radical. This leads to surfaces with the SOX=4. Equilibration (through water desorption) yields structure **4a** as being most stable under the chosen reaction conditions. This process is about 150 kJ/mol exothermic. The activation of a second propane over **4a** has a barrier (TS3) of 145 kJ/mol, followed by conversion of the propyl radical with a barrier of 80 kJ/mol when referenced to the preceding propyl radical. This process is only exothermic by 20 kJ/mol after equilibration to the most stable surface (again accompanied by water desorption).

Importantly, the surface of **2a** has only M_s, such that there is space for the splitting of molecular O_2 along the Mo-O-Mo axis. This process is calculated to be exothermic by 150 kJ/mol. This last step concludes the full catalytic cycle, establishing again surface

6a. The highest barrier in the entire reaction mechanism is thus the activation of the second propane, being 145 kJ/mol. Using the energy span model[124], this yields a rate of about 1.09 x 10^{-5} s^{-1} at 150°C, keeping in mind that the typical error from DFT calculations is +/- 2 orders of magnitude at this temperature[47], however, that our model does not contain any V atoms in Mo-sites. How these influences the reaction barriers are outside the scope of the current contribution and are dealt with in subsequent work.

4.8 Conclusion of the Chapter

In this chapter, a full catalytic cycle for the selective oxidation of propane to propene on the M1 phase of the Mo-Te-Nb-O catalyst is established. This was aided through establishing linear scaling relations using a simple descriptor such as the hydrogen binding energy. Importantly, it is found that the intercept of the scaling is dependent on the C-H bond strength, opening avenues to predict scaling lines without any transition state calculations. Scaling line says activating the CH bond of second carbon of propane is the most favorable than other two carbon. Later exploration of all possible surface configuration and reaction paths on the active site for propane oxidation to propylene have been presented. The full catalytic cycle has been established for oxidation of two molecules of propane to form two molecules of propylene and water and the minimum energy path with most stable surface configurations have been depicted out of it. It shows that even though it can activate the first propane on a high oxidized surface with a comparatively lower activation barrier, the Mo only catalyst is comparatively inactive due to the high C-H activation barrier for the second propane molecule activation on a reduced surface.

5. Understanding the Selectivity of Propane Partial Oxidation to Acrylic Acid on M1 phase of Mo-Te-Nb-O Catalyst

5.1 Introduction

Deeper oxidation of propylene produces various unwanted species such as acetic acid, CO or CO_2[42]. The formation of acetic acid occurs via degradation of acrylic acid[125] or via oxidation of acetone generated propylene via isopropanol in presence of surface -OH species[126,127]. However, Naumann d'Alnoncourt et. al.[42] observed that acetone is not a major by-product of propane or propene oxidation. Acetone can only be detected at low conversion of propane, for conversions above 10% selectivity to acetone is often below 1%. For propylene as a feed, an increase of acetone selectivity towards 10% has been observed with increasing steam feed from 10% to 40%. Kube et. al.[43] reported that activation of propane to propene on M1 starts at low temperature (120°C), hence the first C-H activation of propane is not the main issue for M1 for producing valuable chemicals. They also reported production of several intermediate gas species and overoxidation to CO/CO_2 with increasing reaction temperature (100 - 400°C). Their proposed reaction network over catalytic surface shows that propylene can be oxidized at all three carbon atoms to produce different oxygenated products. A selective pathway towards acrylic acid needs oxidation of the allyl carbon atom to form allyl alcohol and acrolein as the intermediates.

In this chapter, the focus remains on the Mo-only model (shown in Figure 4.1) as a starting point such that a simple scheme covering all the reactions can be established. We have continued to investigate the reaction network starting from propyl radical followed by propylene towards acrylic acid.

This chapter is based on the manuscript in Review:

K. Sen, A. Schäfer, F. Rosowski, D.I. Sharapa and F. Studt; "Understanding the Selectivity of Selective Oxidation of Propane to Acrylic Acid on Mo-Te-Nb-O M1 Catalyst using Density Functional Theory"

The model of the linear scaling relation (LSR) for propylene and allyl alcohol is extended to cover all the relevant gas phase intermediates.

The four selective reactions such as, propane to propylene (Rxn-1), propylene to allyl alcohol (Rxn-2), allyl alcohol to acrolein (Rxn-3), acrolein to acrylic acid (Rxn-4) and one unselective reaction that is propane to isopropanol are studied in this work (as shown in Figure 5.1). Finally, the minimum energy pathways (MEP) for these five reactions have been determined after exploring all the possible surface states of exploring all possible surface states of the highly dynamic active sites.

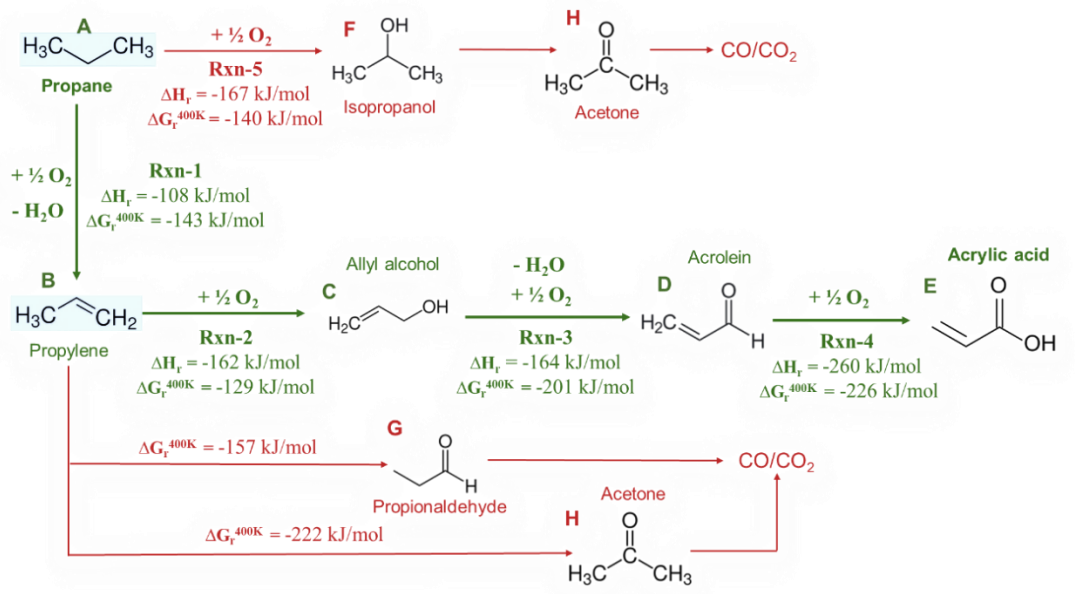

Figure 5.1. 5 Reactions theoretically studied in this work, inspired by Trunschke et al[43] Four-step partial oxidation process of propane to acrylic acid via propene, allyl alcohol and acrolein as the intermediates (Rxn-1, -2, -3 and -4 – the green path). Rxn-5 represents the partial oxidation of propane to isopropanol. Rxn-1 and -3 also produce water. Calculated enthalpies (ΔH_r) and Gibbs free energies at 400K (ΔG_r^{400K}) of reactions are given.

5.2 Thermodynamic Considerations

To initiate the analysis of the various reactions occurring during propane oxidation (see Figure 5.1) by considering the thermodynamics of the reactions in the gas-phase (thus using molecular oxygen) and the comparison to surface reactions where the oxygen adsorbed on the catalysts surface is utilized. This is performed for 3 different surface states of our catalysts having different degrees of oxidation. Each oxidation state has different possible surface configurations, and always the most stable one is chosen.

These are labeled **6a**, **5a** and **4a** in line with what we have published earlier and are shown in figure 3 along with more reduced states **3a** and **2a**[128]. Note that during 2 electron oxidation (and thus 2 electron reduction of the catalyst) the oxidation states go from **6a** →**4a**, **5a** →**3a** and **4a** →**2a**.

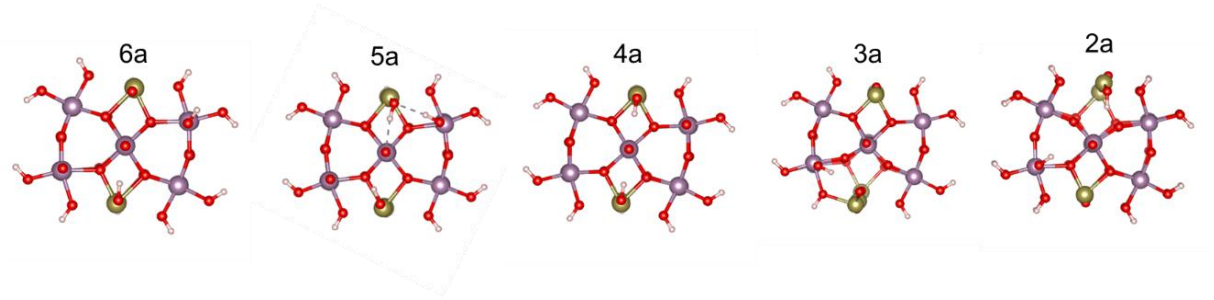

*Figure 5.2. Five most stable surfaces configurations of the M1 catalyst active site for each SOX – **6a**, **5a**, **4a**, **3a** and **2a** (all surface configurations with their IDs are also presented in table ST3 of the SI).*

Table 5.1 shows the calculated Gibbs free energies of the propane oxidation pathways shown in figure 5.1 in the gas phase using molecular oxygen as the oxidant. This is compared to the three relevant M1 surfaces (initial states **6a**, **5a** and **4a**, final states **4a**, **3a** and **2a**, see Figure 5.2). Note, that **3a** and **2a** cannot facilitate these reactions as they are in a reduced state and would need to be oxidized before reaction.

	Calculated ΔG_r^{400K} in kJ/mol							
	A→B	**A→F**	**B→H**	**B→G**	**B→C**	**C→D**	**D→E**	**Reactivity differences**
Gas phase	-143	-140	-222	-157	-129	-201	-226	-
6a -> 4a	-139	-136	-218	-153	-125	-196	-222	4
5a -> 3a	-90	-87	-169	-104	-76	-148	-173	53
4a -> 2a	-55	-52	-134	-69	-41	-113	-138	88

*Table 5.1. Calculated ΔG_r^{400K} of reactions in the gas phase and on the three most stable surface configurations **6a**, **5a**, and **4a** (ordering from more to less oxidized surface) of the cluster for propane(A)→propylene(B), propane(A)→ isopropanol(F), propylene(B)→ acetone(H), propylene(B)→propionaldehyde(G), propylene(B)→allyl-alcohol(C), allyl alcohol(C)→acrolein(D) and acrolein(D)→acrylic acid(E). The last column depicts the differences of the reaction thermodynamics due to the three different catalyst states as compared to the gas-phase.*

The surface configuration dependent reactivity difference relative to the gas phase (last column in Table 5.1) depicts that all the reactions become less favorable for more reduced conditions on the catalyst surface. Furthermore, the difference in ΔG_r of the

reactions to propylene (A→B) and to isopropanol (A→F) is only about 3 kJ/mol. This indicates that these two reactions have a similar driving force; the selectivity is therefore determined by details of the reaction pathways with the associated kinetic barriers. Formation of isopropanol drives the reaction towards the unwanted formation of acetone (H) and overoxidation to CO/CO_2. After formation of propylene (B), the oxidation to acetone (B→H) or to propionaldehyde (B→G) are both thermodynamically more favorable than oxidation to allyl alcohol (B→C), which is the crucial intermediate to the formation of desired acrylic acid (E). However, the bond dissociation energy (BDE) of the allylic C-H bond of propylene is the lowest among all three carbon atoms in the molecule (all data provided in AT5 in appendix). Hence, the allylic C-H bond should be easiest to activate, which implies that selectivity towards acrylic acid is rather driven by kinetics than by thermodynamics. The theoretical pathways for the selective path towards acrylic acid are investigated and only the formation of isopropanol as a gateway to unselective reactions is shown in detail.

5.3 Extension of the Linear Scaling Relation (LSR)

To consider all the stated five reactions on all plausible catalytic surfaces of M1 (e.g. 6a, 5a, and 4a, but also their analogues), linear scaling relations is employed in order to speed up the description of transition states. In previous work[128] also in chapter 4, a linear correlation of the C-H activation barrier of propane and of the propyl radical with the hydrogen binding energy (E_H) on the various catalytic surfaces of M1 has found. For activation at the central C2 position in propane, the linear relation reads

Equation 1: $$\Delta H_{TS} = 0.75 * E_H + 175 \text{ kJ/mol}$$

The relations for different C-H bonds in propane and in the propyl radical all showed the same slope, and the differences in their intercepts could be related to the differences in C-H bond dissociation energies (ΔE_{BDE}) according to

Equation 2: $$\Delta H_{TS} = 0.75 * E_H + 175 \text{ kJ/mol} + \Delta E_{BDE}$$

In this chapter, these considerations are extended by including propylene and allyl alcohol, which are relevant intermediates for acrylic acid formation. The calculated transition states on two catalytic surfaces (**6c** and **4g**), which represent two extreme values of E_H are performed. The four new transition states are shown in Figure 5.3.

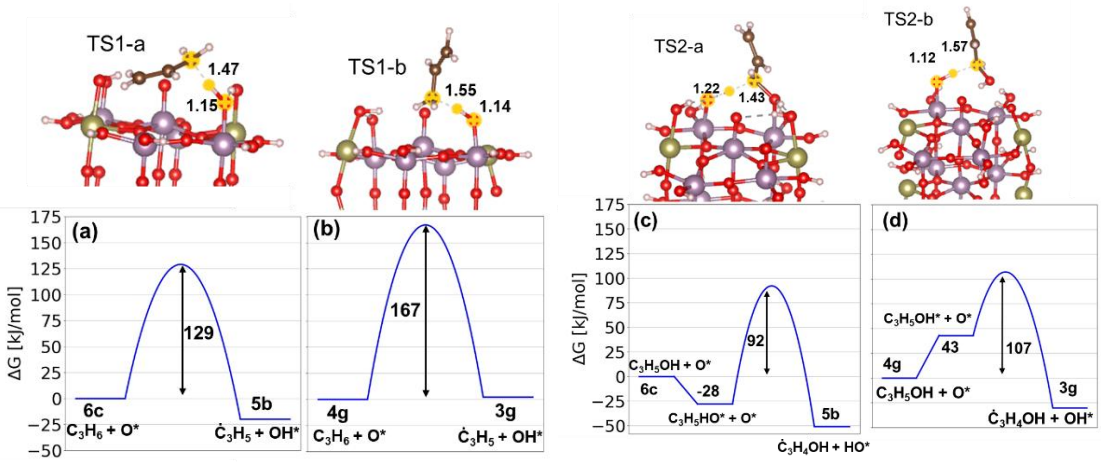

*Figure 5.3. Transition states (with C—H—O bond distances in Å) and Gibbs free energy profiles for the of H abstraction on two different active site configurations (**6c** and **4g**), for propylene at the allylic carbon position (a) **6c→5b** (135 kJ/mol), (b) **4g→3g** (173 kJ/mol), and for allyl alcohol at C1 position (c) **6c→5b** (98 kJ/mol), (d) **4g→3g** (113 kJ/mol).*

Surface type	E_H [kJ/mol]	ΔH_{TS} [kJ/mol]				
		propane C1	propane C2	propyl	Propylene CH3	Allyl Alcohol
6b	-151	89[a]	63[a]	-	60	-2
6a	-146	-	68[a]	-	-	-
4a	-106	-	88[a]	-	-	-
4g	-96	115[a]	104[a]	-	93	34
5a	15	-	-	58[a]	-	-
5b	-58	-	-	18[a]	-	-

Table 5.2. C-H activation barriers (ΔH_{TS}) for different gas molecules on various surface types with corresponding E_H ([a]reference[128]). Detailed data and figures regarding the transition states are provided in the appendix in Figures AF1 and AF2 and tables AT6 and AT7.

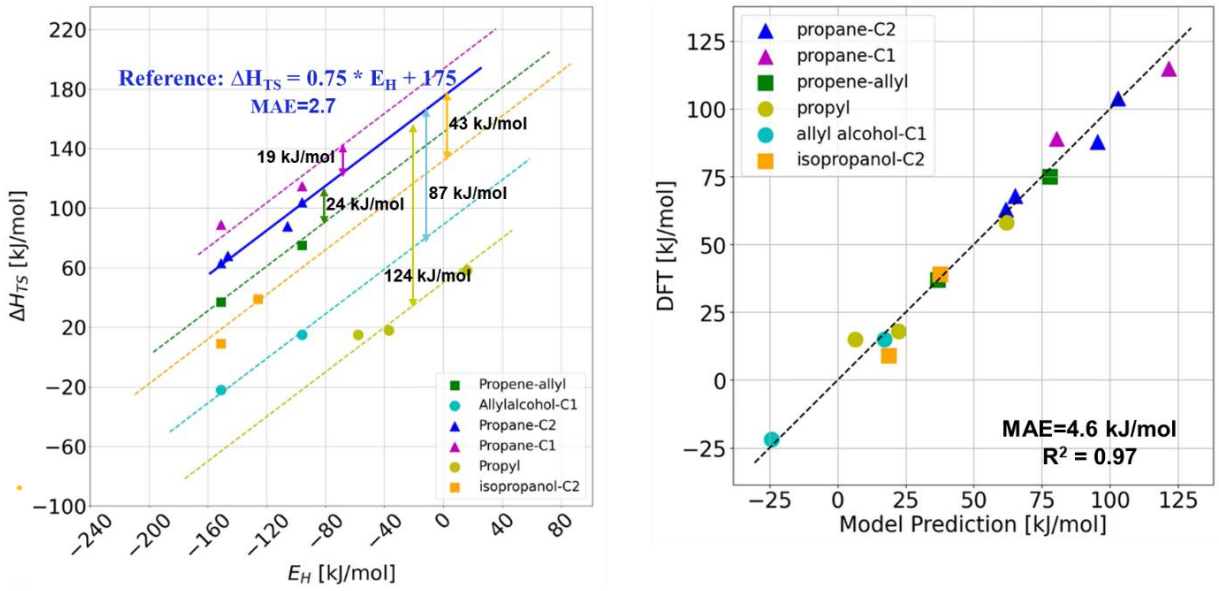

(a) (b)

*Figure 5.4 (a) Linear scaling relations for H abstraction at C1 of propane (purple line), at C2 of propane (blue line), at C1 of 2-propyl (yellow line), at allylic carbon of propene (green line) and at C1 of allyl alcohol on the **Mo-only** M1 catalyst. (b) Overall performance of our model in Equation 3 as compared to DFT calculated data, predicting most of the activation barriers with an R^2 = 0.97, MAE = 4.6 kJ/mol (the black line is the parity line).*

Gas molecule, position of H activation	**E_{BDE} (kJ/mol)**	**ΔE_{BDE} (kJ/mol)**	**E_{int}^{TS} (kJ/mol)**	**E_{MO} (kJ/mol)**	**E_{tot} (kJ/mol)**
Propane C2	431	0	0	0	**0**
Propane C1	450	+19[a]	0	0	**+19**
Propylene, allylic position	386	-45	21	0	**-24**
Allyl Alcohol, allylic position (C1)	344	-87	21	-21	**-87**
2-propene-1-ol-1-yl, O-H	191	-240	21	-21	**-240**
Acrolein C1	403	-28	21	-21	**-28**
Isopropanol C2	409	-22	0	-21	**-43**

Table 5.3. Calculated E_{BDE}, E_{int}^{TS} and E_{MO} for 6 different relevant gas molecules used in this work. $E_{tot} = E_{BDE} + E_{TS} + E_{MO}$. [a]reference[128]

Figure 5.4a shows the dependence of the calculated activation enthalpies on the H binding energies (E_H). This again obeys a linear correlation with the same slope as before. In order to describe the intercepts, the model Equation is further extended to

Equation 3: $$\Delta H_{TS} = 0.75 * E_H + 175\ \text{kJ/mol} + \Delta E_{BDE} + \Delta E_{int}^{TS} + E_{MO}$$

where ΔE_{int}^{TS} is a correction for the change relative to propane of the diradical interaction energy between the incipiently formed organic radical and the catalyst surface in the transition state[32] (mainly caused by radical delocalization), and E_{MO} is an additional stabilizing energy contribution coming from the interaction of an O-containing functional group in the reacting molecule with the catalyst surface (e.g. via hydrogen bonding).

The barriers for C-H activation at the allylic position in propylene (green line in Figure. 5.4a) appear to be about 24 kJ/mol lower than for the C2 position in propane (blue line). According to Equation 3, even lower barriers would be expected because the BDE of propylene is 45 kJ/mol lower than the BDE of propane. Spin delocalization leads to a stabilization of the allyl radical and therefore lower BDE but also leads to a less favorable interaction of the emerging allyl radical and the catalyst surface in the transition state. This leads to a correction ΔE_{int}^{TS} = 21 kJ/mol (25 kJ/mol in reference[32]) if allyl-type radicals are formed (e.g. also for allyl alcohol and acrolein) instead of non-delocalized sigma-type radicals.

Furthermore, for reactant molecules containing O atoms in carbonyl or hydroxyl groups, another stabilizing interaction with the surface needs to be considered. In the transition state structures in Figures 5.3c and 5.3d, this is observed that allyl alcohol comes significantly close to a neighboring metal site via its oxygen. To elaborate this further, the adsorption of allyl alcohol on different cluster surfaces has been studied (Figure 5.5). For all cases, the optimized geometry shows that the molecule adsorbs on the Mo atom site via the oxygen atom (metal-oxo bond distance ranging from 2.1 – 2.5 Å) and – if applicable - has a weak H-bond interaction with a neighboring Te-OH site. Based on the results for isopropanol and allyl alcohol, energy contribution of this interaction term as E_{MO} = -21 kJ/mol is determined (see Table 3). With these energy contributions included in Equation 3, thus achieved a linear scaling relation which well describes the activation barriers across various relevant species in the oxidation

reaction towards acrylic acid. The average entropic correction of 92 kJ/mol is calculated from entropies of the four transition states shown in Figure 5.3 (see Figure AF2 and Table AT7 in appendix).

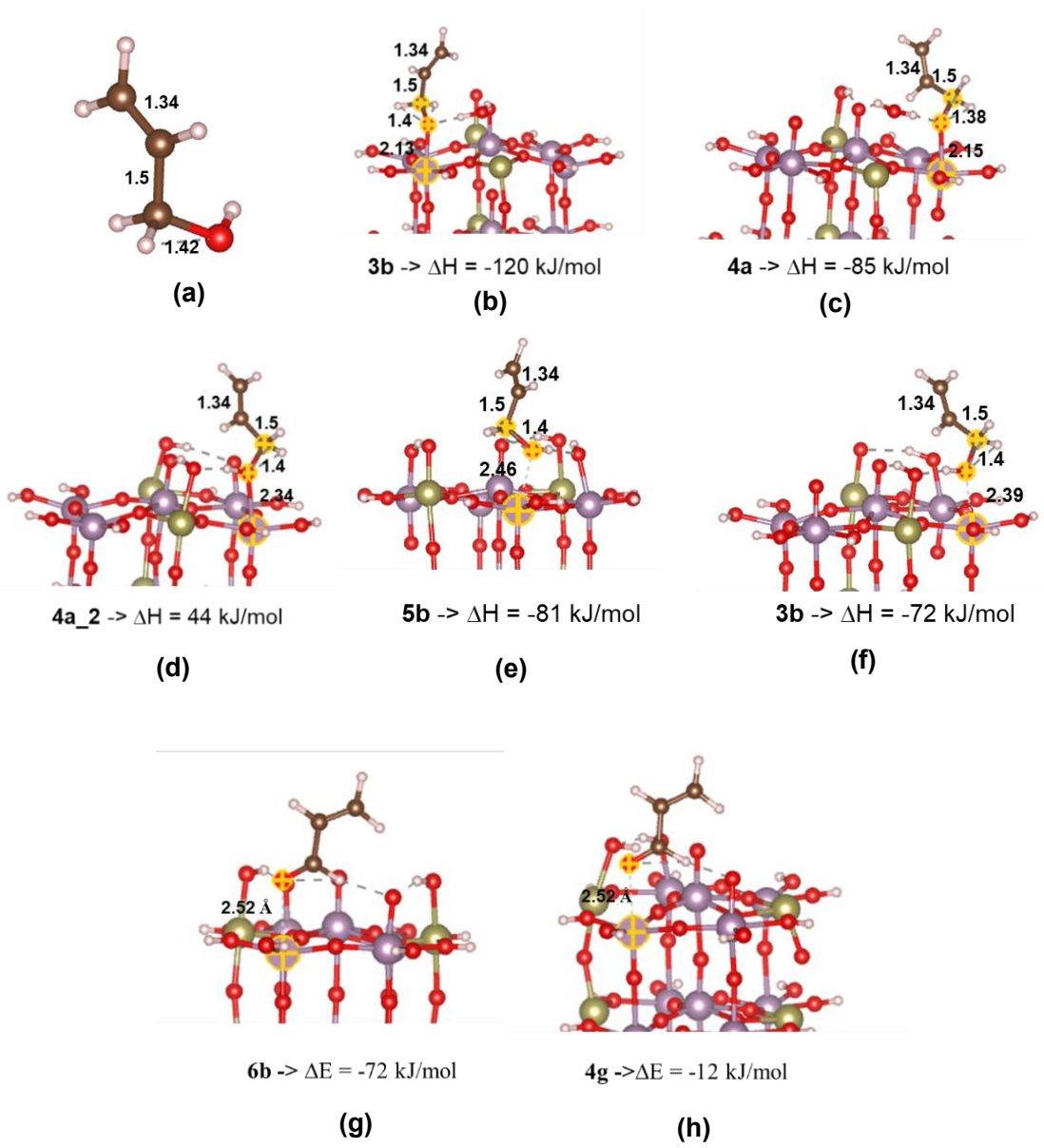

Figure 5.5. (a) Allyl alcohol and its bond distances in gas phase. (b)-(f) Adsorption of allyl alcohol via -OH group on Mo site of different cluster surfaces, (g)-(h) adsorption of acrolein via its O on Mo site. Important bond distances (in black) and corresponding adsorption enthalpies (under each picture) with surface ids are also presented.

5.4 Formation of alcohol species via fast H-migration

The Mo_5Te_2 surface cluster has one central M_o (denoted M_c), four symmetry equivalent side-Mo (denoted M_s, see Figure 2), and two Te attached to the oxygen atoms bridging M_c and M_s. After C-H activation of propane, the C-H activation of the propyl radical is an important step towards selectivity of propylene. In chapter 4, it was shown that C-H activation of a propyl radical from the gas phase primarily shows an entropic barrier which is approximated to 73 kJ/mol at 400K. Because of its radical nature, strong stabilization on M-oxo sites is possible. Calculation results for the adsorption energy of a propyl radical at C2 position are presented in Table 5.4. For adsorption on Te=O, the Te-O bond distance increases by more than 0.3Å, which is larger compared to adsorption on Mo=O (< 0.3Å). The final Te-O bond length is 2.24 Å on average, whereas for Mo-O it is 2.00 Å. This indicates a significant weakening of the metal-oxo bond at the Te site which increases the probability of oxygen cleavage from Te to produce oxygenated compounds. Similar Te-O bond distance increments are also found for allyl-type radicals of propylene (propene-3-yl) and allyl alcohol (2-propene-1-ol-1-yl).

Surface	Molecule	Metal	d_{M-O} (intial) (Å)	d_{M-O} (final) (Å)	Difference (Å)	d_{C-O} (Å)	Adsorption Energy ΔH (kJ/mol)
5c	Propyl	Te	1.85	**2.17**	**0.32**	1.39	-316
3d	Propyl	Te	1.90	**2.28**	**0.38**	1.39	-238
5b	Propyl	Te	1.88	**2.24**	**0.36**	1.39	-245
5b	2-propene-1-ol-1-yl	Te	1.88	**2.28**	**0.38**	1.36	-147
5a	Propyl	Mo	1.72	**1.96**	**0.24**	1.40	-254
4g	Propyl	Mo	1.72	**2.00**	**0.28**	1.38	-302
4a	Propyl	Mo	1.71	**2.00**	**0.29**	1.38	-204
5a	Propene-3-yl	Mo	1.71	**2.02**	**0.31**	1.38	-315

Table 5.4: Adsorption of radical species on Mo-oxo and Te-oxo sites. Changes in metal-oxygen bond distances, final C-O bond lengths and enthalpies of adsorption are given for three different radicals on various surface configurations.

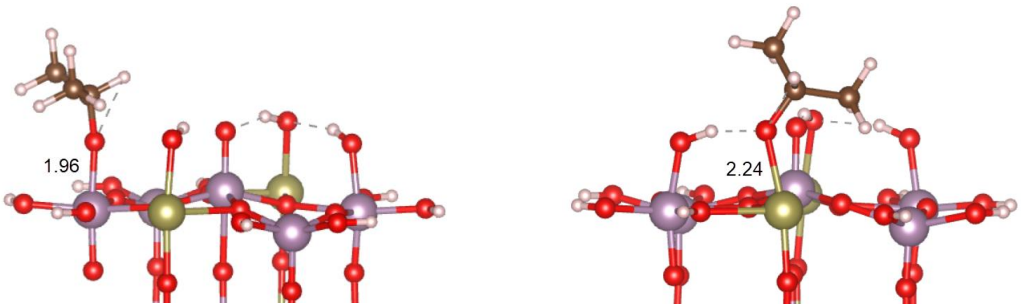

(a) (b)

Figure 5.6. (a) Propyl adsorbed at Mo-Oxo site. No hydrogen bond appears between the Mo-oxo and neighboring Te-OH site. (b) Propyl adsorbed at Te-Oxo site. Weak H-bonding interaction exists between Te-O site and neighboring Mo-OH site. This facilitates fast H-migration and formation of isopropanol from Te-O site.

Final geometry of propyl radical adsorption at Te and at Mo site are shown in Figure 5.6a and 5.6b correspondingly. A neighboring M-OH group is present in both cases. Hydrogen at Mo-OH makes a H-Bond with Oxygen at Te site after in Figure 5.6a, whereas hydrogen at Te-OH does not interact with the oxygen at Mo site in Figure 5.6 b after propyl adsorption. This implies that oxygen insertion occurs preferably from Te site than Mo site.

As an example, one of the possible pathways to form isopropanol from a propyl radical on the most stable surface configuration is calculated (Figure 5.7). Initially, the propyl radical gets absorbed at the Te=O site of **5b** with a strongly exergonic adsorption free energy of -160 kJ/mol. This adsorption weakens the Te-O bond as described in Table 5.4. Afterwards, due to a low activation barrier of 20 kJ/mol, H-migration from a neighboring Mo-OH site to Te-O-iPr facilitates the desorption of isopropanol to the gas phase and creates the surface **4g**. This low barrier of H-migration makes the formation of isopropanol highly favorable compared to the formation of propylene. This can extend the understanding to the formation of allyl alcohol from propylene and the formation of acrylic acid from acrolein following a similar mechanism. In the case of isopropanol, this mechanism steers the reaction to an unselective pathway in propane oxidation, because isopropanol can easily be further oxidized to acetone and ultimately to CO/CO2. In contrast, this kind of mechanism leads to a selective pathway towards acrylic acid in the oxidation of propylene. We have now utilized C-H activation and the above mechanism to derive the MEP for our desired reactions towards acrylic acid in the next section.

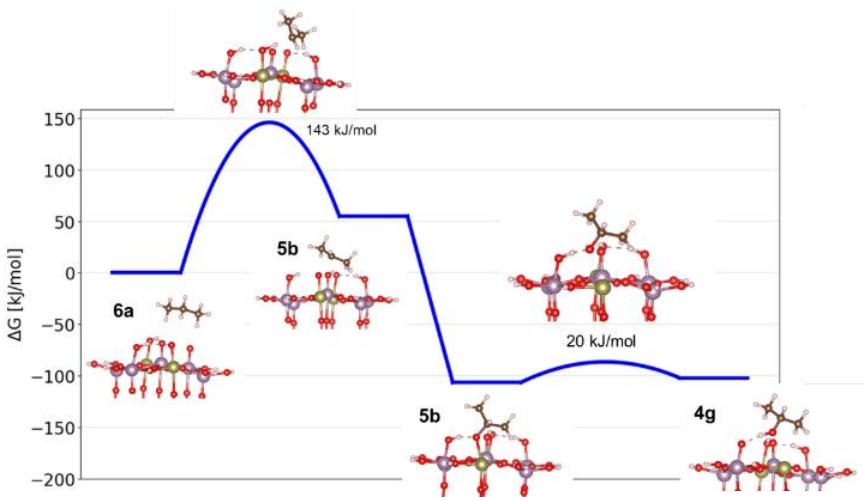

*Figure 5.7. Propyl adsorption on **5b**, followed by neighboring H-migration from Mo-OH site with a barrier of 20 kJ/mol, this desorbs isopropanol in gas phase create surface **4g**.*

5.5 Minimum Energy Pathways for propane to acrylic acid and isopropanol

According to the discussion above, the propyl radical strongly adsorbs onto the catalyst surface when a metal-oxo site of either molybdenum (Mo) or tellurium (Te) is present. Once adsorbed, fast migration of hydrogen atoms from neighboring metal-OH sites leads to isopropanol formation. In chapter 4, we demonstrated that the energy barrier for hydrogen migration between a metal-OH and a metal-oxo site is only 20 kJ/mol. The recent calculations confirm that this low barrier also applies to hydrogen transfer from a neighboring metal-OH site to the oxygen atom where the propyl radical is adsorbed (figure 5.8b). This process leads to the immediate formation of isopropanol, as illustrated in Figure S11 of the SI. The adsorption geometry of the propyl radical (shown in Figure S12 of the SI) suggests that -OH group insertion is more favorable when the radical is adsorbed at a Te-oxo site compared to a Mo-oxo site. Based on these observations, we propose a second reaction pathway for the formation of oxygenated species. This pathway depends on the presence of a neighboring Mo/Te–OH site adjacent to the Mo/Te-oxo site where the radical is adsorbed.

On the other hand, in absence of metal-oxo sites on the active site for radical adsorption, the activated radical molecule abstracts another hydrogen to a metal-OH site forming an unsaturated C3 hydrocarbon and a water molecule. As we have seen previously, the CH abstraction from activated radical species (propyl in this case) is mostly barrierless[128], this reaction occurs instantaneously. In the following section, we

describe two reaction pathways that were used to determine the minimum energy pathways for the five reactions presented in Figure 5.1.

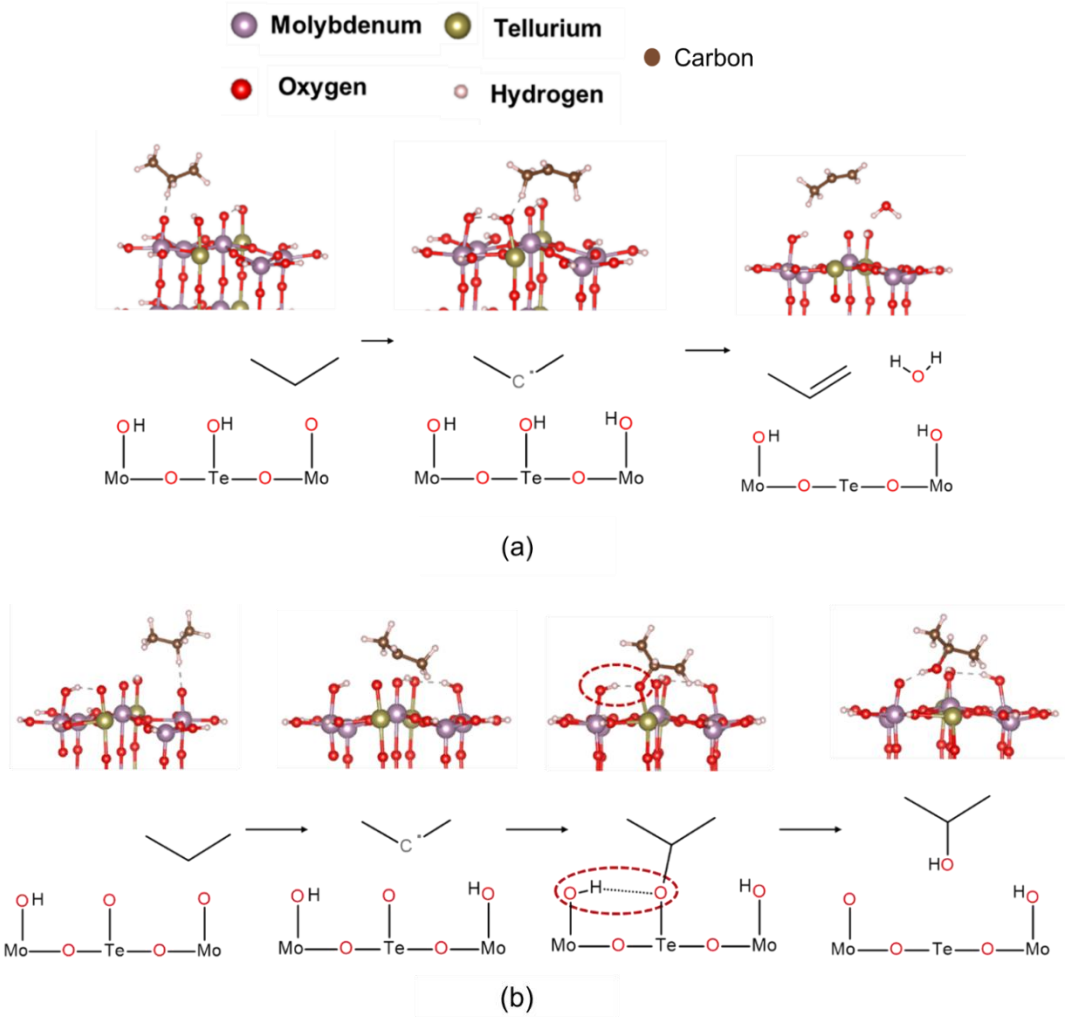

Figure 5.8. Two different reaction pathways are shown here. (a) Schematic description of the creation of a C=C double bond by two successive C-H bond activations of the two carbons of propane at two neighboring metal-oxo and metal-OH sites. The radical is not adsorbed on the surface as there are no metal-oxo sites left, rather it abstracts at another metal-OH site to create the alkene and a water molecule. In this case the conversion of propane to propylene and water is shown as an example. (b) Schematic representation of the generation of a -OH group via a 3-step mechanism - first C-H activation, second radical adsorption on M=O and finally a fast H-migration from a neighboring M-OH to form and desorb the gas species. In this case conversion of propane to isopropanol is shown.

Figure 5.8a shows two consecutive H abstractions from the saturated C3 hydrocarbon at two different M-oxo and M-OH sites forming an unsaturated C3 molecule. Both activation barriers are estimated from the linear model of Equation 3. This describes Rxn-1 (propane to propylene) and Rxn-3 (allyl alcohol to acrolein). Figure 5.8b represents a 3-step process. First the C-H abstraction occurs at a M-oxo site, followed

by adsorption of the radical species on a M-oxo site, and finally a H transfer from a neighboring M-OH site to the adsorbed fragment, forming isopropanol. The first C-H activation barrier is estimated from the linear model of Equation 3, and the second barrier (H transfer) is assumed to be 20 kJ/mol as estimated in the previous section. This pathway describes Rxn-2 (propylene to allyl alcohol), Rxn-4 (acrolein to acrylic acid) and Rxn-5 (propane to isopropanol).

The model of linear scaling relation in Equation 3 is used to estimate the activation barriers for all H abstraction steps in scheme 1 and 2. Since all these oxidation reactions are 2-electron processes, the possible starting and ending SOX of the surfaces are 6 to 4, 5 to 3 and 4 to 2. Consideration of all possible pathways for all surface configurations are shown as dotted lines in Figures 5.9, whereas the bold green and red lines represent selective and unselective MEPs, respectively, at 400K.

The free energy barriers for the first C-H activation of propane on the surfaces **6a**, **5a** and **4a** are 142 kJ/mol, 215 kJ/mol and 166 kJ/mol respectively, whereas the activation barrier to form propylene from propyl on the surfaces **5a**, **4a** and **3g** are 115 kJ/mol, 76 kJ/mol and 163 kJ/mol, respectively (Figure 5.9a, b and c). The surface **6a** first isomerizes to **6d** and the propane is then activated on **6d**, rather than activating propane directly on **6a**.

The free energies of activation for allylic C-H bond abstraction in propylene in Rxn-2 on the surfaces **6a**, **5a** and **4a** are 134 kJ/mol, 200 kJ/mol and 173 kJ/mol, respectively (Figure 5.9d, e and f). Following Scheme-2, the activated allyl radical is adsorbed in a highly exothermic step on the surfaces **5a** (-113 kJ/mol) and **4a** (-117 kJ/mol). Subsequently, fast H-migration with a low barrier of 20 kJ/mol creates and desorbs allyl alcohol from the surface, forming the surface states of **4a** and **3a**, respectively (Figure 5.9d, e). Although adsorption of the allyl radical can take place on surface **3a** (less exothermally with -60 kJ/mol), due to the absence of neighboring M-OH sites, the formation of allyl alcohol does not occur, as shown in Figure 5.8f. This situation causes the radical to remain adsorbed on the surface, blocking the active sites for other reactions to proceed from **3a**.

The free energies of activation for H abstraction from the C1 carbon in allyl alcohol in Rxn-3 on the surfaces **6a**, **5a** and **4a** are 61 kJ/mol, 153 kJ/mol and 113 kJ/mol, respectively (Figure 5.9 g, h and i).

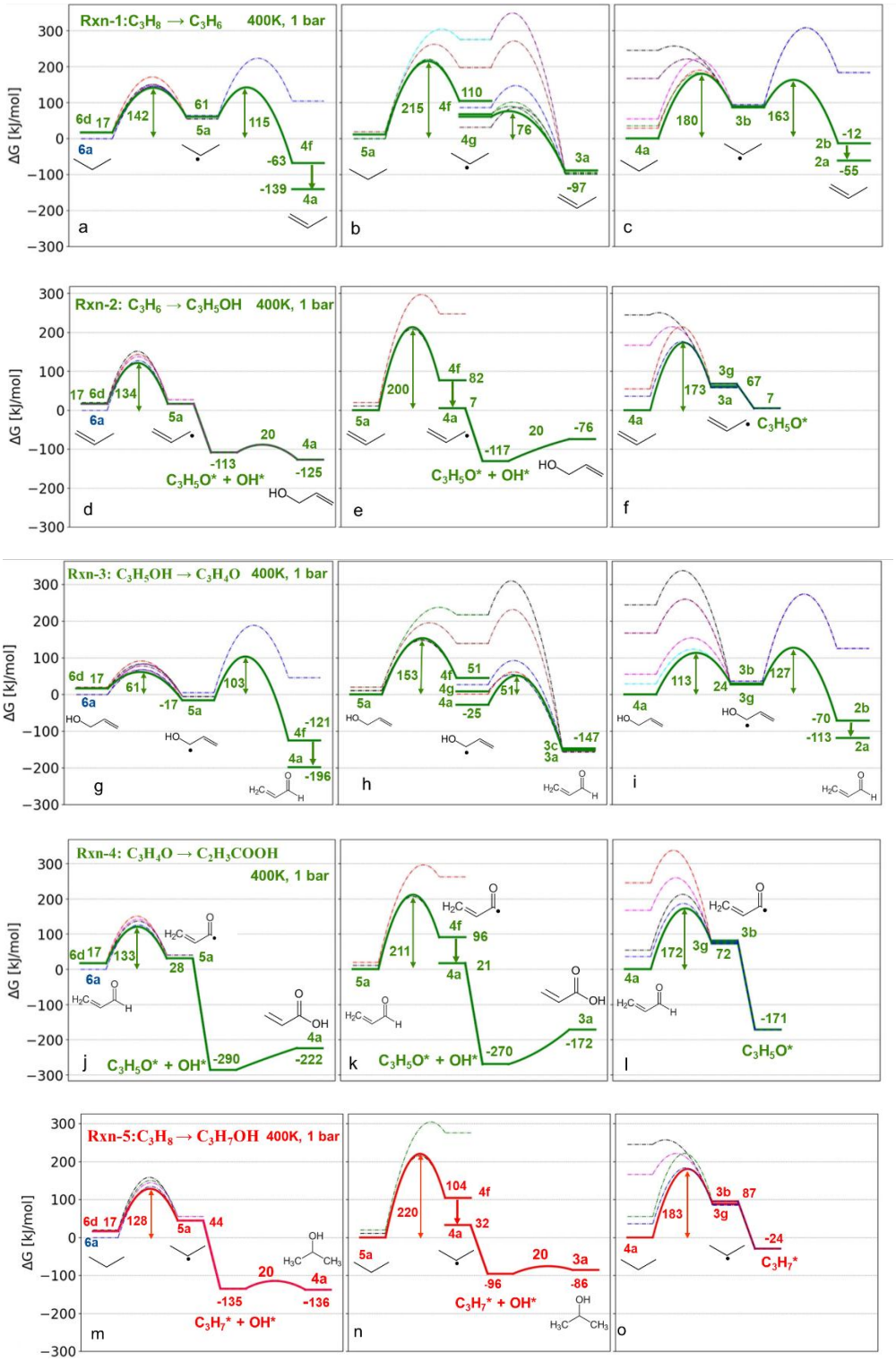

*Figure 5.9. All calculated pathways; a, b, c: Rxn-1; d, e, f: Rxn-2; g, h, i: Rxn-3, j,k,l: Rxn-4 and m,n,o: Rxn-5 are shown for the surfaces **6a→4a**, **5a→3a**, **4a→2a** at 400K, 1 bar. The green bold lines for the first four reactions in the selective path and the red bold lines for the unselective path of Rxn-5 represent the MEP and dash-dotted lines represent other possible non-favorable paths. All CH-activation barriers are estimated from the linear model of Equation 3, and the H-migration barrier is kept constant at 20 kJ/mol.*

The yellow line in Figure 5.4a for propyl radical fits the DFT calculated activation energies. The difference between its gas phase BDE to the propane line is exactly 2 times the difference between the yellow line to the propane line (blue line in Figure 5.4a). The BDE for H atom in -OH group of the allyl alcohol radical (2-propene-1-ol-1-yl) is 191 kJ/mol, which is 240 kJ/mol less than that of propane central carbon. Following the same analogy applied for the propyl radical, the activation of 2-propene-1-ol-1-yl radical is also lower only by half of its gas phase BDE, i.e., 120 kJ/mol, when compared to the central CH bond of propane (the blue line in Figure 5.4a). This gives the activation barriers on the surfaces **5a**, **4a** and **3g** to 103 kJ/mol, 51 kJ/mol and 127 kJ/mol, respectively (Figure 7g, h and i).

The pathways for formation of acrylic acid from acrolein in Rxn-4 are also presented in Figures 5.9 j, k and l. The activation free energies at the C1 carbon in acrolein on the surfaces **6a**, **5a** and **4a** are 133 kJ/mol, 211 kJ/mol and 172 kJ/mol respectively. Activated radical species are strongly adsorbed on a M-oxo site of **5a** and **4a** with -290 kJ/mol and -270 kJ/mol, respectively. Again, a fast H-migration from a neighboring M-OH site with 20 kJ/mol barrier creates the -OH group and facilitates the desorption of acrylic acid from the surface. Comparatively lower adsorption energy of -171 kJ/mol for the radical species of activated acrolein (2-propenal-1-yl) on 3a is observed. But this adsorbed species can block the surface sites, since the lack of neighboring M-OH site does not lead the reaction towards acrylic acid via the insertion of -OH.

The formation of isopropanol from propane in Rxn-5 is an unselective side path in the production of acrylic acid. The first C-H activation barriers are equal to the barriers for Rxn-1 (Figure 5.9 m, n and o). The propyl radical is adsorbed at the surfaces **5a** and **4a** with -121 kJ/mol and -82 kJ/mol, respectively. Consecutive H migration creates and desorb isopropanol leaving the surface at states **4a** and **3a**, respectively. This reaction is competing with the formation of propylene via C-H abstraction of propyl from gas phase which is barrierless (in energy) in most cases. Hence selectivity towards propylene should depend on three factors, i.e. on the availability of a M=O adsorption site for propyl, the adsorption strength of propyl and the availability of neighboring M-OH sites. Whereas these three factors can drive the reaction towards unselective pathways to isopropanol, the same three factors can increase the probability of -OH group formation and the formation of allyl alcohol and acrylic acid in the oxidation of

propylene and acrolein, respectively. All activation barriers of the MEPs are tabulated in Table 5.5.

Reactions (mechanism)	Starting → End surfaces	ΔG_1^{TS} (kJ/mol)	ΔG_2^{TS} (kJ/mol)
Rxn-1:$C_3H_8 \rightarrow C_3H_6$	6a → 4a	142	115
	5a → 3a	215	76
	4a → 2a	180	163
Rxn-2: $C_3H_6 \rightarrow C_3H_5OH$	6a → 4a	134	20
	5a → 3a	200	20
	4a → 2a	173	-
Rxn-3:$C_3H_5OH \rightarrow C_3H_4O$	6a → 4a	61	103
	5a → 3a	153	51
	4a → 2a	113	127
Rxn-4: $C_3H_4O \rightarrow C_2H_3COOH$	6a → 4a	133	20
	5a → 3a	211	20
	4a → 2a	172	-
Rxn-5:$C_3H_8 \rightarrow C_3H_7OH$	6a → 4a	142	20
	5a → 3a	207	20
	4a → 2a	166	-

Table 5.5. Free energy of activation ΔG_1^{TS} and ΔG_2^{TS} for the five reactions studied on three different starting surfaces.

The surfaces **6a** and **4a** isomerize to **6d** and **4g** respectively and activate the C-H bond with lower activation barrier in all the five reactions shown above in Figure 5.8. For all cases shown, the C-H activation barrier on **5a** is always the highest among the three starting surfaces. The surface **5a** has three M-OH sites and only one M=O site. Hence, this indicates that high -OH coverage on the active site leads to high C-H activation barriers. On the other hand, the MEPs show that, Scheme-1 for Rxn-3 can occur on all the three starting surfaces **6a**, **5a** and **4a**, because of having comparatively low barriers of allyl alcohol activation to produce acrolein. Whereas the same for Rxn-1 is only favorable on starting surface **6a** and **4a**. But -OH insertion in Scheme-2 for Rxn-2, Rxn-4 and Rxn-5 is favorable only at **6a**. Because the CH-activation barrier at **5a** is very

high, and -OH insertion starting from **4a** is hindered due to lack of M-OH site at **3a** for all the cases above. The mitigation to this problem is to keep the active site always at high SOX of 6 by repeated oxidation using O_2. The strong stability via deep exothermic adsorption of acrolein radical for Rxn-4 can lead to active site blocking, forming a high coverage of adsorbed acrolein radical and hindering the selectivity towards acrylic acid.

The production of allyl alcohol from propylene and especially of acrylic acid from acrolein, both following Scheme-2, appeared to be less favorable and should become the bottleneck reactions compared to the production of propylene from propane and acrolein from allyl alcohol, following Scheme-1, in the full pathway towards acrylic acid production. Production of iso-propanol is more favorable than production of propylene after propane activation. This should result in the reaction to drive towards the unselective pathway. Scheme-2 reveals a contradiction in selectivity for acrylic acid production after a certain level of propane conversion. While Scheme-2 is essential for converting propylene to acrylic acid, it reduces the selectivity for obtaining propylene from propane oxidation. As more propane is converted to propylene, the pathway from propylene to acrylic acid becomes more favorable due to lower activation barriers. This shift makes subsequent reactions (Rxn-2, Rxn-3, and Rxn-4) more competitive, complicating selectivity. Rapid hydrogen transfer at the metal site initiating Scheme-2 is a key factor limiting the industrial viability of catalyst M1 for one-stage propane oxidation to acrylic acid, highlighting the need for a better understanding of these mechanisms to improve performance.

5.6 Conclusion of the chapter

In this chapter, the extensive exploration of the phase space of catalytic surface configurations of the active site of the M1 phase of the Mo-Te-Nb-O catalyst are performed, and all the minimum energy pathways with the thermodynamics and kinetics data for five important reactions involved in production of acrylic acid from the selective oxidation of propane are presented. In order to that, a robust linear scaling model is established that can be applied to broad range of gas species for faster estimation of activation barrier. Results show that the high activation barrier for the first C-H activation on the Mo-only catalyst is the crucial rate determining step of the process and it varies largely with the oxidation state of the surface what is represented

by SOX in this work. The fast hydrogen atom migration on the surface, which also leads to a reaction scheme for oxygen insertion mechanism, is an important determining factor for better selectivity and at the same time the reason for lowering selectivity in direct propane oxidation towards acrylic acid on M1. This issue is not present in current industrial process where a two-stage conversion has been established so far to separate the propane oxidation to propylene and propylene oxidation to acrylic acid via two different selective mixed metal oxide catalysts. Hence this poses a real challenge for industrial evaluation of the one stage process of direct conversion of propane towards acrylic acid via M1 catalyst. In addition, a specific arrangement of surface M-Oxo and M-OH sites as well as surface coverage of O* and OH* species at reaction conditions are important descriptors for selectivity towards propylene as well as acrylic acid. As a next step of this research, a partial replacement of molybdenum by vanadium or other transition metals is considered to study the effect of metal substitution on catalytic performance.

6. Selective oxidation of Propane to Propylene on M1 phase in presence of Vanadium and Te-Vacancy

6.1 Introduction

So far, the cluster model only includes Mo and Te. In this chapter Mo is systematically replaced by V to create the cluster model for Mo-V-Te-Nb-O catalyst. This model is used to produce different pathways for propane oxidation to propylene on different catalytic surfaces with all possible SOX. The result has been analyzed to understand the effect of vanadium on catalytic performance. Trunschke et al[47] reported dilution of Te on the surface due to hydrolysis on wet condition and its effect on catalytic performance. The effect of the Te free active site at the top layer is also modelled and its catalytic activity for propylene formation is investigated. As described in previous chapters, the selectivity towards acrylic acid mainly depends on the selectivity of propylene formation from propane, because propane can be easily oxidized to isopropanol to create by products like acetone. Therefore, I have only focused on the propane oxidation to propylene in this chapter to conclude the work.

6.2 Replacement of Mo by V

T**he Substitution Energy (SE)** of Mo by V with all possible configurations at the top layer and the layer underneath is calculated here. The references used are $Mo(OH)_5$ and $V(OH)_5$ in gas phase. The combinatorial possibilities of Mo/V in the top layer are shown in Figure 6.1. All the SE for first and/or second layer are presented in Figure 6.2. The lowest configurations (1V_2, 2V_1, 3V_3, 4V_1) in all cases have V at the central position (M_c).

This chapter is based on the following publication in preparation:

K. Sen, A. Schäfer, and F. Studt; "Quantum Chemical Study of Selective Oxidation of Propane to Propylene on MoVTeNb M1 oxide Catalyst with Several Vanadium Content and Te-Vacancy"

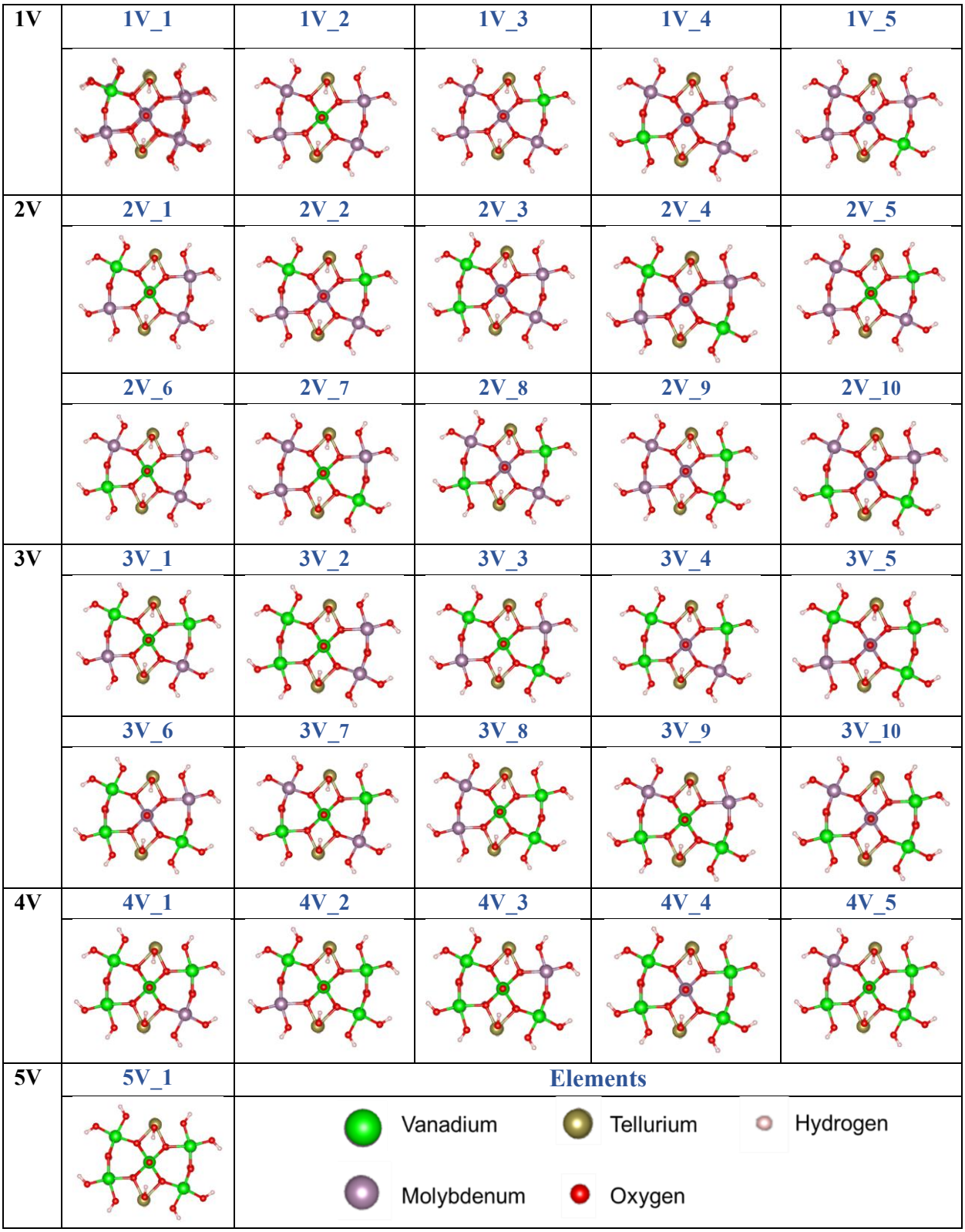

Figure 6.1. All possible configurations of the active site by replacing Mo by V on the top layer are shown here.

The configuration **1V1V** with both vanadium at central position in two layers appears to be the most stable structure. This concludes that the central position is always replaced by V first. The data for V only in 1st layer in Figure 6.2a shows that replacing up to three Mo at the top layer is thermodynamically possible, as SE becomes endothermic from four vanadium. Nevertheless, orange data points for V in both layers in Figure 6.2a shows stabilization of SE which implies the existence of vanadium in both layers, rather only on topmost layer.

Systematic increase of SE with increasing V-content in both sections of Figure 6.2a indicates that there is a limit of maximum vanadium loading possible in two layers, which should be maximum three vanadium in both layers. The structures **1V1V**, **3V0V**, **3V1V**, **3V2V** and **3V3V** are the most relevant stable configurations and are considered for further understanding of propane oxidation to propylene and the effect of vanadium in catalytic performance (Shown in Figure 6.2b).

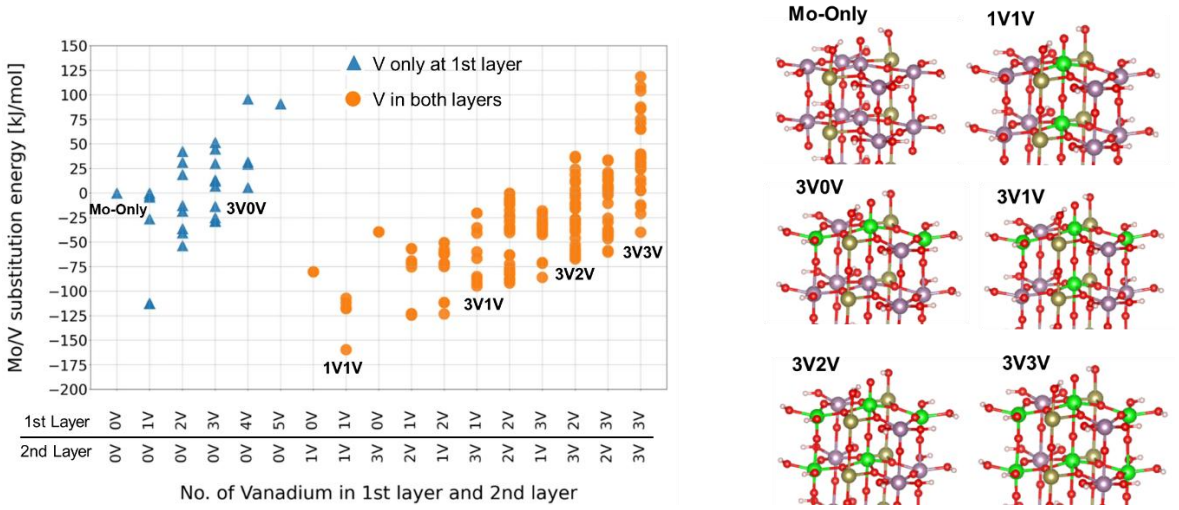

(a) (b)

*Figure 6.2. (a) ΔE of the Mo/V substitution energy (SE) by V in one and two layers are shown here. The data for V only in the top layer are shown in blue triangle markers, and the data for the substitution in two layers are shown in orange circles. $Mo(OH)_5$ and $V(OH)_5$ in gas phase are used as references. (b) All the important structures that are with minimum substitution energy and are considered for our further study are shown here. V are shown in green, Mo in purple, Te in gold, oxygen in red and hydrogen are shown in white. The names of the structures are given in a format such as **3V2V** represents the structure with 3 V in the 1st layer and 2 V in the 2nd layer as an example.*

6.3 Effects of Vanadium on Propane oxidation to propylene

Only the minimum energy pathways for the selected active sites of **Mo-only**, **1V1V**, **3V0V**, **3V1V**, **3V2V** and **3V3V** are shown in Figure 6.3. First CH activation barriers of propane are 84, 106 and 71 kJ/mol on SOX 6, 5 and 4 respectively for **3V3V** (the blue line), which are significantly lower than that on Mo-only active sites (the green line). Propane activation barriers on the starting surface with SOX 6 and 5, have systematically reduced with increment of the number of vanadium in the 2nd layer, producing the ranking for activity as **Mo-Only** < **3V1V** < **3V2V** < **3V3V**. **3V0V** has definitely lower propane activation barrier on SOX = 6 than Mo-only cluster, but this is not true anymore for reduced active sites with SOX 5 and 4. Whereas **1V1V** having both vanadium at central position in two layer always has significantly high propane activation barrier and remains inactive for the reaction. Presence of 2 or 3 V (**3V2V** and **3V3V**) at the second layer made the surface with SOX 5 and 4 also further active, whereas they are inactive for less amount of V. For the next step of propyl to propylene formation, surfaces with SOX 6 and 5 have significantly lower barriers of 16 and 15 kJ/mol with **3V3V** configuration. This barrier is lower than the fast H-Migration barrier to form isopropanol from propyl radical (20 kJ/mol) via scheme-2. This makes the catalyst highly selective towards propylene than towards isopropanol. Propyl activation barriers with **3V2V** configuration are 56, 27 and 26 kJ/mol respectively on SOX 6, 5 and 4. This low barrier makes the catalyst very competitive and selective towards propylene formation. Nevertheless, all the active sites with lower vanadium content produce less propylene formation in comparison to isopropanol formation. So higher vanadium content keeps the surface active even at reduced condition, however SOX=4 produces less propylene than others and needs to be re-oxidized to become further active towards propylene. Adsorption of propyl radical on three different surfaces of **3V3V** are shown in Figure 6.4. Propyl is adsorbed with strong exothermic energy at the Te-Oxo site. But the presence of a neighboring Mo-OH site (Figure 6.4 a, c and e) bends the oxygen atom of Te-Oxo towards it via weak H-Bond force. This movement is missing at the adsorption site shown in Figure 6.4b where there is no neighboring Mo-OH site present.

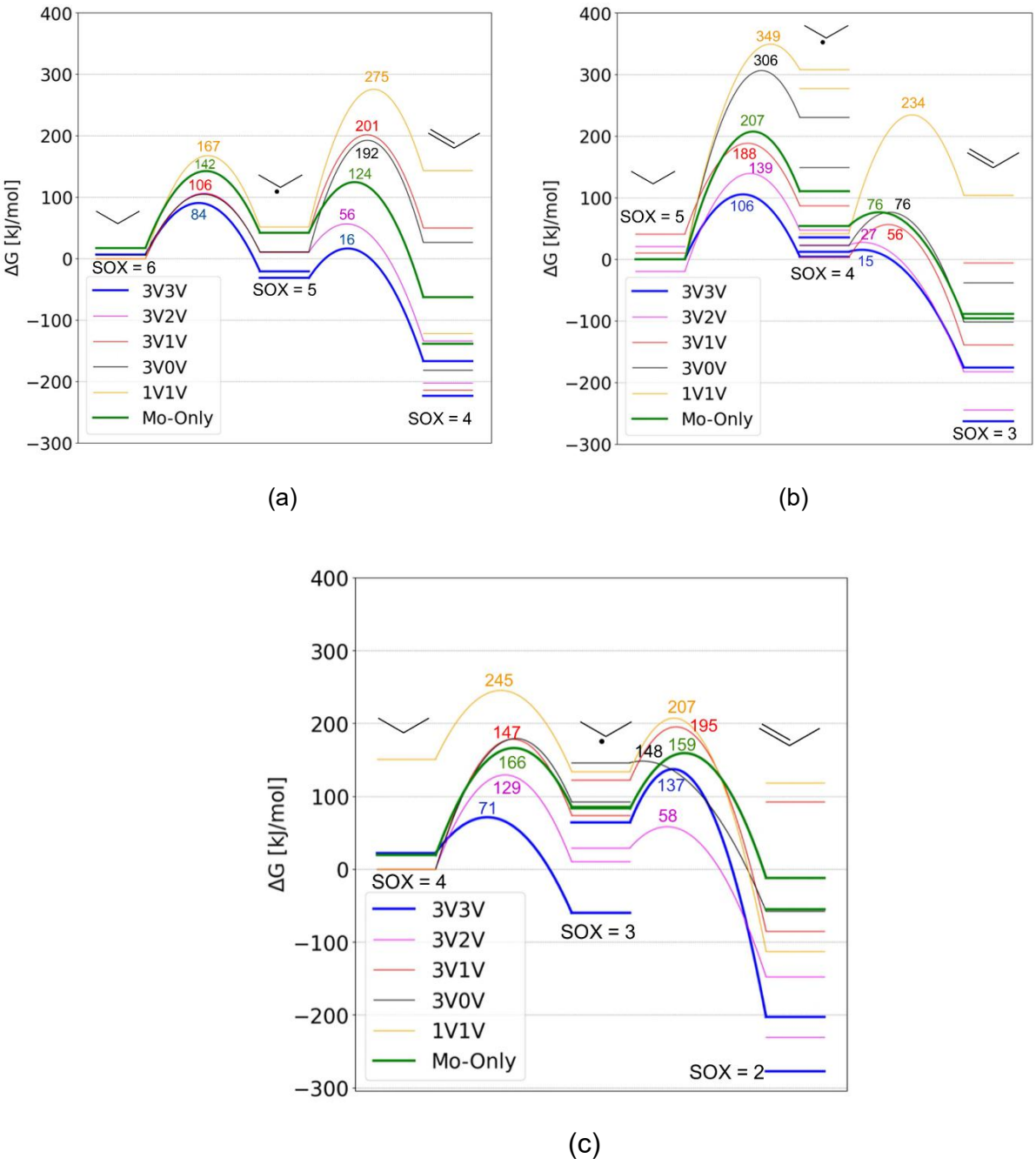

*Figure 6.3. All the minimum energy pathways (MEP) for propane oxidation to propylene on the active sites of **Mo-only**, **1V1V**, **3V0V**, **3V1V**, **3V2V** and **3V3V** clusters are generated from our database of all possible surface configurations of SOX. The transition state barriers are approximated from the LSR established in previous chapter. (a) The MEP for SOX 6 to SOX 4, (b) The MEP for SOX 5 to SOX 3 and (c) the MEP for SOX 4 to SOX 2 are presented. The complete set of raw data are provided in appendix AT2 and AT3.*

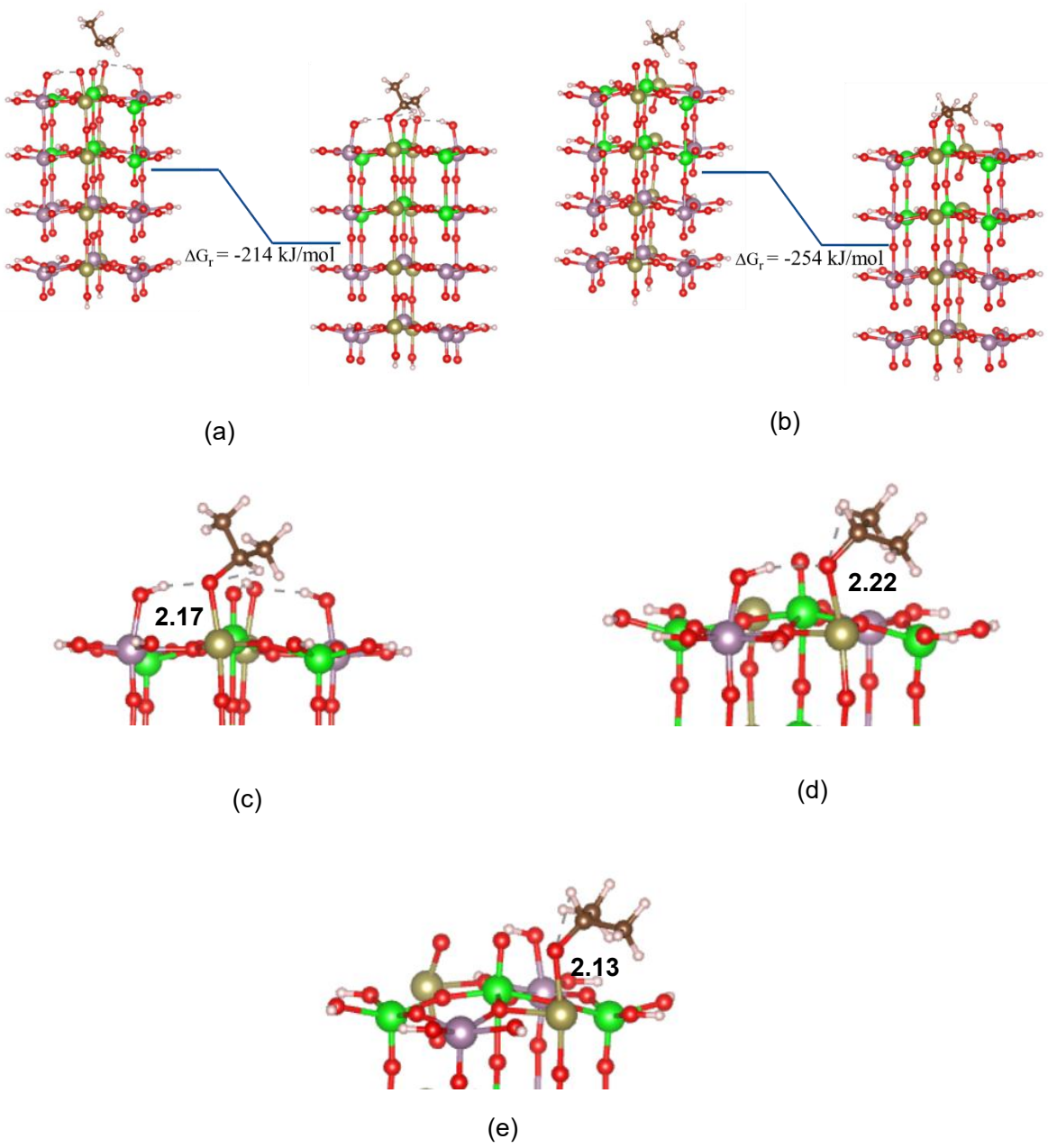

*Figure 6.4. Adsorption of propyl radical at 3 different active sites with **3V3V** configuration. The presence of neighboring Mo-OH site bends the O atom at Te-O towards it via H-bond force after propyl adsorption at (a), (c) and (d). This movement does not appear where there is not neighboring Mo-OH site in (b) and (e).*

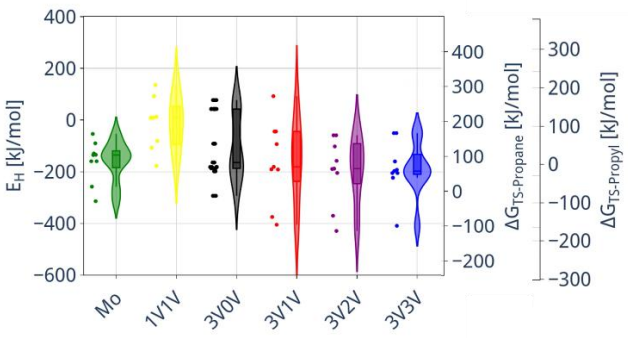

(a)

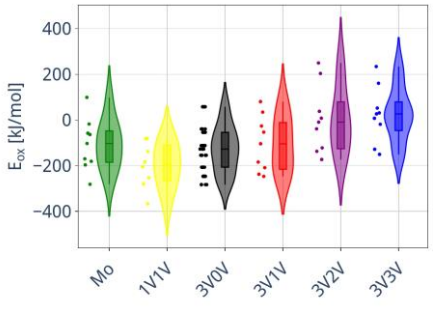

(b)

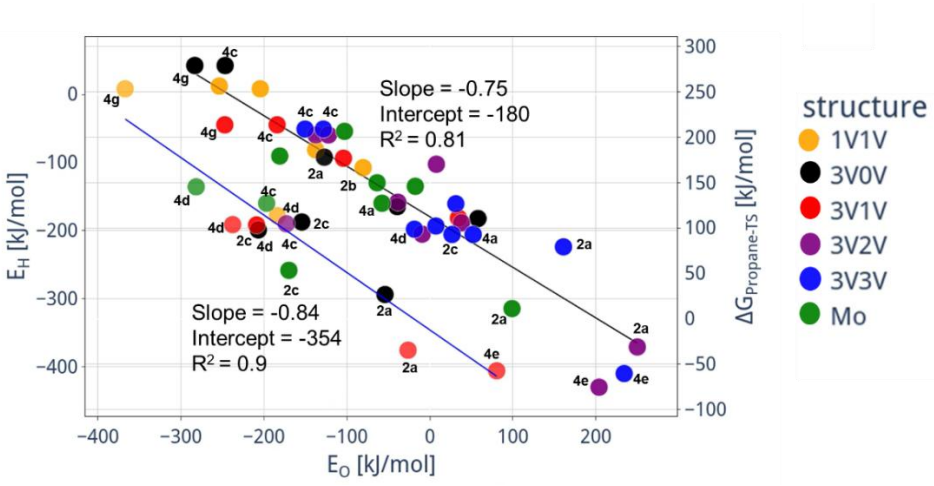

(c)

Figure 6.5. Violin plot with the data from (a) Hydrogen atom binding energy (Y-axis 1), Propane activation barriers (Y-axis 2) and Propyl activation barriers (Y-axis 3), (b) Oxygen atom binding energy, are shown here w.r.t the active sites with zero to many vanadium content in one and/or two layers. Box plots are shown in the order sorted by the median of the data to capture the trend. (c) The whole data set of E_H and E_{OX} are plotted against each other showing the existence of good correlation between the two descriptors. The blue lines are used as the guiding lines to show two negative correlations inside the data sets. All the data are provided in appendix table AT8.

Figure 6.5 a, b presents the statistical distribution of different descriptors such as hydrogen (E_H) and oxygen atom binding energies (E_O) on different active sites. Clear trend of decrement of average E_H and increment of average E_O appears w.r.t increasing vanadium content till **3V3V**, with minor exceptions. **3V3V** possesses the lowest set of E_H. For obvious reason, E_O shows the opposite trend of continuous increment w.r.t increasing vanadium content.

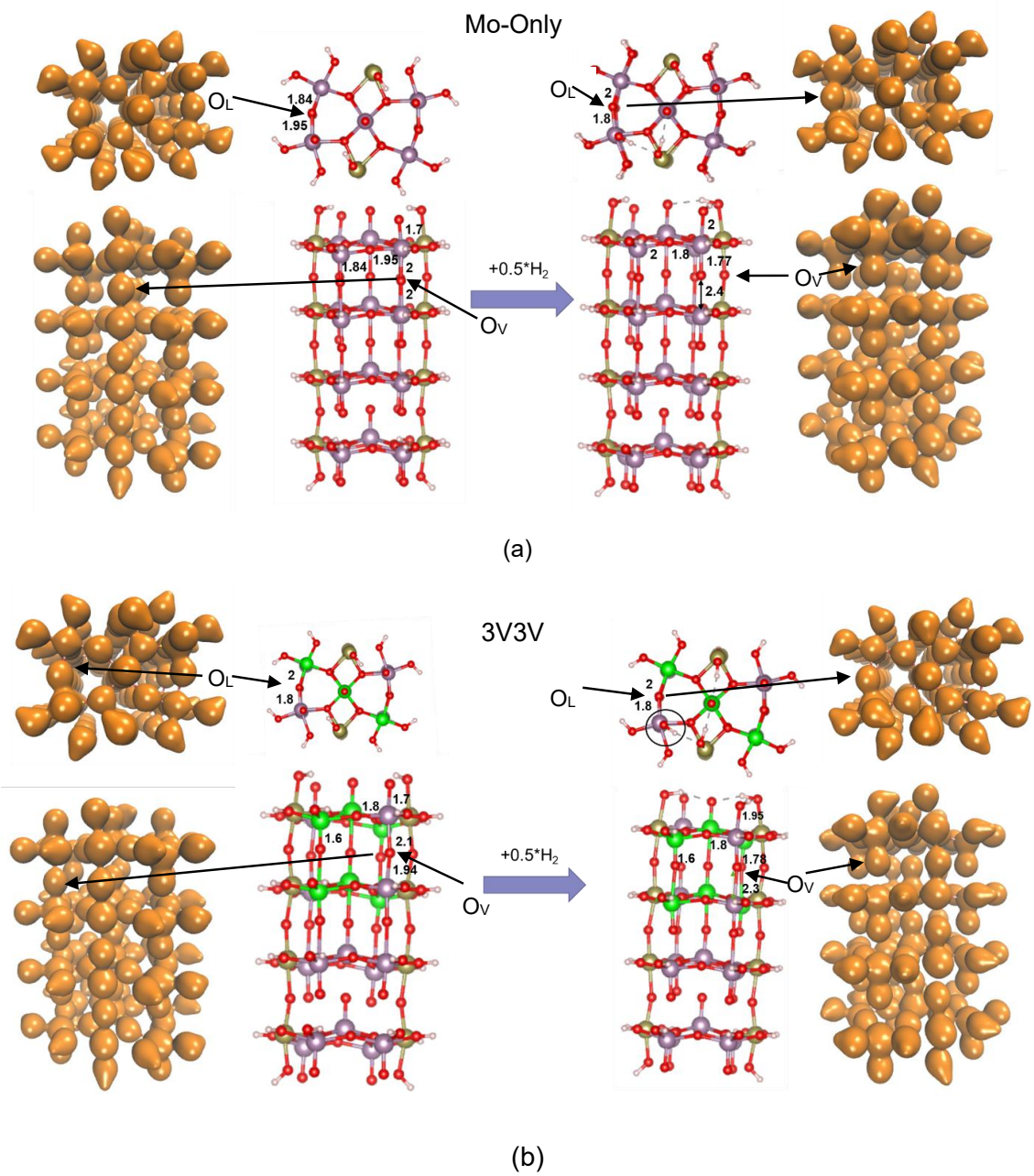

Figure 6.6. Top and side view of the geometry and the total density of the active sites (a) ***Mo-Only*** *and (b)* ***3V3V*** *are shown here before and after hydrogenation. O_L represents the lattice oxygen and O_v represents the oxygen between two Mo atoms in the first and second layer. Corresponding metal-oxygen distances are also shown for these two oxygen types.*

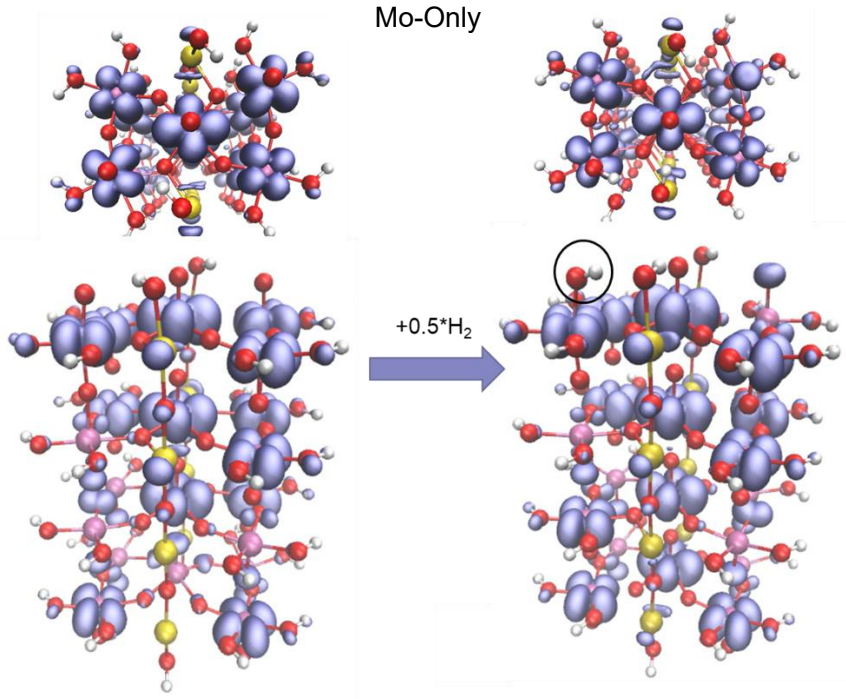

(a)

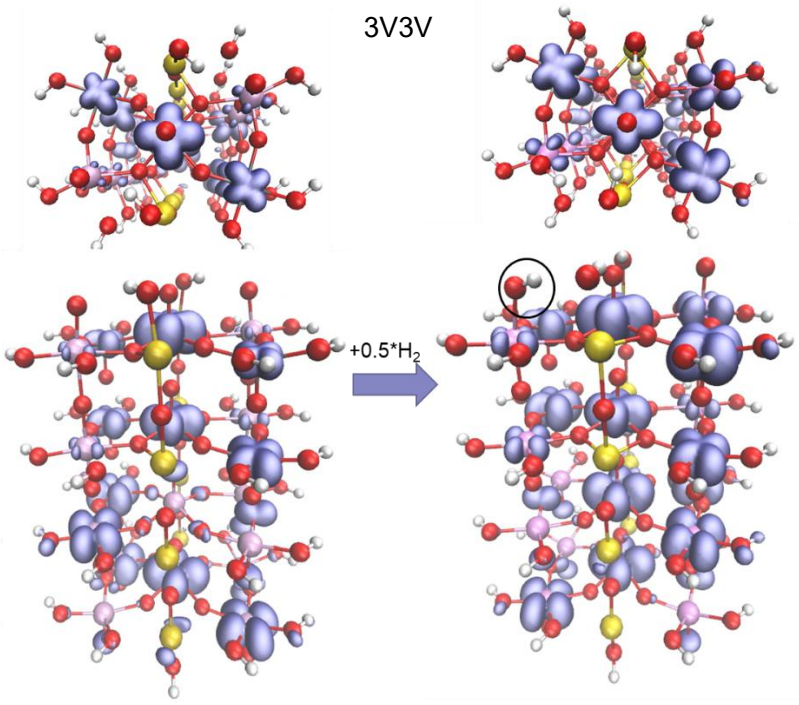

(b)

Figure 6.7. Top and side view of the spin density of the active sites (a) ***Mo-Only*** *and (b)* ***3V3V*** *configurations have been shown before and after hydrogenation. O_L represents the lattice oxygen and O_v represents the oxygen between two Mo atoms in the first and second layer. Corresponding metal-oxygen distances are also shown for these two oxygen types.*

The statistical ranking of both propane and propyl activation barriers are same as E_H, but in a different range of values as they are derived from E_H with our Linear Scaling

Relation, have been shown by introducing in the secondary y-axes in Figure 6.5-a. Major number of negative activation barriers of propyl on **3V2V** and **3V3V** are of high interest as they lead the reaction towards propylene more competitive and selective. All the data for E_O and E_H are plotted against each other in Figure 6.5c, this shows a clear negative trend for reduced E_H when E_O is increased in different surface-active sites specially with increasing number of vanadium content.

To understand what changes vanadium does, to make the Mo-O site more active, the geometry, total density before and after hydrogenation of **Mo-only** (Figure 6.6a) and **3V3V** (Figure 6.6b) surfaces are analyzed. Spin densities of the same have been shown in Figure 6.7. There are two oxygens attached to the active metal site Mo, one is O_L which is the lattice oxygen connecting other Mo or V, and the other one is O_V, which is the oxygen connecting two Mo in first and second layer. They are also indicated by arrows in Figure 6.6. Both total density and distance shown in the Figure 6.6a depict that O_L and O_V are equally shared between two Mo in **Mo-Only** surface before hydrogenation. But after reduction by a hydrogen atom, both this oxygen moved towards the active metal site Mo to oxidize it further. Whereas, in presence of V (Figure 6.3 b), O_L remains fixed, as it has already oxidized the Mo fully and not shared between the Mo and V. The O_L has only moved upwards because of hydrogenation. Hence, the two distinct migrations of O atoms in previous case cost more energy compared to the later with only one O-atom migration between two layers. The same explanation can also be concluded from spin density shown in Figure 6.7. There is always a spin density on all the 4 bridge Mo in **Mo-Only** active site, hence they are not completely oxidized. Whereas there is no spin on Mo in **3V3V** structures, rather only on V sites. This means the Mo sites are purely oxidized in presence of V in neighborhood; hence they become more active to be reduced for CH activation.

6.4 Propane oxidation on Te-Free active sites

Trunschke et al.[47] has reported that acrylic acid can also be formed on Te-free MoV oxide M1 catalyst, implying that Te is not necessarily required as an active component. Other studies have enforced the presence of Te, showing that it increases the selectivity of acrylic acid, especially for the step of propylene oxidation to acrylic acid[10]

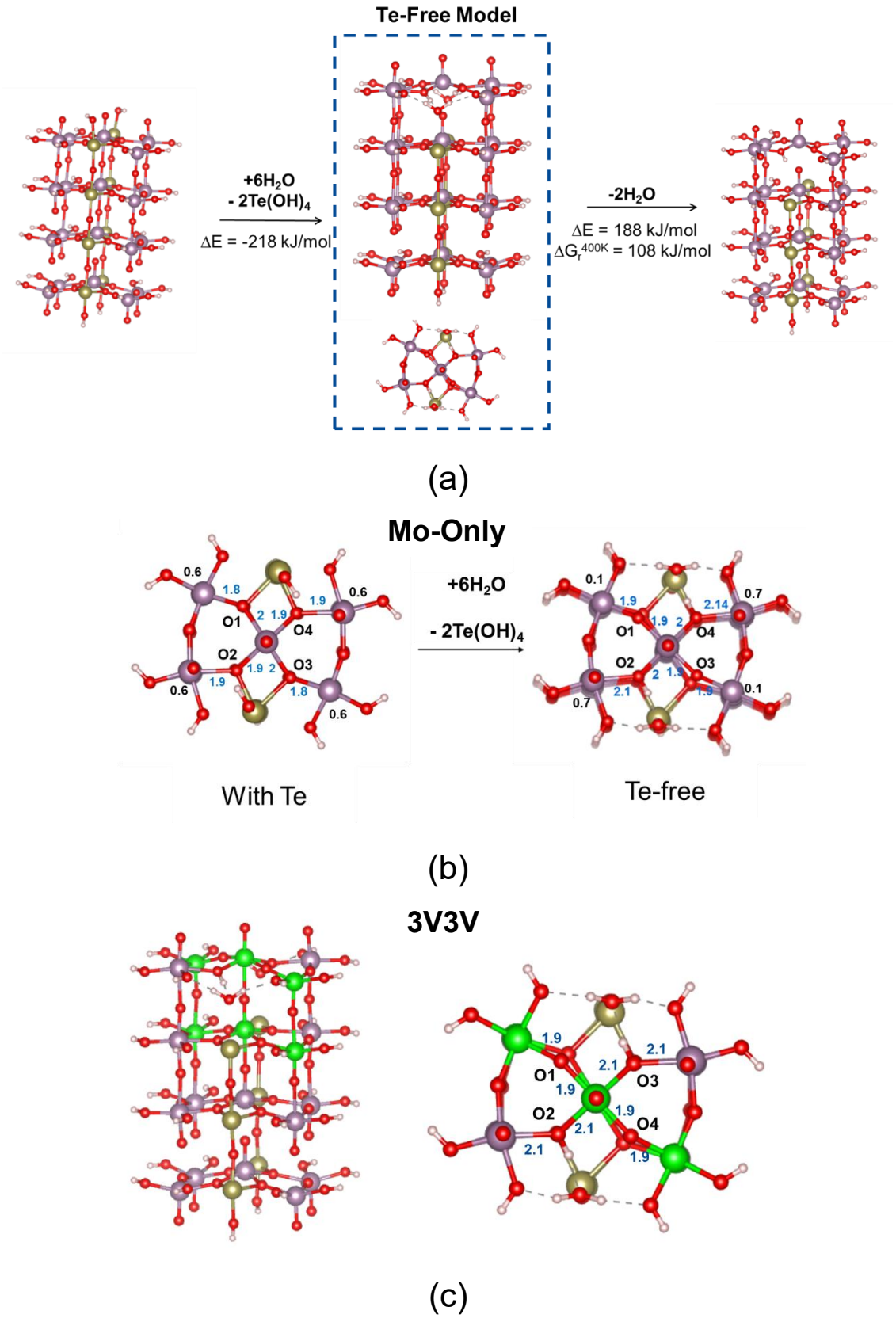

Figure 6.8. Top and side view of the spin density of the active sites (a) ***Mo-Only*** *and (b)* ***3V3V*** *configurations have been shown before and after hydrogenation. O_L represents the lattice oxygen and O_v represents the oxygen between two Mo atoms in the first and second layer. Corresponding metal-oxygen distances are also shown for these two oxygen types.*

and also an element that activate propane in presence of vanadium distribution in surrounding having a range of activation barriers 96 to 142 kJ/mol[45]. Propane can also be activated by Mo with a similar, even slightly lower range of activation barriers. In addition, the presence of Te initiates the formation of isopropanol from propyl radical by the pathway shown Figure 5.8b driving the reaction towards unselective path in formation of propylene. On the other hand, the same pathway is crucial for propylene oxidation to acrylic acid via intermediates of allyl alcohol and acrolein.

- ***Te-Free Model Development:***

Hence to put a shed in the above dilemma, a Te-Free cluster model by removing the two Te-OH from the top layer by hydrolysis is created. In Figure 6.8a, the modelled hydrolysis reaction is shown. It takes place by attacking the three oxygen atoms connected to each Te by three water molecules, which leads to the insertion of three -OH groups to Te to form a $Te(OH)_4$ compound and the other three hydrogen atoms terminate the three oxygen atoms in the cluster. Six water molecules are required in total to dissolve two Te sites forming two $Te(OH)_4$ compounds from the top layer. After geometry optimization, the final structure of the active site contains two water molecules physi-adsorbed on the Te sites at the second layer and two hydrogen atoms terminate the lattice oxygens connecting the central Mo and Mo-Oxo in diagonal position. This modelled reaction is exotherm by ΔE of -218 kJ/mol. Bond distance analysis tells that the lattice oxygens O1, O2, O3 and O4 are equally shared between the central Mo and bridge Mo or V in both **Mo-only** (Figure 6.8b) and **3V3V** (Figure 6.8 c). To satisfy the expected valency of Mo, O2 and O4 are terminated by the hydrogen atom, because they are connected to the bridge Mo which has an oxygen at the top sites.

In Figure 6.9a, it is shown that 3 metal-oxo (O*) sites can be thermodynamically (ΔG_r^{400K} = -40 kJ/mol) possible on **Mo-Only** Te-Free active sites. This configuration leads to formation of isopropanol, when activated propyl radical is adsorbed in one M-Oxo site and neighboring M-OH site transfers the H atom instantly (Figure 6.9b). Nevertheless Te-free **3V3V** active site can only have 2 metal-oxo, hence it completely prohibits the fast H-migration on the active site.

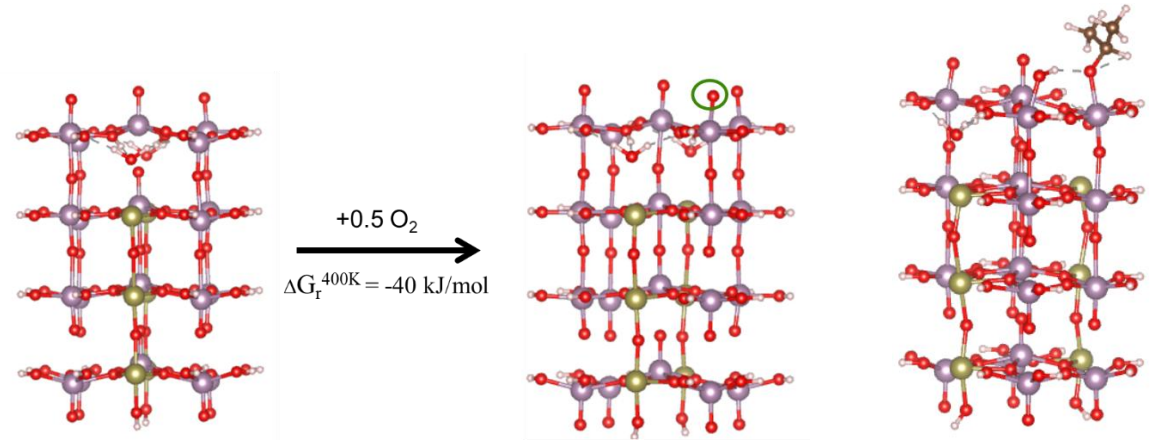

Figure 6.9. (a) Te free Mo-only active site can thermodynamically have three metal-oxo sites, as shown here. (b) The presence of neighboring metal-oxo sites facilitates isopropanol generation, via the two-step mechanism, such as first by adsorbing propyl radical strongly and then fast H-migration from neighboring M-OH site towards it as shown here.

- ***Comparison of MEPs between with and without Te active sites:***

The two possible pathways, as discussed in last chapter in Figure 5.8, availability of M-oxo site adsorbs the propyl radical immediately after first propane CH activation. Then the proximity of neighboring M-OH group facilitates isopropanol formation. Otherwise, if there is no M-oxo site available, the propyl abstracts the second hydrogen at M-OH site to form a water and a propylene molecule. With this observation, if the starting surface is at SOX = 6, the full catalytic cycle forms an isopropanol and a propylene molecule on **Mo-only** surface. Both MEPs for **Mo-only** with and without Te at the top layer are shown in Figure 6.10. The surface ids with a prime sign, for example **3a', 4a'** etc, are indicated for Te-Free surface and presented in appendix Figure AF3 and AF4 and all the raw DFT calculated data are provided in appendix Table AT9. There are three M-oxo sites present on Te-free **Mo-only** site; hence it also forms isopropanol in the first half of the catalytic cycle. Nevertheless, in the second half of the cycle, the propyl radical remains adsorbed on **3a',** as abstracting the second hydrogen and forming the surface **2a'** and propylene are thermodynamically 455 kJ/mol endothermic and not favorable. The CH activation barriers in Te-free **Mo-only** surface are also higher compared to normal active sites with Te. Hence this study interprets that the M1 catalyst without Te is highly unselective to propylene formation. Since removal of Te and consecutive H-termination at O2 and O4 sites have no effect

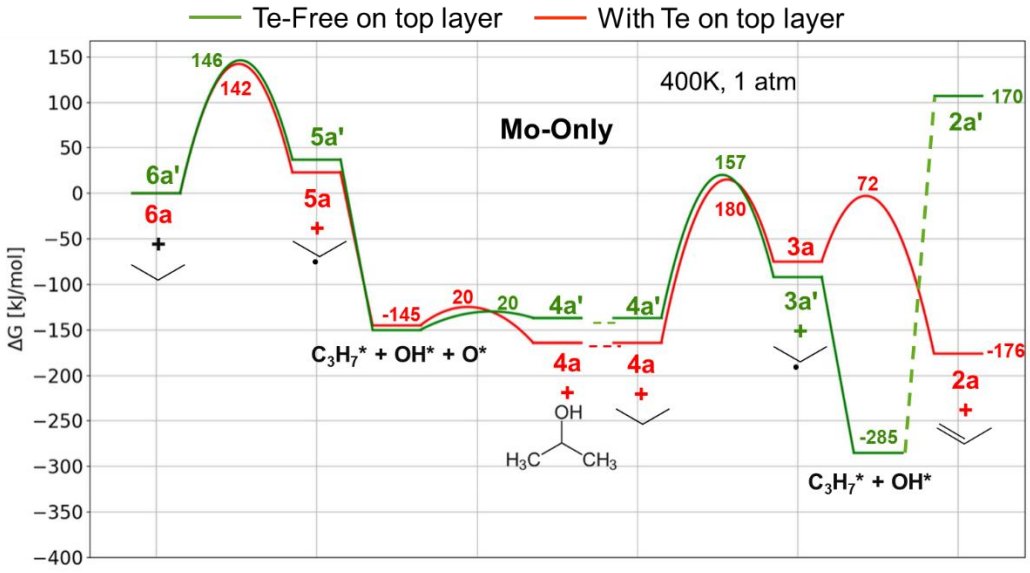

*Figure 6.10. Minimum energy pathways of propane oxidation to isopropanol and propylene on **Mo-Only** active site for both configurations such as, with Te on the top layer (green line) and without Te at the top layer (Red line) are presented here.*

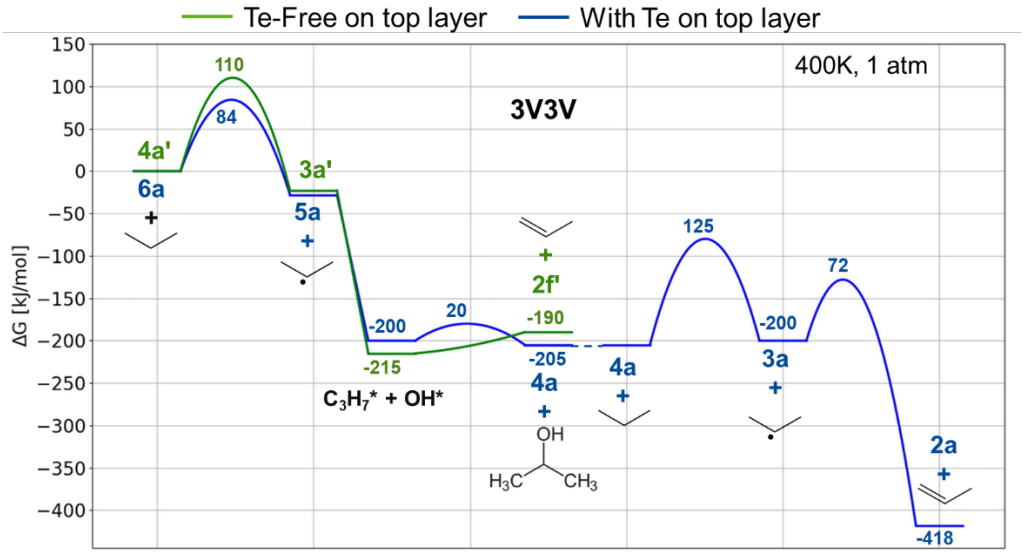

*Figure 6.11. Minimum energy pathways of propane oxidation to isopropanol and propylene on **3V3V** active site for both configurations such as, with Te on the top layer (green line) and without Te at the top layer (Red line) are presented here.*

on the oxidation state of the Mo-Oxo site, it has not resulted in a reduced activation barrier. On the other hand, the absence of the weak H-bond interaction with the neighboring oxygen at Te with the H atom at Mo-OH site in Te-free structure, could possibly be the reason for the elevated CH activation barrier.

The MEP for **3V3V** surface active site is depicted in Figure 6.11. Propane activation barrier on this active site is substantially low as 84 kJ/mol as also shown previously in

Figure 6.3a. But it may still facilitate the formation of isopropanol due to the presence of M-oxo site and Te-OH sites in the vicinity. On the other hand, the very low propyl abstraction barrier from gas phase can also compete with it and form a propylene molecule immediately in the first half of the catalytic cycle. Whereas, due to the reason, Te-free **3V3V** active site can adsorb maximum two oxygen atoms on two Mo sites, propylene formation is highly favorable already in the first half of the cycle from the starting surface **4a'**. Nevertheless, the first CH activation barrier increases to 110 kJ/mol in absence of Te, but the CH activation barrier for adsorbed propyl radical is substantially low as 21 kJ/mol and it leads to propylene formation and form surface **2f'**. Since H-migration between the Mo-oxo sites cannot happen via central Mo-Oxo site because of its large barrier, the formation of isopropanol from adsorbed propyl radical is prohibited. Hence, this finding tells that Te-free **3V3V** active site is not only active but also more selective towards propylene formation.

6.5 Conclusion of the chapter

In this chapter, systematic creation of cluster models with V in the top two layers is presented. A trend in reduction of CH activation barrier appeared with an increase of vanadium content, especially in the 2nd layer. Three vanadium in each layer situated diagonally has been found to be the most prominent optimum configuration. Deeper analysis of spin density, geometrical distortion says that vanadium oxidizes the neighboring molybdenum making Mo-Oxo site more active for CH activation. Later the Te-free model is investigated to understand the effect of absence of Te on the top layer on propane oxidation. CH activation barrier is slightly increased on Te-free active site, nevertheless absence of Te prohibits the oxygen insertion mechanism mainly in presence of V. This should lead to more selectivity towards propylene for Mo-V-Te-Nb-O M1 catalyst.

7. Conclusion and Outlook

In this dissertation, I have conducted a comprehensive computational investigation into the selective oxidation of propane to propylene and its further transformation into oxygenated products such as acrolein, isopropanol, allyl alcohol, and ultimately acrylic acid. The study focuses on the M1 phase of the Mo-V-Te-Nb-O catalyst, employing ab initio quantum chemical calculations.

The mechanistic study is grounded in C–H bond activation and subsequent radical-like reaction pathways. To simplify the complex surface chemistry, I systematically developed a vanadium-free Mo-only cluster model representing the catalytic active site of the M1 phase.

A detailed benchmarking of density functional theory (DFT) methods against multireference approaches revealed that the M06 hybrid-DFT functional is essential for accurately capturing both kinetic and thermodynamic parameters. I demonstrated that the Linear Scaling Relationship (LSR) holds true even for complex catalyst surfaces like M1. This finding is critical for: Rapid estimation of activation barriers, microkinetic modeling and understanding catalytic activity trends.

In Chapter 4, the complete catalytic cycle for the selective oxidation of two propane molecules is established, resulting in the formation of two propylene and two water molecules. All possible surface states were considered, incorporating Oxygen and water adsorption/desorption, fast hydrogen migration and dynamic surface configurations. The results qualitatively reproduce the high activation barriers, explaining the low activity of the Mo-only catalyst in propylene formation.

In Chapter 5, the investigation to the activity of the propyl radical on the Mo-only surface is performed. I established a universal LSR for C–H activation barriers across various species—propane, propyl, propylene, and allyl alcohol—using the descriptors, such as, Hydrogen binding energy (E_H), Bond dissociation energy (ΔE_{BDE}) and two correction terms:

- ΔE_{int}^{TS}: Accounts for changes in diradical interaction energy at the transition state (mainly due to radical delocalization),

- E_{MO}: Represents additional stabilization from interactions between oxygen-containing functional groups and the catalyst surface (e.g., hydrogen bonding).

Since these correction terms are difficult to compute directly, they were estimated using our calculations and previously published data.

Calculations show that when a radical species is adsorbed on a metal-oxo site, fast hydrogen migration from a neighboring metal-OH site facilitates –OH group insertion, leading to the formation of oxygenated compounds. This pathway is crucial for formation of oxygenated compounds in selective path and the reason for formation of isopropanol from adsorbed propyl radical as an undesired product. This mechanism is a key factor influencing catalytic performance and contributes to reduced selectivity in the direct one-step oxidation of propane to acrylic acid on the M1 catalyst. Notably, this issue is absent in the current industrial two-stage process, where propane is first oxidized to propylene and then to acrylic acid using two different selective mixed-metal oxide catalysts.

Further mechanistic pathways for four selective reactions, such as, propane to propylene, propylene to allyl alcohol, allyl alcohol to acrolein and acrolein to acrylic acid and one unselective reaction for propane to isopropanol are generated.

According to our LSR model, the activation of propylene to acrylic acid is not energetically demanding on Mo-only sites. This suggests that the V-free M2 phase could serve as an active component for propylene oxidation, whereas vanadium-containing M1 sites are essential for propane activation. All activation barrier data are provided to support further microkinetic modeling.

In Chapter 6, molybdenum is systematically substituted with vanadium in the top two layers of the cluster model and computed the minimum energy pathways for propane-to-propylene conversion. The results show a systematic reduction in C–H activation barriers with increasing vanadium content. The optimal configuration, featuring three vanadium atoms in the top two layers, exhibits a propane activation barrier of 84 kJ/mol, consistent with experimental values[43]. A deeper analysis of geometry and electron density reveals that vanadium oxidizes neighboring Mo sites, enhancing their reactivity toward C–H activation. Finally, we modeled a Te-free surface, as reported in

experimental studies due to hydrolysis. While Te removal has minimal impact on activity, it inhibits fast hydrogen migration, thereby increasing selectivity toward propylene.

Despite the extensive investigation of reaction mechanisms and surface dynamics presented in this dissertation, further exploration is needed to uncover additional pathways that may occur on the M1 catalytic surface during the selective oxidation of propane to acrylic acid. One such pathway is the surface-stabilized mechanism, which warrants deeper analysis. Different reaction mechanisms can lead to varied products and significantly influence catalytic performance. For instance, the formation of acetone from propylene, the decomposition of acrylic acid into C_2 products like ethylene via C=C cleavage, or the generation of propionaldehyde via oxidation of the primary carbon in propane or propylene are not addressed in this work. Understanding these alternative pathways is essential to identifying the limitations in selectivity toward acrylic acid on the M1 catalyst.

The current Linear Scaling Relationship (LSR) model suggests that activating the primary carbon of propane is more challenging than the secondary carbon. This implies a limitation in the model's ability to capture the full spectrum of by-product formation, as reported in experimental literature[43]. To improve the robustness and general applicability of the LSR model, further refinement and validation are necessary. The two correction terms introduced in our LSR model, Metal–oxygen interactions between gas-phase species and the surface, and Radical interactions at the transition state with the catalyst surface. While these corrections enhance the model's predictive power, they require further validation through additional computational data across a broader range of gas species and surface configurations. A deeper electronic structure analysis helps clarify the origin and applicability of these descriptors. As an immediate extension of this work, high-throughput theoretical screening using various metal substitutions could provide valuable insights for rational catalyst design. However, the inherent complexity of the M1 catalytic material presents a significant challenge for large-scale quantum chemical simulations.

Although periodic surface simulations could offer more comprehensive insights into reaction mechanisms, they are computationally expensive and impractical for exploring all combinatorial possibilities with high accuracy for M1 type catalyst. To address this,

I propose leveraging our generated data and models for machine learning (ML) integration. Specifically:

1. Training ML models based on interatomic potential can accelerate quantum chemical investigations.
2. Large-scale molecular dynamics simulations using ML-trained force fields (MLFF) in hydrated environments can reveal deeper insights into surface phenomena and catalytic behavior.
3. Rapid descriptor generation via ML will streamline catalyst screening and guide experimental efforts more efficiently.

I believe the descriptors proposed in this work will play a pivotal role in developing statistical models that predict experimental catalytic performance. When combined with experimental descriptors, these models can enhance the accuracy and reliability of catalyst design. Nonetheless, further research is needed to discover, understand and identify additional theoretical descriptors that can enrich modeling efforts to describe catalytic performance. This will support the rational design, development, and understanding of the M1 catalyst and heterogeneous catalysis more broadly.

References

(1) Mezhuev, Ya O.; Tsatsakis, A.; Taghizadehghalehjoughi, A. Acrylic Acid. In *Encyclopedia of Toxicology*; Elsevier, 2024; pp 135–138. https://doi.org/10.1016/B978-0-12-824315-2.00936-2.

(2) Lin, M. M. Selective Oxidation of Propane to Acrylic Acid with Molecular Oxygen. *Appl. Catal. Gen.* **2001**, *207* (1–2), 1–16. https://doi.org/10.1016/S0926-860X(00)00609-8.

(3) Ohara, T.; Sato, T.; Shimizu, N.; Prescher, G.; Schwind, H.; Weiberg, O.; Marten, K.; Greim, H.; Shaffer, T. D.; Nandi, P. Acrylic Acid and Derivatives. In *Ullmann's Encyclopedia of Industrial Chemistry*; Wiley-VCH Verlag GmbH & Co. KGaA, Ed.; Wiley, 2020; pp 1–21. https://doi.org/10.1002/14356007.a01_161.pub4.

(4) Amakawa, K.; Mauß, J. M.; Müller, P.; Hinrichsen, B.; Hirth, S.; Bader, A.; Price, S. W. T.; Jacques, S. D. M.; Macht, J. Architecture of Industrial Bi-Mo-Co-Fe-K-O Propene Oxidation Catalysts. *Sci. Adv.* **2023**, *9* (28), eadh5331. https://doi.org/10.1126/sciadv.adh5331.

(5) Knoche, S.; Heid, M.; Gora, N.; Ohlig, D.; Drochner, A.; Etzold, B.; Vogel, H. Mechanistic Study on the Selective Oxidation of Acrolein to Acrylic Acid Concerning the Role of Water. *ChemCatChem* **2020**, *12* (13), 3560–3575. https://doi.org/10.1002/cctc.201902348.

(6) Bettahar, M.; Costentin, G.; Savary, L.; Lavalley, J. On the Partial Oxidation of Propane and Propylene on Mixed Metal Oxide Catalysts. *Appl. Catal. Gen.* **1996**, *145* (1–2), 1–48. https://doi.org/10.1016/0926-860X(96)00138-X.

(7) Shiju, N. R.; Guliants, V. V. Recent Developments in Catalysis Using Nanostructured Materials. *Appl. Catal. Gen.* **2009**, *356* (1), 1–17. https://doi.org/10.1016/j.apcata.2008.11.034.

(8) Védrine, J. Heterogeneous Partial (Amm)Oxidation and Oxidative Dehydrogenation Catalysis on Mixed Metal Oxides. *Catalysts* **2016**, *6* (2), 22. https://doi.org/10.3390/catal6020022.

(9) Ushikubo, T.; Oshima, K.; Kayo, A.; Umezawa, T.; Kiyono, K.; Sawaki, I.; Nakamura, H. Catalyst for the Production of Nitriles. US5472925A.

(10) Grasselli, R. K.; Buttrey, D. J.; DeSanto, P.; Burrington, J. D.; Lugmair, C. G.; Volpe, A. F.; Weingand, T. Active Centers in Mo–V–Nb–Te–O (Amm)Oxidation Catalysts. *Catal. Today* **2004**, *91–92*, 251–258. https://doi.org/10.1016/j.cattod.2004.03.060.

(11) Aouine, M.; Millet, J. M. M.; Dubois, J. L. Crystal Chemistry and Phase Composition of the MoVTeNbO Catalysts for the Ammoxidation of Propane. *Chem. Commun.* **2001**, No. 13, 1180–1181. https://doi.org/10.1039/b103895h.

(12) DeSanto, P.; Buttrey, D. J.; Grasselli, R. K.; Lugmair, C. G.; Volpe, A. F.; Toby, B. H.; Vogt, T. Structural Aspects of the *M* 1 and *M* 2 Phases in MoVNbTeO Propane Ammoxidation Catalysts. *Z. Für Krist. - Cryst. Mater.* **2004**, *219* (3), 152–165. https://doi.org/10.1524/zkri.219.3.152.29091.

(13) Ueda, W.; Vitry, D.; Katou, T. Structural Organization of Catalytic Functions in Mo-Based Oxides for Propane Selective Oxidation. *Catal. Today* **2004**, *96* (4), 235–240. https://doi.org/10.1016/j.cattod.2004.06.147.

(14) Grasselli, R. K.; Burrington, J. D.; Buttrey, D. J.; DeSanto Jr., P.; Lugmair, C. G.; Volpe Jr., A. F.; Weingand, T. Multifunctionality of Active Centers in (Amm)Oxidation Catalysts: From Bi–Mo–O x to Mo–V–Nb–(Te, Sb)–O x. *Top. Catal.* **2003**, *23* (1/4), 5–22. https://doi.org/10.1023/A:1024859917786.

(15) Celayasanfiz, A.; Hansen, T.; Sakthivel, A.; Trunschke, A.; Schlogl, R.; Knoester, A.; Brongersma, H.; Looi, M.; Hamid, S. How Important Is the (001) Plane of M1 for Selective Oxidation of Propane to Acrylic Acid? *J. Catal.* **2008**, *258* (1), 35–43. https://doi.org/10.1016/j.jcat.2008.05.028.

(16) Li, X.; Buttrey, D. J.; Blom, D. A.; Vogt, T. Improvement of the Structural Model for the M1 Phase Mo–V–Nb–Te–O Propane (Amm)Oxidation Catalyst. *Top. Catal.* **2011**, *54* (10–12), 614–626. https://doi.org/10.1007/s11244-011-9684-z.

(17) Masliuk, L.; Heggen, M.; Noack, J.; Girgsdies, F.; Trunschke, A.; Hermann, K. E.; Willinger, M. G.; Schlögl, R.; Lunkenbein, T. Structural Complexity in Heterogeneous Catalysis: Cataloging Local Nanostructures. *J. Phys. Chem. C* **2017**, *121* (43), 24093–24103. https://doi.org/10.1021/acs.jpcc.7b08333.

(18) Grasselli, R. K.; Lugmair, C. G.; Volpe, A. F. Towards an Understanding of the Reaction Pathways in Propane Ammoxidation Based on the Distribution of Elements at the ActiveCenters of the M1 Phase of the MoV(Nb,Ta)TeO System. *Top. Catal.* **2011**, *54* (10–12), 595–604. https://doi.org/10.1007/s11244-011-9681-2.

(19) Korovchenko, P.; Shiju, N. R.; Dozier, A. K.; Graham, U. M.; Guerrero-Pérez, M. O.; Guliants, V. V. M1 to M2 Phase Transformation and Phase Cooperation in Bulk Mixed Metal Mo–V–M–O (M=Te, Nb) Catalysts for Selective Ammoxidation of Propane. *Top. Catal.* **2008**, *50* (1–4), 43–51. https://doi.org/10.1007/s11244-008-9098-8.

(20) Grasselli, R. K. Advances and Future Trends in Selective Oxidation and Ammoxidation Catalysis. *Catal. Today* **1999**, *49* (1–3), 141–153. https://doi.org/10.1016/S0920-5861(98)00418-0.

(21) Grasselli, R. K. Selectivity Issues in (Amm)Oxidation Catalysis. *Catal. Today* **2005**, *99* (1–2), 23–31. https://doi.org/10.1016/j.cattod.2004.09.021.

(22) Woo, J.; Sanghavi, U.; Vonderheide, A.; Guliants, V. V. A Study of M1/M2 Phase Synergy in the MoVTe(Nb,Ta)O Catalysts for Propane Ammoxidation to Acrylonitrile. *Appl. Catal. Gen.* **2016**, *515*, 179–189. https://doi.org/10.1016/j.apcata.2016.01.038.

(23) Shiju, N. R.; Guliants, V. V.; Overbury, S. H.; Rondinone, A. J. Toward Environmentally Benign Oxidations: Bulk Mixed Mo-V-(Te-Nb)-O M1 Phase Catalysts for the Selective

Ammoxidation of Propane. *ChemSusChem* **2008**, *1* (6), 519–523. https://doi.org/10.1002/cssc.200800039.

(24) Yu, J.; Xu, Y.; Guliants, V. V. Propane Ammoxidation over Mo–V–Te–Nb–O M1 Phase: Density Functional Theory Study of Propane Oxidative Dehydrogenation Steps. *Catal. Today* **2014**, *238*, 28–34. https://doi.org/10.1016/j.cattod.2014.02.053.

(25) Yu, J.; Xu, Y.; Guliants, V. V. Propane Ammoxidation over Mo–V–Te–Nb–O M1 Phase Investigated by DFT: Elementary Steps of Ammonia Adsorption, Activation and NH Insertion into π-Allyl Intermediate. *Top. Catal.* **2014**, *57* (14–16), 1145–1151. https://doi.org/10.1007/s11244-014-0280-x.

(26) DeSanto, P.; Buttrey, D. J.; Grasselli, R. K.; Pyrz, W. D.; Lugmair, C. G.; Volpe, A. F.; Vogt, T.; Toby, B. H. Comparison of MoVTaTeO and MoVNbTeO M1 Crystal Chemistry. *Top. Catal.* **2006**, *38* (1–3), 31–40. https://doi.org/10.1007/s11244-006-0068-8.

(27) Shiju, N. R.; Liang, X.; Weimer, A. W.; Liang, C.; Dai, S.; Guliants, V. V. The Role of Surface Basal Planes of Layered Mixed Metal Oxides in Selective Transformation of Lower Alkanes: Propane Ammoxidation over Surface *Ab* Planes of Mo−V−Te−Nb−O M1 Phase. *J. Am. Chem. Soc.* **2008**, *130* (18), 5850–5851. https://doi.org/10.1021/ja800575v.

(28) Fu, G.; Xu, X.; Lu, X.; Wan, H. Mechanisms of Initial Propane Activation on Molybdenum Oxides: A Density Functional Theory Study. *J. Phys. Chem. B* **2005**, *109* (13), 6416–6421. https://doi.org/10.1021/jp0454974.

(29) Che-Galicia, G.; Quintana-Solórzano, R.; Ruiz-Martínez, R. S.; Valente, J. S.; Castillo-Araiza, C. O. Kinetic Modeling of the Oxidative Dehydrogenation of Ethane to Ethylene over a MoVTeNbO Catalytic System. *Chem. Eng. J.* **2014**, *252*, 75–88. https://doi.org/10.1016/j.cej.2014.04.042.

(30) Schlögl, R. Active Sites for Propane Oxidation: Some Generic Considerations. *Top. Catal.* **2011**, *54* (10–12), 627–638. https://doi.org/10.1007/s11244-011-9683-0.

(31) Panov, G.; Dubkov, K.; Starokon, E. Active Oxygen in Selective Oxidation Catalysis. *Catal. Today* **2006**, *117* (1–3), 148–155. https://doi.org/10.1016/j.cattod.2006.05.019.

(32) Kolen'ko, Y. V.; Zhang, W.; d'Alnoncourt, R. N.; Girgsdies, F.; Hansen, T. W.; Wolfram, T.; Schlögl, R.; Trunschke, A. Synthesis of MoVTeNb Oxide Catalysts with Tunable Particle Dimensions. *ChemCatChem* **2011**, *3* (10), 1597–1606. https://doi.org/10.1002/cctc.201100089.

(33) Chu, B.; An, H.; Chen, X.; Cheng, Y. Phase-Pure M1 MoVNbTeO x Catalysts with Tunable Particle Size for Oxidative Dehydrogenation of Ethane. *Appl. Catal. Gen.* **2016**, *524*, 56–65. https://doi.org/10.1016/j.apcata.2016.05.026.

(34) Melzer, D.; Xu, P.; Hartmann, D.; Zhu, Y.; Browning, N. D.; Sanchez-Sanchez, M.; Lercher, J. A. Atomic-Scale Determination of Active Facets on the MoVTeNb Oxide M1 Phase and Their Intrinsic Catalytic Activity for Ethane Oxidative Dehydrogenation. *Angew. Chem. Int. Ed.* **2016**, *55* (31), 8873–8877. https://doi.org/10.1002/anie.201600463.

(35) Ishikawa, S.; Yi, X.; Murayama, T.; Ueda, W. Heptagonal Channel Micropore of Orthorhombic Mo3VOx as Catalysis Field for the Selective Oxidation of Ethane. *Appl. Catal. Gen.* **2014**, *474*, 10–17. https://doi.org/10.1016/j.apcata.2013.07.050.

(36) Ishikawa, S.; Yi, X.; Murayama, T.; Ueda, W. Catalysis Field in Orthorhombic Mo3VOx Oxide Catalyst for the Selective Oxidation of Ethane, Propane and Acrolein. *Catal. Today* **2014**, *238*, 35–40. https://doi.org/10.1016/j.cattod.2013.12.054.

(37) Sadakane, M.; Ohmura, S.; Kodato, K.; Fujisawa, T.; Kato, K.; Shimidzu, K.; Murayama, T.; Ueda, W. Redox Tunable Reversible Molecular Sieves: Orthorhombic Molybdenum Vanadium Oxide. *Chem. Commun.* **2011**, *47* (38), 10812. https://doi.org/10.1039/c1cc13454j.

(38) Annamalai, L.; Ezenwa, S.; Dang, Y.; Tan, H.; Suib, S. L.; Deshlahra, P. Comparison of Structural and Catalytic Properties of Monometallic Mo and V Oxides and M1 Phase Mixed Oxides for Oxidative Dehydrogenation. *Catal. Today* **2021**, *368*, 28–45. https://doi.org/10.1016/j.cattod.2020.04.046.

(39) Annamalai, L.; Liu, Y.; Ezenwa, S.; Dang, Y.; Suib, S. L.; Deshlahra, P. Influence of Tight Confinement on Selective Oxidative Dehydrogenation of Ethane on MoVTeNb Mixed Oxides. *ACS Catal.* **2018**, *8* (8), 7051–7067. https://doi.org/10.1021/acscatal.8b01586.

(40) Liu, Y.; Annamalai, L.; Deshlahra, P. Effects of Lattice O Atom Coordination and Pore Confinement on Selectivity Limitations for Ethane Oxidative Dehydrogenation Catalyzed by Vanadium-Oxo Species. *J. Phys. Chem. C* **2019**, *123* (46), 28168–28191. https://doi.org/10.1021/acs.jpcc.9b07778.

(41) Hävecker, M.; Wrabetz, S.; Kröhnert, J.; Csepei, L.-I.; Naumann d'Alnoncourt, R.; Kolen'ko, Y. V.; Girgsdies, F.; Schlögl, R.; Trunschke, A. Surface Chemistry of Phase-Pure M1 MoVTeNb Oxide during Operation in Selective Oxidation of Propane to Acrylic Acid. *J. Catal.* **2012**, *285* (1), 48–60. https://doi.org/10.1016/j.jcat.2011.09.012.

(42) Naumann d'Alnoncourt, R.; Csepei, L.-I.; Hävecker, M.; Girgsdies, F.; Schuster, M. E.; Schlögl, R.; Trunschke, A. The Reaction Network in Propane Oxidation over Phase-Pure MoVTeNb M1 Oxide Catalysts. *J. Catal.* **2014**, *311*, 369–385. https://doi.org/10.1016/j.jcat.2013.12.008.

(43) Kube, P.; Frank, B.; Schlögl, R.; Trunschke, A. Isotope Studies in Oxidation of Propane over Vanadium Oxide. *ChemCatChem* **2017**, *9* (18), 3446–3455. https://doi.org/10.1002/cctc.201700847.

(44) Wernbacher, A. M.; Kube, P.; Hävecker, M.; Schlögl, R.; Trunschke, A. Electronic and Dielectric Properties of MoV-Oxide (M1 Phase) under Alkane Oxidation Conditions. *J. Phys. Chem. C* **2019**, *123* (21), 13269–13282. https://doi.org/10.1021/acs.jpcc.9b01273.

(45) Cheng, M.-J.; Goddard, W. A. I. In Silico Design of Highly Selective Mo-V-Te-Nb-O Mixed Metal Oxide Catalysts for Ammoxidation and Oxidative Dehydrogenation of Propane and

Ethane. *J. Am. Chem. Soc.* **2015**, *137* (41), 13224–13227. https://doi.org/10.1021/jacs.5b07073.

(46) Melzer, D.; Mestl, G.; Wanninger, K.; Jentys, A.; Sanchez-Sanchez, M.; Lercher, J. A. On the Promoting Effects of Te and Nb in the Activity and Selectivity of M1 MoV-Oxides for Ethane Oxidative Dehydrogenation. *Top. Catal.* **2020**, *63* (19–20), 1754–1764. https://doi.org/10.1007/s11244-020-01304-0.

(47) Trunschke, A.; Noack, J.; Trojanov, S.; Girgsdies, F.; Lunkenbein, T.; Pfeifer, V.; Hävecker, M.; Kube, P.; Sprung, C.; Rosowski, F.; Schlögl, R. The Impact of the Bulk Structure on Surface Dynamics of Complex Mo–V-Based Oxide Catalysts. *ACS Catal.* **2017**, *7* (4), 3061–3071. https://doi.org/10.1021/acscatal.7b00130.

(48) Fjermestad, T.; Li, W.; Rugg, G.; Ishida, S.; Okuno, M.; Sagi, K.; Genest, A.; Rösch, N. Acrolein Oxidation to Acrylic Acid over the MoVOx Material. Insights from DFT Modeling. *Appl. Catal. Gen.* **2018**, *565*, 68–75. https://doi.org/10.1016/j.apcata.2018.07.044.

(49) Liu, Y.; Twombly, A.; Dang, Y.; Mirich, A.; Suib, S. L.; Deshlahra, P. Roles of Enhancement of C−H Activation and Diminution of C−O Formation Within M1-Phase Pores in Propane Selective Oxidation. *ChemCatChem* **2021**, *13* (3), 882–899. https://doi.org/10.1002/cctc.202001642.

(50) Deshlahra, P.; Iglesia, E. Reactivity and Selectivity Descriptors for the Activation of C–H Bonds in Hydrocarbons and Oxygenates on Metal Oxides. *J. Phys. Chem. C* **2016**, *120* (30), 16741–16760. https://doi.org/10.1021/acs.jpcc.6b04604.

(51) Li, W.-Q.; Fjermestad, T.; Genest, A.; Rösch, N. Reactivity Trends of the $MoVO_x$ Mixed Metal Oxide Catalyst from Density Functional Modeling. *Catal. Sci. Technol.* **2019**, *9* (7), 1559–1569. https://doi.org/10.1039/C8CY02545B.

(52) Sabatier, P. *La catalyse en chimie organique*, 2. ed., rev. et augm.; Librairie polytechnique Paris et Liege: Paris et Liege, 1920.

(53) Medford, A. J.; Vojvodic, A.; Hummelshøj, J. S.; Voss, J.; Abild-Pedersen, F.; Studt, F.; Bligaard, T.; Nilsson, A.; Nørskov, J. K. From the Sabatier Principle to a Predictive Theory of Transition-Metal Heterogeneous Catalysis. *J. Catal.* **2015**, *328*, 36–42. https://doi.org/10.1016/j.jcat.2014.12.033.

(54) Studt, F.; Sharafutdinov, I.; Abild-Pedersen, F.; Elkjær, C. F.; Hummelshøj, J. S.; Dahl, S.; Chorkendorff, I.; Nørskov, J. K. Discovery of a Ni-Ga Catalyst for Carbon Dioxide Reduction to Methanol. *Nat. Chem.* **2014**, *6* (4), 320–324. https://doi.org/10.1038/nchem.1873.

(55) Kaiser, S. K.; Fako, E.; Surin, I.; Krumeich, F.; Kondratenko, V. A.; Kondratenko, E. V.; Clark, A. H.; López, N.; Pérez-Ramírez, J. Performance Descriptors of Nanostructured Metal Catalysts for Acetylene Hydrochlorination. *Nat. Nanotechnol.* **2022**, *17* (6), 606–612. https://doi.org/10.1038/s41565-022-01105-4.

(56) Zhao, Z.-J.; Liu, S.; Zha, S.; Cheng, D.; Studt, F.; Henkelman, G.; Gong, J. Theory-Guided Design of Catalytic Materials Using Scaling Relationships and Reactivity Descriptors. *Nat. Rev. Mater.* **2019**, *4* (12), 792–804. https://doi.org/10.1038/s41578-019-0152-x.

(57) Araujo-Lopez, E. Theoretical Insights into the Light Alkanes Dehydrogenation and Aldehydes Hydrogenation on Transition Metal and Metal Oxide Surfaces, Karlsruher Institut für Technologie (KIT), 2022. https://doi.org/10.5445/IR/1000152395.

(58) Metiu, H.; Chrétien, S.; Hu, Z.; Li, B.; Sun, X. Chemistry of Lewis Acid–Base Pairs on Oxide Surfaces. *J. Phys. Chem. C* **2012**, *116* (19), 10439–10450. https://doi.org/10.1021/jp301341t.

(59) Latimer, A. A.; Kulkarni, A. R.; Aljama, H.; Montoya, J. H.; Yoo, J. S.; Tsai, C.; Abild-Pedersen, F.; Studt, F.; Nørskov, J. K. Understanding Trends in C–H Bond Activation in Heterogeneous Catalysis. *Nat. Mater.* **2017**, *16* (2), 225–229. https://doi.org/10.1038/nmat4760.

(60) Xu, J.; Cao, X.-M.; Hu, P. Improved Prediction for the Methane Activation Mechanism on Rutile Metal Oxides by a Machine Learning Model with Geometrical Descriptors. *J. Phys. Chem. C* **2019**, *123* (47), 28802–28810. https://doi.org/10.1021/acs.jpcc.9b08939.

(61) Evans, M. G.; Polanyi, M. Inertia and Driving Force of Chemical Reactions. *Trans. Faraday Soc.* **1938**, *34*, 11. https://doi.org/10.1039/tf9383400011.

(62) Bronsted, J. N. Acid and Basic Catalysis. *Chem. Rev.* **1928**, *5* (3), 231–338. https://doi.org/10.1021/cr60019a001.

(63) Abild-Pedersen, F.; Greeley, J.; Studt, F.; Rossmeisl, J.; Munter, T. R.; Moses, P. G.; Skúlason, E.; Bligaard, T.; Nørskov, J. K. Scaling Properties of Adsorption Energies for Hydrogen-Containing Molecules on Transition-Metal Surfaces. *Phys. Rev. Lett.* **2007**, *99* (1), 016105. https://doi.org/10.1103/PhysRevLett.99.016105.

(64) Greeley, J. Theoretical Heterogeneous Catalysis: Scaling Relationships and Computational Catalyst Design. *Annu. Rev. Chem. Biomol. Eng.* **2016**, *7* (1), 605–635. https://doi.org/10.1146/annurev-chembioeng-080615-034413.

(65) Dixit, M.; Kostetskyy, P.; Mpourmpakis, G. Structure–Activity Relationships in Alkane Dehydrogenation on γ-Al_2O_3: Site-Dependent Reactions. *ACS Catal.* **2018**, *8* (12), 11570–11578. https://doi.org/10.1021/acscatal.8b03484.

(66) Born, M.; Oppenheimer, R. Zur Quantentheorie Der Molekeln. *Ann. Phys.* **1927**, *389* (20), 457–484. https://doi.org/10.1002/andp.19273892002.

(67) Thomas, L. H. The Calculation of Atomic Fields. *Math. Proc. Camb. Philos. Soc.* **1927**, *23* (5), 542–548. https://doi.org/10.1017/S0305004100011683.

(68) Fermi, E. Un Metodo Statistico per La Determinazione Di Alcune Prioprietà Dell'Atomo. *Rend Accad Naz Lincei* **1927**, *6*, 602–607.

(69) Hohenberg, P.; Kohn, W. Inhomogeneous Electron Gas. *Phys. Rev.* **1964**, *136* (3B), B864–B871. https://doi.org/10.1103/PhysRev.136.B864.

(70) Kohn, W.; Sham, L. J. Self-Consistent Equations Including Exchange and Correlation Effects. *Phys. Rev.* **1965**, *140* (4A), A1133–A1138. https://doi.org/10.1103/PhysRev.140.A1133.

(71) Barth, U. von; Hedin, L. A Local Exchange-Correlation Potential for the Spin Polarized Case. i. *J. Phys. C Solid State Phys.* **1972**, *5* (13), 1629–1642. https://doi.org/10.1088/0022-3719/5/13/012.

(72) Wigner, E. Effects of the Electron Interaction on the Energy Levels of Electrons in Metals. *Trans. Faraday Soc.* **1938**, *34*, 678. https://doi.org/10.1039/tf9383400678.

(73) Ceperley, D. M.; Alder, B. J. Ground State of the Electron Gas by a Stochastic Method. *Phys. Rev. Lett.* **1980**, *45* (7), 566–569. https://doi.org/10.1103/PhysRevLett.45.566.

(74) Burke, K.; Perdew, J. P.; Wang, Y. Derivation of a Generalized Gradient Approximation: The PW91 Density Functional. In *Electronic Density Functional Theory*; Dobson, J. F., Vignale, G., Das, M. P., Eds.; Springer US: Boston, MA, 1998; pp 81–111. https://doi.org/10.1007/978-1-4899-0316-7_7.

(75) Perdew, J. P.; Burke, K.; Ernzerhof, M. Generalized Gradient Approximation Made Simple. *Phys. Rev. Lett.* **1996**, *77* (18), 3865–3868. https://doi.org/10.1103/PhysRevLett.77.3865.

(76) Becke, A. D. Density-Functional Exchange-Energy Approximation with Correct Asymptotic Behavior. *Phys. Rev. A* **1988**, *38* (6), 3098–3100. https://doi.org/10.1103/PhysRevA.38.3098.

(77) Lee, C.; Yang, W.; Parr, R. G. Development of the Colle-Salvetti Correlation-Energy Formula into a Functional of the Electron Density. *Phys. Rev. B* **1988**, *37* (2), 785–789. https://doi.org/10.1103/PhysRevB.37.785.

(78) Tao, J.; Perdew, J. P.; Staroverov, V. N.; Scuseria, G. E. Climbing the Density Functional Ladder: Nonempirical Meta–Generalized Gradient Approximation Designed for Molecules and Solids. *Phys. Rev. Lett.* **2003**, *91* (14), 146401. https://doi.org/10.1103/PhysRevLett.91.146401.

(79) Ernzerhof, M.; Scuseria, G. E. Assessment of the Perdew–Burke–Ernzerhof Exchange-Correlation Functional. *J. Chem. Phys.* **1999**, *110* (11), 5029–5036. https://doi.org/10.1063/1.478401.

(80) Hertwig, R. H.; Koch, W. On the Parameterization of the Local Correlation Functional. What Is Becke-3-LYP? *Chem. Phys. Lett.* **1997**, *268* (5–6), 345–351. https://doi.org/10.1016/S0009-2614(97)00207-8.

(81) Stephens, P. J.; Devlin, F. J.; Chabalowski, C. F.; Frisch, M. J. Ab Initio Calculation of Vibrational Absorption and Circular Dichroism Spectra Using Density Functional Force Fields. *J. Phys. Chem.* **1994**, *98* (45), 11623–11627. https://doi.org/10.1021/j100096a001.

(82) Becke, A. D. A New Mixing of Hartree–Fock and Local Density-Functional Theories. *J. Chem. Phys.* **1993**, *98* (2), 1372–1377. https://doi.org/10.1063/1.464304.

(83) Zhao, Y.; Truhlar, D. G. The M06 Suite of Density Functionals for Main Group Thermochemistry, Thermochemical Kinetics, Noncovalent Interactions, Excited States, and Transition Elements: Two New Functionals and Systematic Testing of Four M06-Class

Functionals and 12 Other Functionals. *Theor. Chem. Acc.* **2008**, *120* (1–3), 215–241. https://doi.org/10.1007/s00214-007-0310-x.

(84) Zhao, Y.; Schultz, N. E.; Truhlar, D. G. Exchange-Correlation Functional with Broad Accuracy for Metallic and Nonmetallic Compounds, Kinetics, and Noncovalent Interactions. *J. Chem. Phys.* **2005**, *123* (16), 161103. https://doi.org/10.1063/1.2126975.

(85) Zhao, Y.; Schultz, N. E.; Truhlar, D. G. Design of Density Functionals by Combining the Method of Constraint Satisfaction with Parametrization for Thermochemistry, Thermochemical Kinetics, and Noncovalent Interactions. *J. Chem. Theory Comput.* **2006**, *2* (2), 364–382. https://doi.org/10.1021/ct0502763.

(86) Zhao, Y.; Truhlar, D. G. Benchmark Data for Interactions in Zeolite Model Complexes and Their Use for Assessment and Validation of Electronic Structure Methods. *J. Phys. Chem. C* **2008**, *112* (17), 6860–6868. https://doi.org/10.1021/jp7112363.

(87) Paranthaman, S.; Sampathkumar, S.; Murugasenapathi, N. K. Density Functional Benchmark Studies on Structure and Energetics of 3d Transition Metal Mononitrides. *J. Chem. Sci.* **2018**, *130* (12), 164. https://doi.org/10.1007/s12039-018-1564-7.

(88) Jensen, F. *Introduction to Computational Chemistry*, Third edition.; John Wiley & Sons: Chichester, UK ; Hoboken, NJ, 2017.

(89) Grimme, S. Density Functional Theory with London Dispersion Corrections. *WIREs Comput. Mol. Sci.* **2011**, *1* (2), 211–228. https://doi.org/10.1002/wcms.30.

(90) Grimme, S.; Hansen, A. A Practicable Real-Space Measure and Visualization of Static Electron-Correlation Effects. *Angew. Chem. Int. Ed.* **2015**, *54* (42), 12308–12313. https://doi.org/10.1002/anie.201501887.

(91) Neese, F. The ORCA Program System. *WIREs Comput. Mol. Sci.* **2012**, *2* (1), 73–78. https://doi.org/10.1002/wcms.81.(92) Furche, F.; Ahlrichs, R.; Hättig, C.; Klopper, W.; Sierka, M.; Weigend, F. Turbomole. *WIREs Comput. Mol. Sci.* **2014**, *4* (2), 91–100. https://doi.org/10.1002/wcms.1162.

(93) Weigend, F.; Ahlrichs, R. Balanced Basis Sets of Split Valence, Triple Zeta Valence and Quadruple Zeta Valence Quality for H to Rn: Design and Assessment of Accuracy. *Phys. Chem. Chem. Phys.* **2005**, *7* (18), 3297. https://doi.org/10.1039/b508541a.

(94) Dinda, S.; Chiu, C.; Genest, A.; Rösch, N. Evaluation of Density Functionals for Elementary Steps of Selective Oxidation Reactions. *Comput. Theor. Chem.* **2017**, *1101*, 36–45. https://doi.org/10.1016/j.comptc.2016.12.021.

(95) Goncalves, T. J.; Plessow, P. N.; Studt, F. On the Accuracy of Density Functional Theory in Zeolite Catalysis. *ChemCatChem* **2019**, *11* (17), 4368–4376. https://doi.org/10.1002/cctc.201900791.

(96) Grimme, S.; Antony, J.; Ehrlich, S.; Krieg, H. A Consistent and Accurate *Ab Initio* Parametrization of Density Functional Dispersion Correction (DFT-D) for the 94 Elements H-Pu. *J. Chem. Phys.* **2010**, *132* (15), 154104. https://doi.org/10.1063/1.3382344.

(97) Okazaki, I.; Sato, F.; Yoshihiro, T.; Ueno, T.; Kashiwagi, H. Development of a Restricted Open Shell Kohn–Sham Program and Its Application to a Model Heme Complex. *J. Mol. Struct. THEOCHEM* **1998**, *451* (1–2), 109–119. https://doi.org/10.1016/S0166-1280(98)00164-X.

(98) Kresse, G.; Hafner, J. *Ab Initio* Molecular Dynamics for Liquid Metals. *Phys. Rev. B* **1993**, *47* (1), 558–561. https://doi.org/10.1103/PhysRevB.47.558.

(99) Kresse, G.; Furthmüller, J. Efficient Iterative Schemes for *Ab Initio* Total-Energy Calculations Using a Plane-Wave Basis Set. *Phys. Rev. B* **1996**, *54* (16), 11169–11186. https://doi.org/10.1103/PhysRevB.54.11169.

(100) Kresse, G.; Furthmüller, J. Efficiency of Ab-Initio Total Energy Calculations for Metals and Semiconductors Using a Plane-Wave Basis Set. *Comput. Mater. Sci.* **1996**, *6* (1), 15–50. https://doi.org/10.1016/0927-0256(96)00008-0.

(101) Staroverov, V. N.; Scuseria, G. E.; Tao, J.; Perdew, J. P. Comparative Assessment of a New Nonempirical Density Functional: Molecules and Hydrogen-Bonded Complexes. *J. Chem. Phys.* **2003**, *119* (23), 12129–12137. https://doi.org/10.1063/1.1626543.

(102) Schäfer, A.; Huber, C.; Ahlrichs, R. Fully Optimized Contracted Gaussian Basis Sets of Triple Zeta Valence Quality for Atoms Li to Kr. *J. Chem. Phys.* **1994**, *100* (8), 5829–5835. https://doi.org/10.1063/1.467146.

(103) Govindasamy, A.; Muthukumar, K.; Yu, J.; Xu, Y.; Guliants, V. V. Adsorption of Propane, Isopropyl, and Hydrogen on Cluster Models of the M1 Phase of Mo−V−Te−Nb−O Mixed Metal Oxide Catalyst. *J. Phys. Chem. C* **2010**, *114* (10), 4544–4549. https://doi.org/10.1021/jp910382x.

(104) Johnson, R. Computational Chemistry Comparison and Benchmark Database, NIST Standard Reference Database 101, 2002. https://doi.org/10.18434/T47C7Z.

(105) Brazdil, J. F. Strategies for the Selective Catalytic Oxidation of Alkanes. *Top. Catal.* **2006**, *38* (4), 289–294. https://doi.org/10.1007/s11244-006-0027-4.

(106) Li, X.; Teschner, D.; Streibel, V.; Lunkenbein, T.; Masliuk, L.; Fu, T.; Wang, Y.; Jones, T.; Seitz, F.; Girgsdies, F.; Rosowski, F.; Schlögl, R.; Trunschke, A. How to Control Selectivity in Alkane Oxidation? *Chem. Sci.* **2019**, *10* (8), 2429–2443. https://doi.org/10.1039/C8SC04641G.

(107) Faramawy, S.; Zaki, T.; Sakr, A. A.-E. Natural Gas Origin, Composition, and Processing: A Review. *J. Nat. Gas Sci. Eng.* **2016**, *34*, 34–54. https://doi.org/10.1016/j.jngse.2016.06.030.

(108) Wachs, I. E.; Routray, K. Catalysis Science of Bulk Mixed Oxides. *ACS Catal.* **2012**, *2* (6), 1235–1246. https://doi.org/10.1021/cs2005482.

(109) Sprenger, P.; Kleist, W.; Grunwaldt, J.-D. Recent Advances in Selective Propylene Oxidation over Bismuth Molybdate Based Catalysts: Synthetic, Spectroscopic, and Theoretical Approaches. *ACS Catal.* **2017**, *7* (9), 5628–5642. https://doi.org/10.1021/acscatal.7b01149.

(110) Deshlahra, P.; Carr, R. T.; Chai, S.-H.; Iglesia, E. Mechanistic Details and Reactivity Descriptors in Oxidation and Acid Catalysis of Methanol. *ACS Catal.* **2015**, *5* (2), 666–682. https://doi.org/10.1021/cs501599y.

(111) Andrushkevich, T. V.; Ovchinnikova, E. V. The Role of Water in Selective Heterogeneous Catalytic Oxidation of Hydrocarbons. *Mol. Catal.* **2020**, *484*, 110734. https://doi.org/10.1016/j.mcat.2019.110734.

(112) Grasselli, R. K.; Buttrey, D. J.; Burrington, J. D.; Andersson, A.; Holmberg, J.; Ueda, W.; Kubo, J.; Lugmair, C. G.; Volpe, A. F. Active Centers, Catalytic Behavior, Symbiosis and Redox Properties of MoV(Nb,Ta)TeO Ammoxidation Catalysts. *Top. Catal.* **2006**, *38* (1–3), 7–16. https://doi.org/10.1007/s11244-006-0066-x.

(113) Schlögl, R. Selective Oxidation: From a Still Immature Technology to the Roots of Catalysis Science. *Top. Catal.* **2016**, *59* (17–18), 1461–1476. https://doi.org/10.1007/s11244-016-0684-x.

(114) Sanfiz, A. C.; Hansen, T. W.; Teschner, D.; Schnörch, P.; Girgsdies, F.; Trunschke, A.; Schlögl, R.; Looi, M. H.; Hamid, S. B. A. Dynamics of the MoVTeNb Oxide M1 Phase in Propane Oxidation. *J. Phys. Chem. C* **2010**, *114* (4), 1912–1921. https://doi.org/10.1021/jp909352u.

(115) Fan, Y.; Li, S.; Liu, Y.; Wang, Y.; Wang, Y.; Chen, Y.; Yu, S. High-Pressure Hydrothermal Synthesis of MoVTeNbOx with High Surface V5+ Abundance for Oxidative Conversion of Propane to Acrylic Acid. *J. Supercrit. Fluids* **2022**, *181*, 105469. https://doi.org/10.1016/j.supflu.2021.105469.

(116) Shorayeva, K. A.; Massalimova, B. K.; Bespalko, Y. N.; Kovalev, E. P.; Ishchenko, A. V.; Sadykov, V. A. Synthesis, Properties, and Activity of MoVTeNbO Catalysts Modified by Zirconia-Pillared Clays in Oxidative Dehydrogenation of Ethane. *Open Chem.* **2021**, *19* (1), 492–502. https://doi.org/10.1515/chem-2021-0048.

(117) Duprez, D.; Cavani, F. *Handbook of Advanced Methods and Processes in Oxidation Catalysis: From Laboratory to Industry*; IMPERIAL COLLEGE PRESS, 2014. https://doi.org/10.1142/p791.

(118) Amakawa, K.; Kolen'ko, Y. V.; Villa, A.; Schuster, M. E.; Csepei, L.-I.; Weinberg, G.; Wrabetz, S.; Naumann d'Alnoncourt, R.; Girgsdies, F.; Prati, L.; Schlögl, R.; Trunschke, A. Multifunctionality of Crystalline MoV(TeNb) M1 Oxide Catalysts in Selective Oxidation of Propane and Benzyl Alcohol. *ACS Catal.* **2013**, *3* (6), 1103–1113. https://doi.org/10.1021/cs400010q.

(119) Donaubauer, P. J.; Melzer, D. M.; Wanninger, K.; Mestl, G.; Sanchez-Sanchez, M.; Lercher, J. A.; Hinrichsen, O. Intrinsic Kinetic Model for Oxidative Dehydrogenation of Ethane over MoVTeNb Mixed Metal Oxides: A Mechanistic Approach. *Chem. Eng. J.* **2020**, *383*, 123195. https://doi.org/10.1016/j.cej.2019.123195.

(120) Busch, M.; Fabrizio, A.; Luber, S.; Hutter, J.; Corminboeuf, C. Exploring the Limitation of Molecular Water Oxidation Catalysts. *J. Phys. Chem. C* **2018**, *122* (23), 12404–12412. https://doi.org/10.1021/acs.jpcc.8b03935.

(121) Miyajima, M.; Watanabe, Y.; Nakano, H. Relativistic Quasidegenerate Perturbation Theory with Four-Component General Multiconfiguration Reference Functions. *J. Chem. Phys.* **2006**, *124* (4), 044101. https://doi.org/10.1063/1.2161182.

(122) Nakano, H.; Uchiyama, R.; Hirao, K. Quasi-degenerate Perturbation Theory with *General* Multiconfiguration Self-consistent Field Reference Functions. *J. Comput. Chem.* **2002**, *23* (12), 1166–1175. https://doi.org/10.1002/jcc.10050.

(123) Alexopoulos, K.; Reyniers, M.-F.; Marin, G. B. Reaction Path Analysis of Propane Selective Oxidation over V2O5 and V2O5/TiO2. *J. Catal.* **2012**, *289*, 127–139. https://doi.org/10.1016/j.jcat.2012.01.019.

(124) Kozuch, S.; Shaik, S. How to Conceptualize Catalytic Cycles? The Energetic Span Model. *Acc. Chem. Res.* **2011**, *44* (2), 101–110. https://doi.org/10.1021/ar1000956.

(125) Vitry, D. Mo-V-Te-(Nb)-O Mixed Metal Oxides Prepared by Hydrothermal Synthesis for Catalytic Selective Oxidations of Propane and Propene to Acrylic Acid. *Appl. Catal. Gen.* **2003**, *251* (2), 411–424. https://doi.org/10.1016/S0926-860X(03)00381-8.

(126) Trunschke, A.; Bellini, G.; Boniface, M.; Carey, S. J.; Dong, J.; Erdem, E.; Foppa, L.; Frandsen, W.; Geske, M.; Ghiringhelli, L. M.; Girgsdies, F.; Hanna, R.; Hashagen, M.; Hävecker, M.; Huff, G.; Knop-Gericke, A.; Koch, G.; Kraus, P.; Kröhnert, J.; Kube, P.; Lohr, S.; Lunkenbein, T.; Masliuk, L.; Naumann d'Alnoncourt, R.; Omojola, T.; Pratsch, C.; Richter, S.; Rohner, C.; Rosowski, F.; Rüther, F.; Scheffler, M.; Schlögl, R.; Tarasov, A.; Teschner, D.; Timpe, O.; Trunschke, P.; Wang, Y.; Wrabetz, S. Towards Experimental Handbooks in Catalysis. *Top. Catal.* **2020**, *63* (19–20), 1683–1699. https://doi.org/10.1007/s11244-020-01380-2.

(127) Botella, P.; López Nieto, J. M.; Solsona, B.; Mifsud, A.; Márquez, F. The Preparation, Characterization, and Catalytic Behavior of MoVTeNbO Catalysts Prepared by Hydrothermal Synthesis. *J. Catal.* **2002**, *209* (2), 445–455. https://doi.org/10.1006/jcat.2002.3648.

(128) Sen, K.; Schäfer, A.; Rosowski, F.; Sharapa, D. I.; Studt, F. Quantum Chemical Modeling of the Full Catalytic Cycle for Selective Oxidation of Propane to Propene on the M1 Phase of Mo–Te–Nb–O Mixed-Metal Oxide Catalysts. *J. Phys. Chem. C* **2024**, *128* (34), 14273–14281. https://doi.org/10.1021/acs.jpcc.4c02899.

(129) Deshlahra, P.; Iglesia, E. Toward More Complete Descriptors of Reactivity in Catalysis by Solid Acids. *ACS Catal.* **2016**, *6* (8), 5386–5392. https://doi.org/10.1021/acscatal.6b01402.

Appendixes

A. Different surface configurations of active site

ID	Surface	ID	Surface
2a	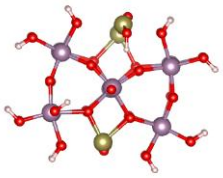	3e	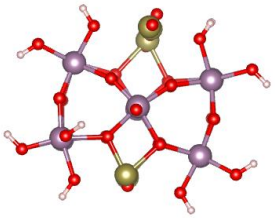
2b	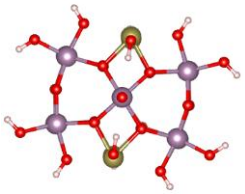	3f	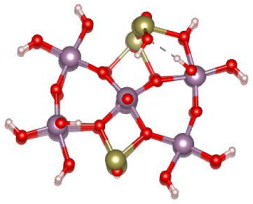
2c	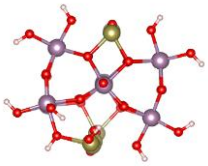	4a	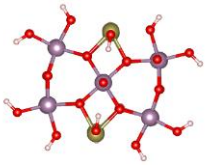
3a	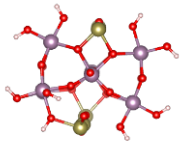	4b	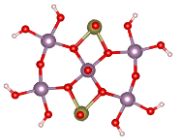
3b	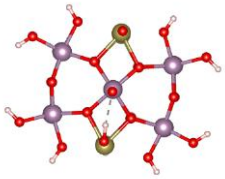	4c	
3c	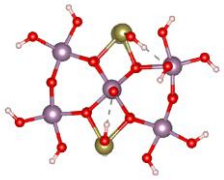	4d	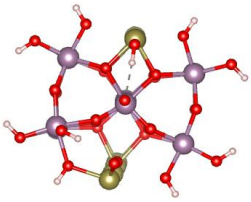

3d	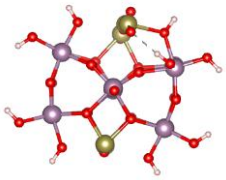		
4e	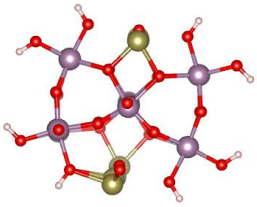	6a	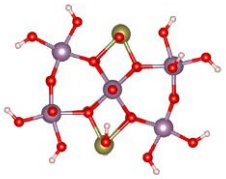
4f	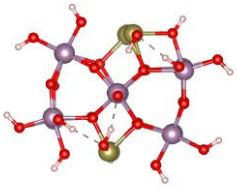	6b	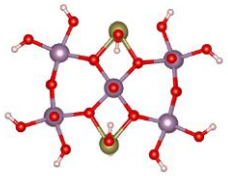
4g	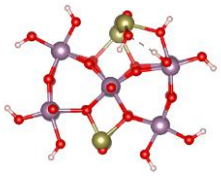	6c	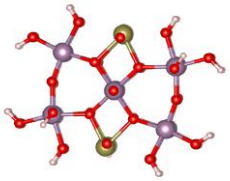
5a	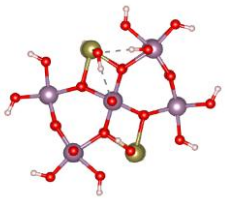	6d	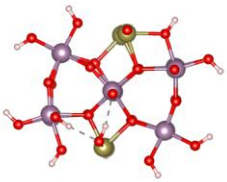
5b	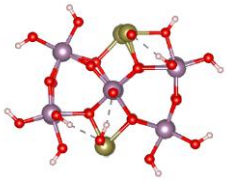	6e	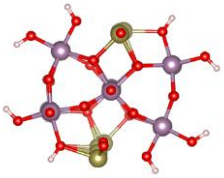
5c	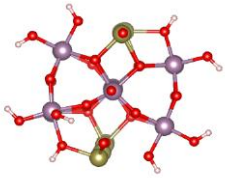	6f	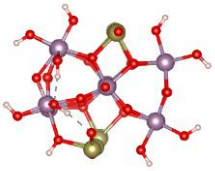

*Table AT1. All the surface structures with their ID. Digits in the id represents the SOX number and the alphabets are given according to energetic ranking, e.g., structure **3c** has SOX 3 and it is the 3rd stable surface compared to **3a**. xyz files of these structures are also provided as a separate zip file.*

B. Raw energetics from DFT Calculations

- **Ground state structures with Mo-Only:**

id	PBE-D3 (Hartree)	M06-D3 (Hartree)	ZPE (Hartree)	S (kJ/mol/K) T=298K	S (kJ/mol/K) T=400K
2a	-9992.603140	-10003.135250	0.619028	2.8228	3.6037
2b	-9992.565935	-10003.113920	0.616219	2.8371	3.6037
2c	-9992.604996	-10003.054210	0.624359	2.7832	3.5568
3a	-9991.991649	-10002.512770	0.611145	2.7907	3.5456
3b	-9991.948761	-10002.503018	0.606108	2.8423	3.5985
3c	-10068.288087	-10078.961216	0.630972	2.8245	3.6037
3d	-9991.969332	-10002.512770	0.611145	2.7907	3.5457
3e	-9991.963474	-10002.503170	0.606108	2.8423	3.5985
3f	-10068.317478	-10078.944896	0.630972	2.8245	3.5965
4a	-10067.663479	-10078.351460	0.619029	2.7930	3.5812
4b	-9991.321976	-10001.871700	0.594716	2.8120	3.5725
4c	-10067.661539	-10078.275920	0.624563	2.7507	3.6199
4d	-10067.697652	-10078.254530	0.623302	2.7871	3.5568
4e	-9991.388664	-10001.884004	0.601584	2.7327	3.4705
4f	-10144.016014	-10154.764971	0.644762	2.8552	3.6256
4g	-10067.697756	-10078.32305	0.620376	2.8496	3.5721
5a	-10143.370554	-10154.157396	0.633713	2.8067	3.5213
5b	-10143.370405	-10154.155640	0.635671	2.7970	3.5592
5c	-10067.055325	-10077.685994	0.606621	2.8134	3.5789
6a	-10142.737344	-10153.518784	0.621357	2.7836	3.5428
6b	-10142.742533	-10153.521051	0.622056	2.7419	3.4813
6c	-10142.736898	-10153.510265	0.623340	2.8039	3.5686
6d	-10142.739372	-10153.518784	0.621357	2.7836	3.5726
6e	-10066.421934	-10077.047677	0.597969	2.7766	3.5306
6f	-10142.757033	-10153.489840	0.625094	2.8224	3.5855
C_3H_5* + 5a	-10260.456881	-10271.445018	0.703948	2.8493	3.6984
C_3H_5* + 4a	-10184.749942	-10195.615609	0.690221	2.9337	3.7236
C_3H_5* + 3a	-10109.069686	-10119.771022	0.680194	2.8419	3.6591
C_3H_4O* + 5a	-10334.406106	-10345.511204	0.686742	2.9526	3.7019
C_3H_4O* + 4a	-10258.699728	-10269.686545	0.672861	2.9247	3.7019
C_3H_4O* + 3a	-10183.014439	-10193.838842	0.662895	2.8711	3.6996
C_3H_7* + 5a	-10261.684800	-10272.671763	0.726804	2.9052	3.5985
C_3H_7* + 4a	-10185.995591	-10196.835893	0.713534	2.9312	3.7254
C_3H_7* + 3a	-10110.298592	-10121.009474	0.702900	2.8806	3.6143

Table AT2. Calculated energies (M06-D3, PBE-D3), ZPE and entropy, dispersion correction of all the surface structures with their IDs.

○ V containing ground state structures:

sid	Source	Vanadium	Unpaired electrons	Energy (M06-D3) (Hartree)	ZPE (Hartree)	S (298K) (kJ/mol/K)
6c	1V1V	2	4	-11905.03773	0.622176	2.79786
3b	1V1V	2	3	-11754.05633	0.605501	2.77443
4f	1V1V	2	4	-11906.26202	0.641666	2.79027
4b	1V1V	2	4	-11753.39133	0.590272	2.75653
4d	1V1V	2	4	-11829.84492	0.619684	2.75816
4e	1V1V	2	4	-11753.37239	0.596212	2.79403
4c	1V1V	2	4	-11829.88057	0.618694	2.71482
4g	1V1V	2	4	-11829.81854	0.619451	2.78294
4a	1V1V	2	4	-11829.9111	0.620078	2.76667
6a	1V1V	2	4	-11905.07189	0.619933	2.74463
3d	1V1V	2	3	-11753.99518	0.605484	2.74665
3f	1V1V	2	3	-11754.04633	0.60562	2.77284
3g	1V1V	2	3	-11830.46282	0.630405	2.75772
2a	1V1V	2	4	-11754.63551	0.615269	2.77547
2b	1V1V	2	4	-11754.72271	0.620107	2.81294
2c	1V1V	2	4	-11754.62692	0.617705	2.74065
3c	1V1V	2	4	-11830.46282	0.630405	2.75772
6b	1V1V	2	4	-11905.0987	0.622145	2.71590
6d	1V1V	2	4	-11905.11541	0.621834	2.71134
6f	1V1V	2	4	-11904.99227	0.620131	2.87398
6e	1V1V	2	4	-11828.50311	0.593842	2.76856
5b	1V1V	2	3	-11905.69921	0.634423	2.72864
5a	1V1V	2	3	-11905.72659	0.633462	2.78070
3g	1V1V	2	3	-11830.46282	0.630405	2.75772
6c	3V1V	4	2	-13656.56609	0.617636	2.76989
5c	3V1V	4	2	-13580.76166	0.60867	2.75597
4f	3V1V	4	2	-13657.78891	0.639634	2.76483
4b	3V1V	4	2	-13504.91677	0.585147	2.72027
4d	3V1V	4	2	-13581.3298	0.614766	2.74492
4e	3V1V	4	2	-13504.89391	0.591952	2.71538
4c	3V1V	4	2	-13581.39982	0.614202	2.72826
4g	3V1V	4	2	-13581.37581	0.614663	2.68759
3d	3V1V	4	2	-13505.57447	0.602784	2.73730
6a	3V1V	4	2	-13656.57732	0.615189	2.72003
3f	3V1V	4	2	-13505.5779	0.600789	2.74418
3a	3V1V	4	2	-13505.53997	0.603081	2.72143
3g	3V1V	4	2	-13582.00676	0.625628	2.75140
2a	3V1V	4	2	-13506.16279	0.61007	2.76465
2b	3V1V	4	2	-13506.24048	0.611602	2.70703
2c	3V1V	4	2	-13506.1633	0.613327	2.73454
3c	3V1V	4	2	-13582.05975	0.626286	2.74199

6b	3V1V	4	2	-13656.58098	0.614259	2.65484
6d	3V1V	4	2	-13656.62693	0.616159	2.68115
6f	3V1V	4	2	-13656.50097	0.62216	2.76494
6e	3V1V	4	2	-13580.0202	0.592583	2.75656
5a	3V1V	4	2	-13657.23704	0.627154	2.68322
6c	3V2V	5	2	-14532.3015	0.613906	2.73129
5c	3V2V	5	2	-14456.5171	0.60584	2.77591
4f	3V2V	5	2	-14533.59438	0.636536	2.71219
4b	3V2V	5	2	-14380.6604	0.585084	2.74073
4d	3V2V	5	2	-14457.08626	0.612497	2.75164
4e	3V2V	5	2	-14380.68714	0.588917	2.71814
4c	3V2V	5	2	-14457.14933	0.608893	2.71692
4g	3V2V	5	2	-14457.15505	0.61375	2.72852
3d	3V2V	5	2	-14381.35315	0.601245	2.76299
6a	3V2V	5	2	-14532.30914	0.613256	2.72106
3f	3V2V	5	2	-14381.40754	0.601742	2.78562
3a	3V2V	5	2	-14381.35425	0.599118	2.68640
3g	3V2V	5	2	-14457.83967	0.624085	2.71544
2a	3V2V	5	2	-14382.02449	0.611282	2.71723
2b	3V2V	5	2	-14381.9955	0.610734	2.70588
2c	3V2V	5	2	-14381.98877	0.610205	2.73523
3c	3V2V	5	2	-14457.8144	0.623086	2.71920
6b	3V2V	5	2	-14532.30968	0.611739	2.63802
6d	3V2V	5	2	-14532.35862	0.61264	2.69621
6f	3V2V	5	2	-14532.29073	0.619785	2.73743
6e	3V2V	5	2	-14455.76647	0.588756	2.73837
5a	3V2V	5	2	-14532.96841	0.625574	2.68959
6c	3V3V	6	2	-15408.03076	0.611839	2.74691
5c	3V3V	6	2	-15332.24856	0.602237	2.73877
4f	3V3V	6	2	-15409.36029	0.6336	2.69716
4b	3V3V	6	2	-15256.39534	0.581964	2.70765
4d	3V3V	6	2	-15332.87339	0.610648	2.72902
4e	3V3V	6	2	-15256.43774	0.588014	2.67776
4c	3V3V	6	2	-15332.88031	0.608942	2.72575
4g	3V3V	6	2	-15332.88874	0.611138	2.71977
4a	3V3V	6	2	-15332.89746	0.609103	2.70468
3d	3V3V	6	2	-15257.10839	0.598333	2.71924
6a	3V3V	6	2	-15408.03748	0.609749	2.70287
3f	3V3V	6	2	-15257.1565	0.598837	2.71433
3b	3V3V	6	2	-15257.06942	0.59567	2.71957
3a	3V3V	6	2	-15257.03719	0.59815	2.71650
3g	3V3V	6	2	-15333.5768	0.621587	2.71591
2a	3V3V	6	2	-15257.77772	0.608908	2.71117
2b	3V3V	6	2	-15257.75237	0.608269	2.68482
2c	3V3V	6	2	-15257.7335	0.608513	2.69934
3c	3V3V	6	2	-15333.54555	0.621105	2.70128
6b	3V3V	6	2	-15408.03458	0.609374	2.68512

6d	3V3V	6	2	-15408.09461	0.613054	2.69861
6f	3V3V	6	2	-15408.09192	0.618379	2.77911
6e	3V3V	6	2	-15331.50555	0.588678	2.72305
5b	3V3V	6	2	-15408.70092	0.622507	2.72312
5a	3V3V	6	2	-15408.69978	0.621174	2.66390
6c	1V0V	4	1	-11029.26146	0.622022	2.80495
6d	1V0V	4	5	-11029.28599	0.620584	2.75901
6b	1V0V	4	5	-11029.32055	0.621942	2.78387
4c	1V0V	4	3	-10954.10943	0.619997	2.82154
2a	1V0V	4	5	-10878.88688	0.617243	2.85542
4f	1V0V	4	1	-11030.51287	0.643944	2.79695
6a	1V0V	4	3	-11029.29812	0.620292	2.77275
3g	1V0V	3	4	-10954.70868	0.632334	2.78615
4a	1V0V	4	5	-10954.12523	0.619988	2.79518
3f	1V0V	3	0	-10878.29824	0.608583	2.74843
5b	1V0V	3	0	-11029.94414	0.634333	2.76660
3b	1V0V	3	2	-10878.29582	0.606995	2.80844
6e	1V0V	4	3	-10952.76494	0.594406	2.83461
2c	1V0V	4	3	-10878.88546	0.619859	2.79893
6f	1V0V	4	1	-11029.24085	0.621682	2.82357
4e	1V0V	4	1	-10877.61669	0.597393	2.78216
5a	1V0V	3	4	-11029.94253	0.632907	2.77255
4g	1V0V	4	5	-10954.07325	0.619816	2.78031
2b	1V0V	4	1	-10878.94514	0.619737	2.81082
3d	1V0V	3	0	-10878.24738	0.607019	2.77359
4d	1V0V	4	3	-10954.05597	0.620517	2.80971
4b	1V0V	4	3	-10877.62029	0.592349	2.81762
3c	1V0V	3	4	-10954.70868	0.632334	2.78615
4g	3V0V	2	5	-12705.61309	0.617037	2.79182
6d	3V0V	2	5	-12780.87799	0.617008	2.73944
2a	3V0V	2	5	-12630.40889	0.611989	2.73993
6a	3V0V	2	5	-12780.8222	0.616979	2.74153
4f	3V0V	2	5	-12782.04252	0.640698	2.77433
4d	3V0V	2	5	-12705.58648	0.617268	2.79342
4b	3V0V	2	3	-12629.14092	0.588097	2.77077
6f	3V0V	2	3	-12780.78785	0.625858	2.77061
3c	3V0V	2	2	-12706.28529	0.627091	2.77332
2c	3V0V	2	3	-12630.41122	0.614826	2.77454
5c	3V0V	2	4	-12704.94086	0.606093	2.78083
6c	3V0V	2	1	-12780.78506	0.616914	2.77139
3g	3V0V	2	4	-12706.25796	0.626787	2.79137
4a	3V0V	2	3	-12705.66327	0.614007	2.75949
4c	3V0V	2	5	-12705.62702	0.614102	2.72797
4e	3V0V	2	1	-12629.14961	0.592995	2.71668
6e	3V0V	2	3	-12704.28453	0.59326	2.75504
3d	3V0V	2	2	-12629.83033	0.604535	2.80435
6b	3V0V	2	3	-12780.83524	0.615203	2.65578

3f	3V0V	2	4	-12629.83088	0.602774	2.78580
2b	3V0V	2	5	-12630.45781	0.614109	2.78186
5b	3V0V	2	2	-12781.44878	0.629295	2.74280
5a	3V0V	2	4	-12781.4849	0.628257	2.68933
3b	3V0V	2	2	-12629.80948	0.600591	2.73646
3a	3V0V	2	4	-12629.79456	0.603806	2.74207
4a	3V1V	4	2	-13581.43713	0.61506	2.70054
3b	3V1V	4	2	-13505.57913	0.598684	2.74669
5b	3V1V	4	2	-13657.23085	0.628563	2.75887
4a	3V2V	5	2	-14457.16721	0.611086	2.67392
3b	3V2V	5	2	-14381.33766	0.596887	2.74592
5b	3V2V	5	2	-14532.96822	0.624377	2.73486

Table AT3. Calculated energies (M06-D3), ZPE and entropy, dispersion correction of all the surface structures with their IDs for V containing active sites.

- **Transition state structures:**

Correspondence to Figure S2 or S3	Gas species	Surface-Id	PBE-D3 (Hartree)	M06-D3 (Hartree)	ZPE (Hartree)	Entropy (400K) (kJ/mol/K)
S2-(a)	Propane-C2	6b	-10270.328455	-10272.570509	0.714890	0.1742
S2-(b)	Propane-C2	6a	-10270.332311	-10272.558586	0.718256	0.1945
S2-(c)	Propane-C2	4g	-10195.193208	-10197.357277	0.716045	0.1417
S2-(d)	Propane-C2	4a	-10195.157995	-10197.380625	0.714499	0.1335
S2-(e)	Propane-C1	6b	-10261.579255	-10272.560736	0.716389	0.1237
S2-(f)	Propane-C1	4g	-8106.266224	-10197.353938	0.716567	0.1355
S2-(g)	Propyl	5a	-10261.570671	-10272.557101	0.718951	0.1666
S2-(h)	Propyl	5b	-10261.602140	-10272.563699	0.718994	0.1363
S2-(i)	Propyl	5a	-10261.634856	-10272.561655	0.718083	0.1800
S3-(a)	Propene-allyl	6c	-10260.387966	-10271.348105	0.693102	0.0948
S3-(b)	Propene-allyl	4g	-10185.327101	-10196.137318	0.693924	0.1394
S3-(c)	Allylalcohol-C1	6c	-10335.501202	-10346.586236	0.699390	0.1259
S3-(d)	Allylalcohol-C1	4g	-10260.411862	-10271.374497	0.698984	0.1299

Table AT4. Calculated energies (M06, PBE-D3) ZPE and entropy, dispersion correction of all the gas molecules used for this work

- **Molecules in gas phase:**

Molecule	PBE-D3 (Hartree)	M06-D3 (Hartree)	ZPE (Hartree)	S (298K) (kJ/mol/K)	S (400K) (kJ/mol/K)
water	-76.380182	-76.426460	0.02121	0.1890	0.1989
oxygen	-150.248730	-150.313940	0.00369	0.1961	0.2048
hydrogen	-1.166102	-1.173870	0.01012	0.1305	0.1390
propane	-119.005972	-119.082269	0.10296	0.2690	0.2929
2-propyl	-118.345242	-118.418220	0.08765	0.2876	0.3118
1-propyl	-118.338390	-118.411150	0.08779	0.29214	0.3168
propene	-117.780172	-117.849800	0.07771	0.26400	0.2858

propene-3-yl, allyl	-117.137146	-117.202790	0.06582	0.25237	0.2902
Allylalcohol	-192.955681	-193.064230	0.08471	0.30816	0.3348
2-propene-1-ol-1-yl	-192.330035	-192.433239	0.07110	0.29204	0.3195
Acrolein	-191.757562	-191.860631	0.06101	0.28025	0.3030
2-propenal-1-yl (sigma radical)	-191.110422	-191.207070	0.04871	0.28507	0.2996
2-propenal-1-yl (pi radical)	-191.116522	-191.216397	0.04699	0.27880	0.3035
Acrylic acid	-266.977253	-267.121125	0.06693	0.30581	0.3321
Isopropanol	-194.187954	-194.304250	0.10724	0.30871	0.3381

Table AT5. Calculated energies (M06, PBE-D3) ZPE and entropy, dispersion correction of all the gas molecules used for this work.

C. Transition states for Linear Scaling Model

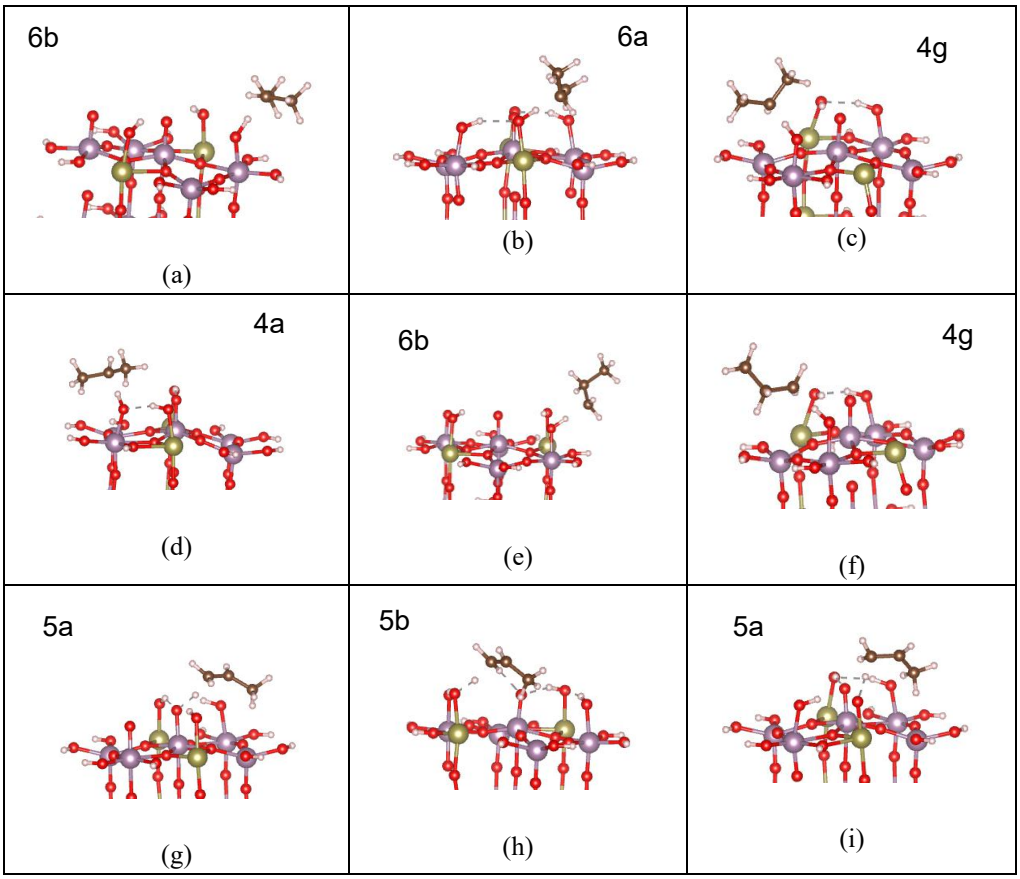

Figure AF1. DFT calculated transition state structures of CH activation of propane at C2 position (a, b, c, d), at C1 position (e, f) and propyl (g, h, i) activation on C2 cluster at different metal sites within different environment. IDs of the corresponding educt surfaces are given on top of each picture

Correspondence to Figure S2	Gas molecule	id	Metal-site	E_H (kJ/mol)	ΔE_{TS} (kJ/mol)	ΔH_{TS} (kJ/mol)	ΔS_{TS} (400 K) (kJ/mol)
(a)	Propane-c2	6b	Mo-O	-151	86	63	-57
(b)	Propane-c2	6a	Te-O	-146	89	68	-64
(c)	Propane-c2	4g	Mo-O	-106	126	104	-78
(d)	Propane-c2	4a	Mo-O	-96	108	88	-85
(e)	Propane-c1	6b	Mo-O	-151	111	89	-70
(f)	Propane-c1	4g	Mo-O	-96	142	115	-80
(g)	Propyl	5a	Mo-O	16	65	58	-77
(h)	Propyl	5b	Te-O	-58	32	18	-70
							Average = -72.6

Table AT6. Energy, enthalpy, entropy data for all the DFT calculated with transition states along with the corresponding E_H

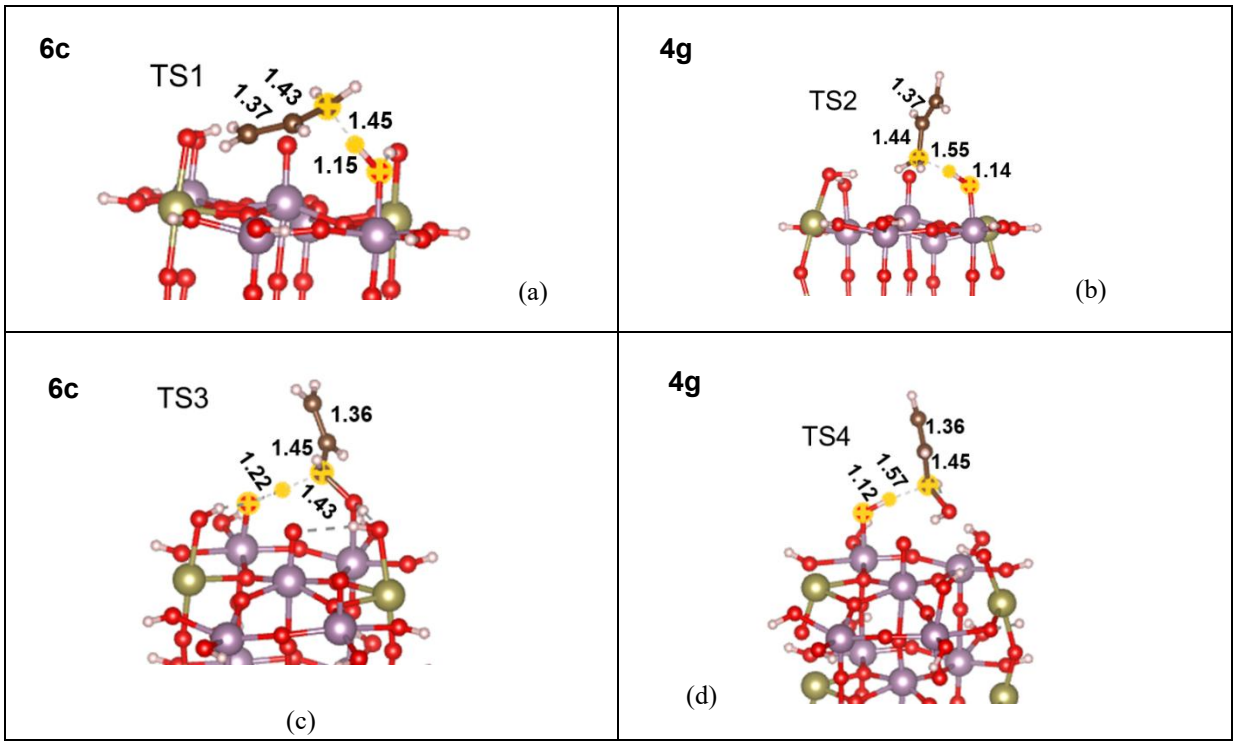

Figure AF2. DFT calculated transition state structures of CH activation of propene at allyl carbon (a, b), and allyl alcohol (c, d) activation on C2 cluster at different metal sites on surface 6c and 4g.

Correspondence to Figure S3	Gas molecule	id	Metal-site	E_H (kJ/mol)	ΔE_{TS} (kJ/mol)	ΔH_{TS} (kJ/mol)	ΔS_{TS} (400 K) (kJ/mol)
(a)	Propene-allyl C	6b	Mo-O	-151	60	38	-91
(b)	Propene-allyl C	4g	Mo-O	-96	93	76	-77
(c)	Allyl alcohol – c1	6b	Mo-O	-151	-2	-21	-99
(d)	Allyl alcohol – c2	4g	Mo-O	-96	34	15	-98
							Average = -92

Table AT7. Energy, enthalpy, entropy data for all the DFT calculated with transition states of propene and allyl alcohol along with the corresponding E_H

D. Different descriptor values for Mo-Only and V containing active sites.

Structure	Path of Oxidation_ Hydrogenation	sid_1	tid_1	E_{ox} (kJ/mol)	sid_2	tid_2	E_H (kJ/mol)	$E_{propane\text{-}TS}$ (kJ/mol)	$E_{propyl\text{-}TS}$ (kJ/mol)	Color
1V1V	2b_4a_4a_3c	2b	4a	-82	4a	3c	92	316	191	red
1V1V	2a_4d_4d_3c	2a	4d	-138	4d	3c	-81	186	61	red
1V1V	2c_4c_4c_3c	2c	4c	-254	4c	3c	12	256	131	red
1V1V	3c_5a_5a_4f	3c	5a	-280	5a	4f	135	348	223	red
1V1V	4a_6b_6b_5a	4a	6b	-80	6b	5a	-108	166	41	red
1V1V	4c_6d_6d_5b	4c	6d	-204	6d	5b	8	253	128	red
1V1V	4g_6d_6d_5b	4g	6d	-367	6d	5b	8	253	128	red
1V1V	4d_6a_6a_5a	4d	6a	-184	6a	5a	-178	114	-11	red
3V0V	2b_4a_4a_3c	2b	4a	-127	4a	3c	-92	178	53	blue
3V0V	2b_4a_4a_3c	2b	4a	-127	4a	3c	-92	178	53	blue
3V0V	2b_4a_4a_3c	2b	4a	-127	4a	3c	-92	178	53	blue
3V0V	2b_4a_4a_3c	2b	4a	-127	4a	3c	-92	178	53	blue
3V0V	2a_4d_4d_3c	2a	4d	-54	4d	3c	-294	27	-98	blue
3V0V	2a_4d_4d_3c	2a	4d	-54	4d	3c	-294	27	-98	blue
3V0V	2a_4d_4d_3c	2a	4d	-54	4d	3c	-294	27	-98	blue
3V0V	2a_4d_4d_3c	2a	4d	-54	4d	3c	-294	27	-98	blue
3V0V	2c_4c_4c_3c	2c	4c	-154	4c	3c	-187	107	-18	blue
3V0V	2c_4c_4c_3c	2c	4c	-154	4c	3c	-187	107	-18	blue
3V0V	2c_4c_4c_3c	2c	4c	-154	4c	3c	-187	107	-18	blue
3V0V	2c_4c_4c_3c	2c	4c	-154	4c	3c	-187	107	-18	blue
3V0V	3c_5a_5a_4f	3c	5a	-112	5a	4f	77	305	180	blue
3V0V	3c_5a_5a_4f	3c	5a	-112	5a	4f	77	305	180	blue
3V0V	3c_5a_5a_4f	3c	5a	-112	5a	4f	77	305	180	blue
3V0V	3c_5a_5a_4f	3c	5a	-112	5a	4f	77	305	180	blue
3V0V	4a_6b_6b_5a	4a	6b	-39	6b	5a	-165	123	-2	blue
3V0V	4a_6b_6b_5a	4a	6b	-39	6b	5a	-165	123	-2	blue
3V0V	4a_6b_6b_5a	4a	6b	-39	6b	5a	-165	123	-2	blue
3V0V	4a_6b_6b_5a	4a	6b	-39	6b	5a	-165	123	-2	blue
3V0V	4c_6d_6d_5b	4c	6d	-247	6d	5b	42	279	154	blue
3V0V	4c_6d_6d_5b	4c	6d	-247	6d	5b	42	279	154	blue
3V0V	4g_6d_6d_5b	4g	6d	-283	6d	5b	42	279	154	blue
3V0V	4g_6d_6d_5b	4g	6d	-283	6d	5b	42	279	154	blue
3V0V	4c_6d_6d_5b	4c	6d	-247	6d	5b	42	279	154	blue
3V0V	4c_6d_6d_5b	4c	6d	-247	6d	5b	42	279	154	blue
3V0V	4g_6d_6d_5b	4g	6d	-283	6d	5b	42	279	154	blue
3V0V	4g_6d_6d_5b	4g	6d	-283	6d	5b	42	279	154	blue
3V0V	4d_6a_6a_5a	4d	6a	-207	6a	5a	-199	98	-27	blue
3V0V	4d_6a_6a_5a	4d	6a	-207	6a	5a	-199	98	-27	blue
3V0V	4d_6a_6a_5a	4d	6a	-207	6a	5a	-199	98	-27	blue
3V0V	4d_6a_6a_5a	4d	6a	-207	6a	5a	-199	98	-27	blue

3V0V	4e_6e_6e_5c	4e	6e	58	6e	5c	-182	110	-15	blue
3V0V	4e_6e_6e_5c	4e	6e	58	6e	5c	-182	110	-15	blue
3V0V	4e_6e_6e_5c	4e	6e	58	6e	5c	-182	110	-15	blue
3V0V	4e_6e_6e_5c	4e	6e	58	6e	5c	-182	110	-15	blue
3V1V	2b_4a_4a_3c	2b	4a	-104	4a	3c	-94	177	52	purple
3V1V	2a_4d_4d_3c	2a	4d	-26	4d	3c	-375	-35	-160	purple
3V1V	2c_4c_4c_3c	2c	4c	-209	4c	3c	-192	103	-22	purple
3V1V	3c_5a_5a_4f	3c	5a	-53	5a	4f	92	316	191	purple
3V1V	4a_6b_6b_5a	4a	6b	34	6b	5a	-181	111	-14	purple
3V1V	4c_6d_6d_5b	4c	6d	-184	6d	5b	-45	214	89	purple
3V1V	4g_6d_6d_5b	4g	6d	-247	6d	5b	-45	214	89	purple
3V1V	4d_6a_6a_5a	4d	6a	-238	6a	5a	-191	104	-21	purple
3V1V	4e_6e_6e_5c	4e	6e	81	6e	5c	-406	-57	-182	purple
3V2V	2b_4a_4a_3c	2b	4a	-39	4a	3c	-158	128	3	green
3V2V	2a_4d_4d_3c	2a	4d	250	4d	3c	-371	-31	-156	green
3V2V	2c_4c_4c_3c	2c	4c	-9	4c	3c	-205	93	-32	green
3V2V	3c_5a_5a_4f	3c	5a	8	5a	4f	-102	170	45	green
3V2V	4a_6b_6b_5a	4a	6b	38	6b	5a	-188	106	-19	green
3V2V	4c_6d_6d_5b	4c	6d	-137	6d	5b	-60	202	77	green
3V2V	4g_6d_6d_5b	4g	6d	-122	6d	5b	-60	202	77	green
3V2V	4d_6a_6a_5a	4d	6a	-173	6a	5a	-190	105	-20	green
3V2V	4e_6e_6e_5c	4e	6e	204	6e	5c	-430	-75	-200	green
3V3V	2b_4a_4a_3c	2b	4a	31	4a	3c	-161	127	2	black
3V3V	2a_4d_4d_3c	2a	4d	161	4d	3c	-224	79	-46	black
3V3V	2c_4c_4c_3c	2c	4c	27	4c	3c	-206	93	-32	black
3V3V	3c_5a_5a_4f	3c	5a	7	5a	4f	-193	102	-23	black
3V3V	4a_6b_6b_5a	4a	6b	52	6b	5a	-205	93	-32	black
3V3V	4c_6d_6d_5b	4c	6d	-151	6d	5b	-51	209	84	black
3V3V	4g_6d_6d_5b	4g	6d	-128	6d	5b	-51	209	84	black
3V3V	4d_6a_6a_5a	4d	6a	-19	6a	5a	-198	99	-26	black
3V3V	4e_6e_6e_5c	4e	6e	234	6e	5c	-410	-60	-185	black
Mo	2b_4a_4a_3c	2b	4a	-181	4a	3c	-90	179	54	magenta
Mo	2a_4d_4d_3c	2a	4d	99	4d	3c	-314	11	-114	magenta
Mo	2c_4c_4c_3c	2c	4c	-170	4c	3c	-258	53	-72	magenta
Mo	3c_5a_5a_4f	3c	5a	-103	5a	4f	-54	206	81	magenta
Mo	4a_6b_6b_5a	4a	6b	-64	6b	5a	-130	150	25	magenta
Mo	4c_6d_6d_5b	4c	6d	-197	6d	5b	-160	127	2	magenta
Mo	4g_6d_6d_5b	4g	6d	-58	6d	5b	-160	127	2	magenta
Mo	4d_6a_6a_5a	4d	6a	-282	6a	5a	-136	145	20	magenta
Mo	4e_6e_6e_5c	4e	6e	-18	6e	5c	-135	146	21	magenta
1V0V	2b_4a_4a_3c	2b	4a	-77	4a	3c	-127	152	27	yellow
1V0V	2a_4d_4d_3c	2a	4d	-36	4d	3c	-173	117	-8	yellow
1V0V	2c_4c_4c_3c	2c	4c	0	4c	3c	0	247	122	yellow
1V0V	3c_5a_5a_4f	3c	5a	-202	5a	4f	44	280	155	yellow
1V0V	4a_6b_6b_5a	4a	6b	-237	6b	5a	-92	178	53	yellow
1V0V	4c_6d_6d_5b	4c	6d	0	6d	5b	-187	107	-18	yellow
1V0V	4g_6d_6d_5b	4g	6d	-51	6d	5b	-187	107	-18	yellow

1V0V	4d_6a_6a_5a	4d	6a	-224	6a	5a	-151	134	9	yellow
1V0V	4e_6e_6e_5c	4e	6e	23	6e	5c	0	247	122	yellow

Table AT8. Oxidation energy (E_{ox}), Hydrogen Binding Energy (E_H), Activation energy for propane ($E_{propane\text{-}TS}$) and propyl ($E_{Propyl\text{-}TS}$) are provided here on all the active site surfaces of all the Mo-only and V containing cluster model. The surface sid_1 is oxidized to tid_1 by ½ O_2, and sid_2 (same surface as tid_1) will be reduced by ½ H_2 to tid_2.

E. Structures of Te-free active sites

Mo-Only

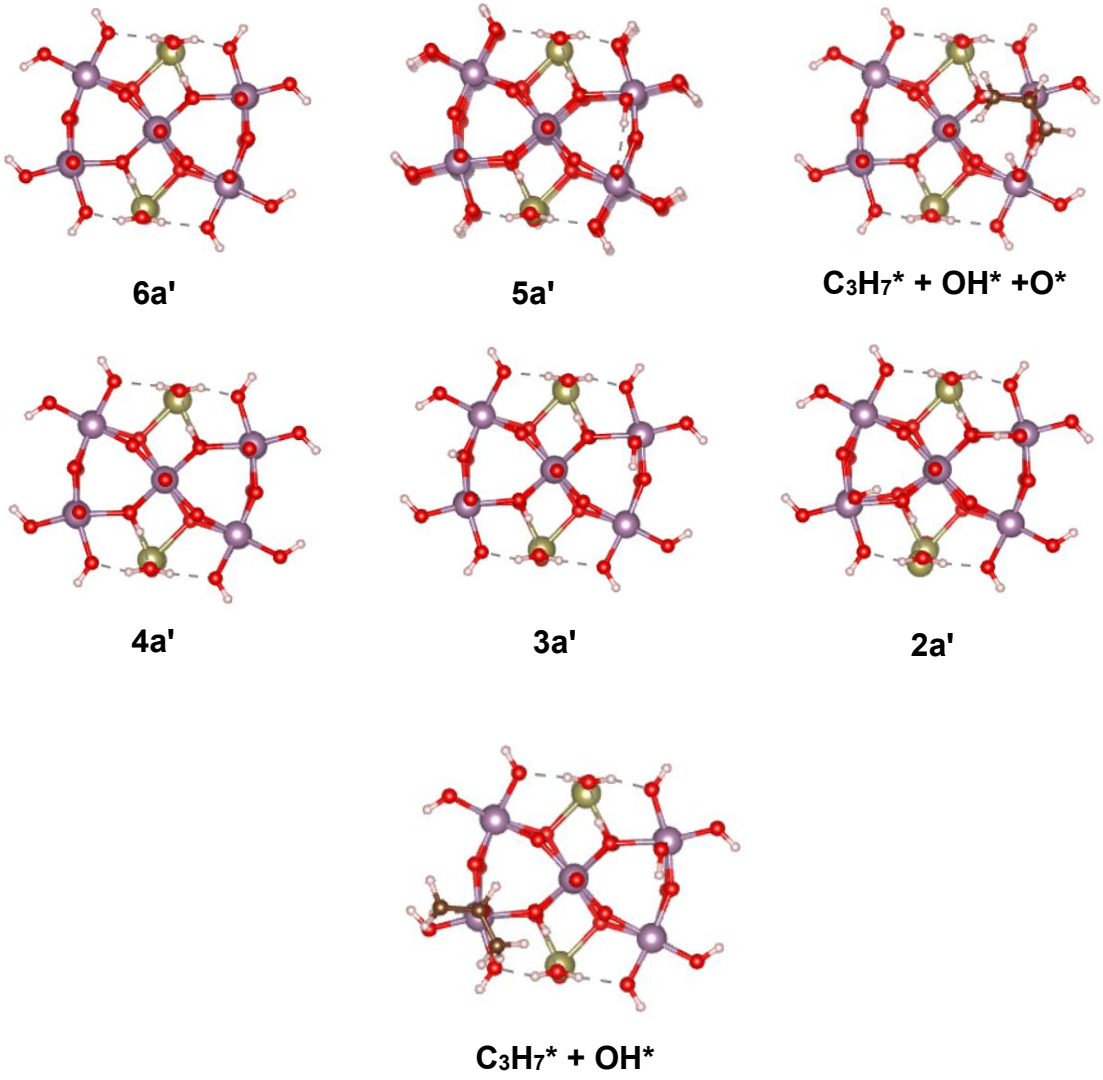

*Figure AF3. Top view of all the Te-free **Mo-only** active sites.*

3V3V

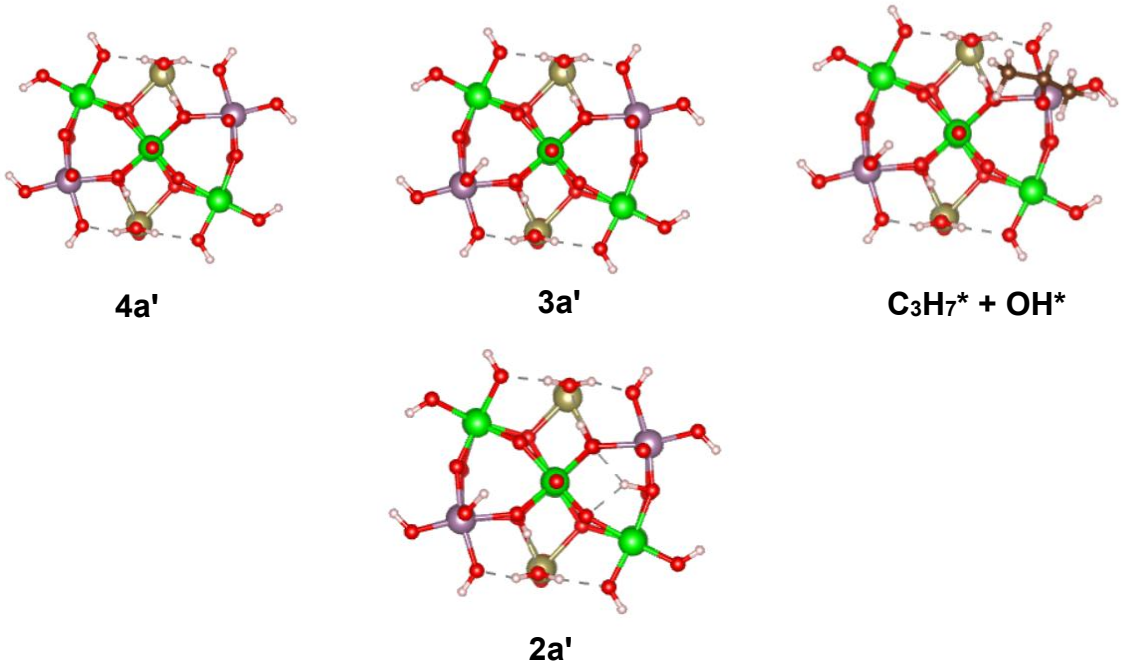

*Figure AF4. Top view of all the Te-free **3V3V** active sites.*

F. Raw data for Te-Free active sites

Surface		Energy (M06-D3) (Hartree)	ZPE (Hartree)	S@400K (kJ/mol/K)
Mo-only	6a'	-9544.527689	0.66345	3.4040
	5a'	-9545.165628	0.67127	3.4126
	C_3H_7* + OH* +O*	-9663.684746	0.76609	3.5792
	4a'	-9469.346018	0.65979	3.4343
	3a'	-9469.978420	0.67088	3.4844
	2a'	-9588.503767	0.76421	3.6117
	C_3H_7* + OH*	-9588.503767	0.76421	3.6117
3V3V	4a'	-14723.879752	0.65303	3.3538
	3a'	-14724.534709	0.66361	3.3748
	C_3H_7* + OH*	-14843.059729	0.75616	3.5462
	2a'	-14725.173021	0.67450	3.4203

Table AT9. Calculated energies (M06-D3), ZPE and entropy@400K of all the Te-Free models used for this work.

Acronyms

AE	Atomization Energy
ALD	Atomic Layer Decomposition
ATM	Axelrod-Teller-Muto
B3LYP	Becke, 3-Parameter, Lee-Yang-Parr
BDE	Bond Dissociation Energy
BH	Barrier Heights
CASSCF	Complete active space self-consistent field
CCSD	Coupled Cluster Singles and Doubles
def2-SVP	Split valence single polarized basis set
def2-TZVPP	Triple zeta valence double polarized basis set
DFT	Density Functional Theory
DLPNO	Domain-based Local Pair Natural Orbital
ES	Electron Spectroscopy
FOD	Fractional occupation number weighted electron density
GGA	Generalized Gradient Approximation
HAE	E-atom addition energy
ICSD	Inorganic Crystal Structure Database
KIE	Kinetic Isotope Effects
KS	Kohn-Sham
LFESR	linear free energy scaling relationships
LSR	Linear Scaling Relation
MEP	Minimum Energy Pathways
MvK	Mars van Krevelen
MLFF	Machine learning force field
NC	Noncovalent Interactions
NEVPT2	n-electron valence state perturbation theory
ODHE	Oxidative Dehydrogenation of Ethane
ODHE	Oxidative Dehydrogenation
OER	Oxygen Evolution Reaction
PBE	Perdew-Burke-Ernzerhof exchange functional
ROA	Reduction-coupled oxo activation
SAR	Structure Activity Relationship
SCAN	Strongly Constrained and Appropriately normed
SOX	Surface Oxidation State
TC	Thermochemistry
TM	Transition Metal
TPSS	Tao, Perdew, Staroverov, and Scuseria exchange functional
TS	Transition States
VASP	Vienna ab initio Simulation Package Software Package
vdW	Van der Waals
ZPE	Zero-Point Energy

Acknowledgements

I want to express my gratitude to several people who helped during my doctoral studies. First and foremost, I am sincerely grateful to my supervisor Prof. Dr. Felix Studt, for accepting me as a doctoral student in his group. Also, for the continuous guidance and support during the last couple of years. I am highly grateful to Dr. Ansgar Schäfer from BASF SE, Ludwigshafen for his continuous guidance, contribution, and enthusiasm to pursue and finish the Doctoral study, also during difficult professional times.

A very special thanks and gratitude goes to Dr. Frank Rosowski from BASF SE Catalysis research, for his crucial discussions in the initial ideation and execution part of the project and to provide financial support from his Key Technology Capability (KTC). Additionally, I want to convey my deep gratitude to Dr. Dmitry I. Sharapa, Dr. Jelena Jelic and Dr. Philip Plessow from IKFT and Dr. Annette Trunschke from FHI Berlin for their enriching discussions and contribution to the research work.

Last but not the least, my love, gratitude and respect go to all my family and friends whose dedicated love and support keep me going and pursue the dream to complete my Doctoral study even in a very critical time of life. The special mentions are my wife, Mrs. Mahasweta Banerjee, my mother Mrs. Putul Sen, my father Mr. Krishna Gopal Sen, my son Mr. Ayudh Sen and my sister Mrs. Trisha Sen. Without your continuous love and support, this study would never have been completed.

List of Publications

1. Sen, K.; Schäfer, A.; Rosowski, F.; Sharapa, D. I.; Studt, F. Quantum Chemical Modeling of the Full Catalytic Cycle for Selective Oxidation of Propane to Propene on the M1 Phase of Mo–Te–Nb–O Mixed-Metal Oxide Catalysts. J. Phys. Chem. C 2024, 128 (34), 14273–14281. https://doi.org/10.1021/acs.jpcc.4c02899.

2. Sen, K.; Schäfer, A.; Rosowski, F.; Sharapa, D. I.; Studt, F. Understanding the Selectivity of Selective Oxidation of Propane to Acrylic Acid on Mo-Te-Nb-O M1 Catalyst using Density Functional Theory

   In Review

3. Sen, K.; Schäfer, A.; Studt, F. Quantum Chemical Study of Selective Oxidation of Propane to Propylene on Mo-V-Te-Nb-O M1 Catalyst with multiple Vanadium Content and Te-Vacancy

   In preparation

Eidesstattliche Erklärung

Hiermit versichere ich eidesstattlich, dass ich die hier vorgelegte Dissertation selbstständig angefertigt habe und keine anderen Quellen und Hilfsmittel genutzt habe als die hier angegebenen. Die wörtlich und inhaltlich übernommenen Stellen wurden als solche kenntlich gemacht. Die Regeln zur Sicherung guter wissenschaftlicher Praxis des Karlsruher Instituts für Technologie (KIT) in der gültigen Fassung wurden beachtet und Primärdaten gemäß Abs. A (6) gesichert. Die elektronische Version der Arbeit stimmt mit der schriftlichen überein. Die Arbeit wurde in gleicher oder ähnlicher Form noch keiner anderen Prüfungsbehörde zur Erlangung eines akademischen Grades vorgelegt.

Ort und Date *Unterschrift von*

M.Sc. Karnajit Sen